POLITECNICO DI TORINO

Master of Science in Mechanical Engineering

MASTER’S DEGREE THESIS

Enhancing Additive Manufacturing Quality through Vibration Analysis and Machine Learning

Candidate: Ramin Moradi

Politecnico di Torino

Supervisors:
Prof. Abdollah Saboori
Prof. Vahid Yaghoubi Nasrabadi
Co-supervisor:
Dr. Amir Behjat

July 2025

Acknowledgments

First and foremost, I extend my deepest gratitude to my supervisors, Prof. Abdollah Saboori and Prof. Vahid Yaghoubi. Their expert guidance, thoughtful feedback, and unwavering belief in my abilities have been the cornerstone of this work. From the earliest project conception through to the final analysis, their mentorship has challenged me to think critically and creatively, and their support has kept me motivated even through the most difficult phases of research.

I would also like to thank my colleagues at the IAM Laboratory of Politecnico di Torino and at the QVaIB group and NDI lab of TU Delft. In particular, Abishay's enthusiasm and hands-on support during experiments were invaluable—always ready to lend a hand in the lab and share his passion for solving any challenge. The collaborative spirit, stimulating discussions, and shared laughter in these groups have been a constant source of inspiration.

This journey would not have been possible without the generous financial support I received along the way. I am grateful to EDISU for providing me with the means to pursue higher education; to the ERASMUS+ programme for the enriching opportunity to study abroad and broaden my horizons; and to Intesa Sanpaolo for facilitating my studies through student loans, allowing me to focus on my academic goals.

To my beloved partner, Nasim: thank you for your unconditional love, patience, and encouragement. Your steady presence and comforting words strengthened me during the long days and late nights, and I could not have completed this thesis without you by my side.

My heartfelt appreciation goes to my family—my mother, father, and brother—for their constant kindness, sacrifices, and unwavering belief in me. Your support laid the foundation for my academic journey and continues to be my greatest inspiration.

Last but certainly not least, I am grateful to my friends for their ongoing encouragement and for reminding me to celebrate small victories along the way. Your confidence in me and your shared moments of joy have made this thesis not just an academic milestone, but a deeply human one.

Abstract

Ensuring defect-free additive manufacturing (AM) parts is essential for reliable performance in safety-critical applications. To minimize defects, process-parameter optimization is required. In this study, we first develop a machine-learning model that predicts optimal L-PBF settings—namely laser power, hatch distance, and scanning speed—using relative-density results from a structured experimental design. Recognizing that conventional non-destructive evaluation via computed tomography is both time-consuming and expensive, we next propose a rapid, cost-effective inspection method based on vibration and modal analysis. Frequency-response features are extracted from printed specimens and used to train a second machine-learning classifier, enhancing defect-detection accuracy. The combined framework—parameter-optimization modelling followed by vibration-based NDE—demonstrates significant reductions in both build defects and inspection time, offering a scalable pathway toward real-time quality assurance in AM processes.

Keywords: Additive Manufacturing (AM), Laser Powder Bed Fusion (LPBF), Process Parameter Optimization, Machine Learning, Relative Density, Vibration Analysis, Modal Analysis, Non‑Destructive Evaluation (NDE), Computed Tomography (CT) Alternatives, Quality Assurance

Contents

Introduction

AM has provided a significant transformation in the manufacturing process of metal components. This method enables the manufacture of complicated geometries with excellent accuracy. Targeted changes in the manufacturing process also enable it to produce localized changes in microstructure and characteristics. Notwithstanding the great work done by people throughout the years that has led to the commercialization of metal AM technologies (Johnson et al., 2020), the ongoing challenge of producing consistent and high-quality results for different applications remains. Primarily, direct metal AM methods fall into two primary technology categories: PBF and DED. Academic studies and industrial uses have increasingly highlighted these two direct AM techniques, which therefore draw main attention. While PBF adds small layers of powder after each fusion phase, DED supplies material via a moving nozzle. Both techniques call for melting the material using a heat source as a laser or electron beam (DebRoy et al., 2018; Milewski, n.d.). Extensive studies have been done lately to improve the efficiency of AM procedures. Using artificial intelligence (AI) is among the most powerful ways to raise AM performance. AI technologies like ML, automation, robotics, machine vision, data mining, large data analysis, and expert systems have shown their effectiveness in manufacturing(Sarker, 2022). ML is a potent instrument for raising the quality and efficiency of metal AM (J. Liu et al., 2023). Particularly when fundamental physical ideas are not well understood but data on process variables, alloy qualities, and product traits are available, it can also be rather important in improving the quality of printed components (Qi et al., 2019). Eventually improving the quality, integrating ML with AM can find faults early, cut waste, maximize input and output properties, and increase speed and accuracy (Gupta et al., 2022). ML techniques have attracted much attention for their outstanding performance in several data-related activities, including regression, classification, and clustering. Based on the degree and kind of supervision required during the training process, these methods fall under supervised, unsupervised, semi-supervised, and reinforcement learning. Combining these potent ML technologies offers a thrilling chance to transform manufacturing processes, address issues, and maximize resource use. Establishing a link called Process-Structure-Property (PSP) becomes possible by thinking of the parameters of the AM process and the material properties, component shape, and microstructural traits as inputs for ML algorithms. Among data—including optimizing processing parameters and property prediction, cost estimate, defect identification, in-situ monitoring, and regulating geometric deviation—various linkages and correlations may be seen(Meng et al., 2020). Therefore, this dissertation will thoroughly examine the uses of ML in a laser-based AM technology, L-PBF. The papers under discussion in the framework of this review text offer an all-encompassing perspective of ML applications in AM. It is interesting to highlight, nonetheless, that the number of articles concentrating on ML broad applications in AM (Meng et al., 2020; C. Wang et al., 2020) is significantly greater than those that directly discuss L-PBF (Pandiyan et al., 2021; Yuan et al., 2018) which tend to be less common in the literature. The selective analysis method in this chapter has two key justifications. Focusing on ML in L-PBF helps one first to a deeper and more thorough knowledge of its practical uses. This method allows one to investigate the particular difficulties and obstacles linked to L-PBF that would be ignored in more general research. Focusing on this part helps to avoid subsequent generalization issues. This method allows for the handling of practical issues and the presentation of creative ideas. Promising non-destructive testing (NDT) method for assessing the integrity of metal parts generated by Laser Powder Bed Fusion (L-PBF) and associated powder-bed fusion technologies including Selective Laser Melting (SLM) is modal analysis. Modal analysis provides a more scalable and affordable substitute than traditional NDT techniques such as X-ray Computed Tomography (CT), which although accurate are time-consuming and expensive. This approach depends on the identification of a component's inherent sensitivity to changes in mass distribution, stiffness, and boundary conditions—that is, natural frequencies and related mode shapes. Defects include porosity, unmelted powder, and delamination directly influence the local stiffness and density of AM parts, therefore they cause appreciable changes in the dynamic response of the component. Recent studies have shown that modal properties can be consistently connected to variations in process parameters that change the thermal history of the part during fabrication—affecting crystallization patterns, grain morphology, and finally mechanical properties including yield strength and ultimate tensile strength. Especially in small-lot manufacturing characteristic of aerospace and biomedical AM applications, the great sensitivity of modal analysis to these variations makes it appropriate not only for defect detection but also for mechanical property prediction. Moreover, its fit with machine learning methods improves its possibilities for digital twin uses and real-time quality control. Thus, modal analysis provides a convincing compromise between accuracy and pragmatism, allowing scalable in-situ or ex-situ inspection techniques—essential for the certification and dependability of AM parts (West et al., 2017)

Additive Manufacturing

Metallic components are capable of being produced through direct metal additive manufacturing immediately following their design in a singular processing step (Sutton & Barto, n.d.). In the additive manufacturing process, intricate shape components are constructed layer by layer in accordance with a digital design. This unique feature enables the direct production of complex shape components from the design, thereby removing the necessity for expensive tooling or shaping tools such as punches, dies, or casting molds, and reducing the number of conventional processing stages (Milewski, n.d.). Manufactured metallic components are employed across multiple sectors, such as healthcare, energy, automotive, marine, and consumer products (DebRoy et al., 2019). Components of this nature encompass metal implants tailored for individual patients (Bose et al., 2018), turbine blades featuring cooling channels (Shinde & Ashtankar, 2017), manifolds utilized in engines and turbines, as well as lattice structures and truss networks optimized for enhanced strength-to-weight ratios (Xue et al., 2020).

ASTM F42 classifies additive manufacturing processes into seven distinct categories: Vat Photopolymerization (VP), Material Extrusion (ME), Material Jetting (MJ), Binder Jetting (BJ), Powder Bed Fusion (PBF), Directed Energy Deposition (DED), and Sheet Lamination (SL) (ISO/TC 261 & ASTM- Komitee F42, 2021). The PBF and DED methods are distinguished by their feedstock types, which can be either powder or wire, as well as the heat sources utilized, including laser, electron beam, plasma arc, or gas metal arc. Electron beam processes occur within a vacuum or low-pressure inert gas environment, facilitating the utilization of reactive metals. Conversely, certain heat sources necessitate the shielding of components with an inert gas (DebRoy et al., 2018). Certain additive manufacturing processes, referred to as indirect metal additive manufacturing processes, are capable of consolidating metallic materials in the form of thin sheets and ribbons through ultrasonic methods, all while avoiding the melting of the feedstock material. Alloy powders may be fused through the application of a binder jetted onto a powder bed, followed by sintering in a high-temperature furnace (Milewski, n.d.).

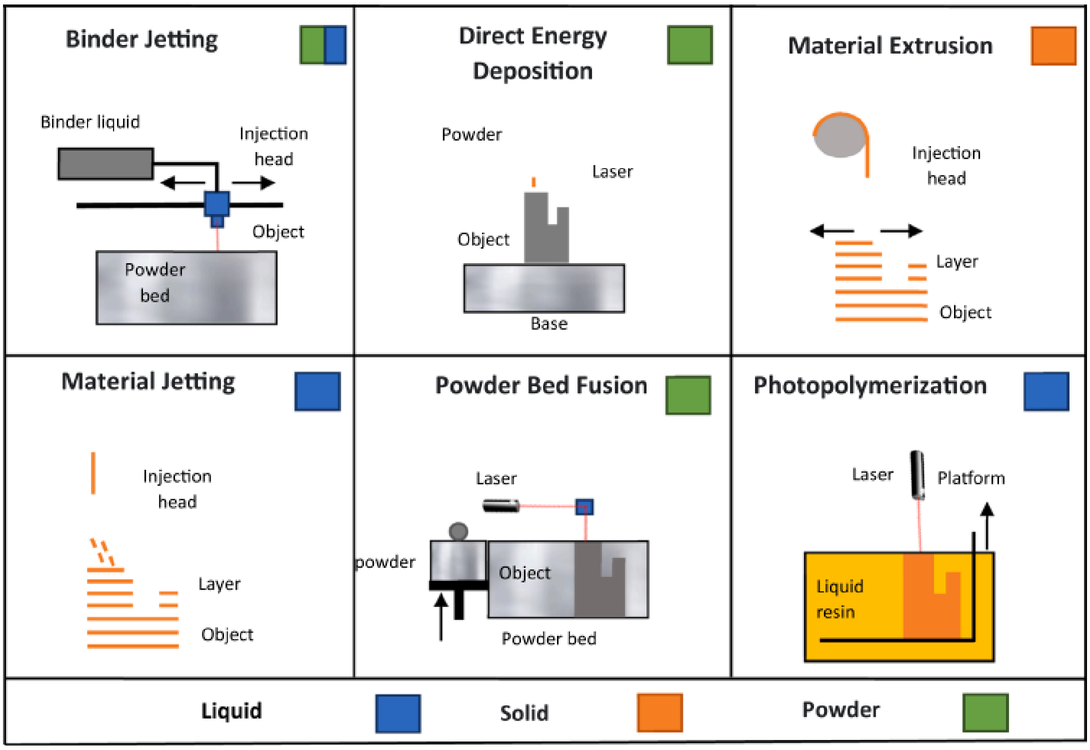

Figure 1 Different AM processes(Segovia Ramírez et al., 2023a)

Metal Additive Manufacturing

Metal additive manufacturing is divided into 4 categories(Armstrong et al., 2022):

1. Powder Bed Fusion
2. Binder Jetting
3. Directed Energy Deposition
4. Material extrusion

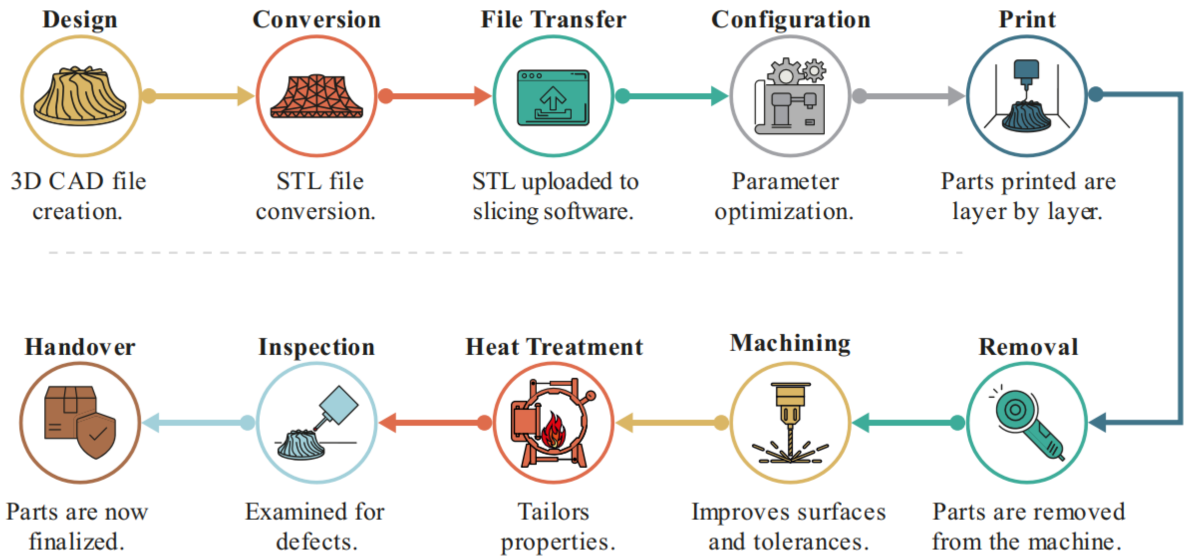

Figure 2 An example of a typical MAM process workflow.(Armstrong et al., 2022)

Definition

DED

DED is gaining popularity due to its mechanical properties, which are comparable to those of conventional manufacturing techniques. DED is an additive manufacturing technique that employs concentrated thermal energy to melt and deposit materials, thereby constructing solid three-dimensional (3D) structures in a layer-by-layer fashion (Q. Wang et al., 2017). This additive manufacturing method is more efficient and economical compared to subtractive manufacturing, enabling the production of complex components with reduced material waste. Additionally, DED demonstrates significant effectiveness in repair and remanufacturing applications (Z. Liu et al., 2016). DED can be categorized into two types according to the feedstock utilized: wire feed DED and powder feed DED, as illustrated in Fig. 2. In the powder feed system, material melts during deposition, whereas in the wire feed system, a laser or arc fuses the wire onto the substrate. The energy source is localized, depositing the feedstock onto the preceding layer or the substrate for the initial layer concurrently. This procedure entails the formation of a molten pool through the melting of both the raw material and the underlying layer. The deposition layer is formed as the substance cools down (Dass & Moridi, 2019).

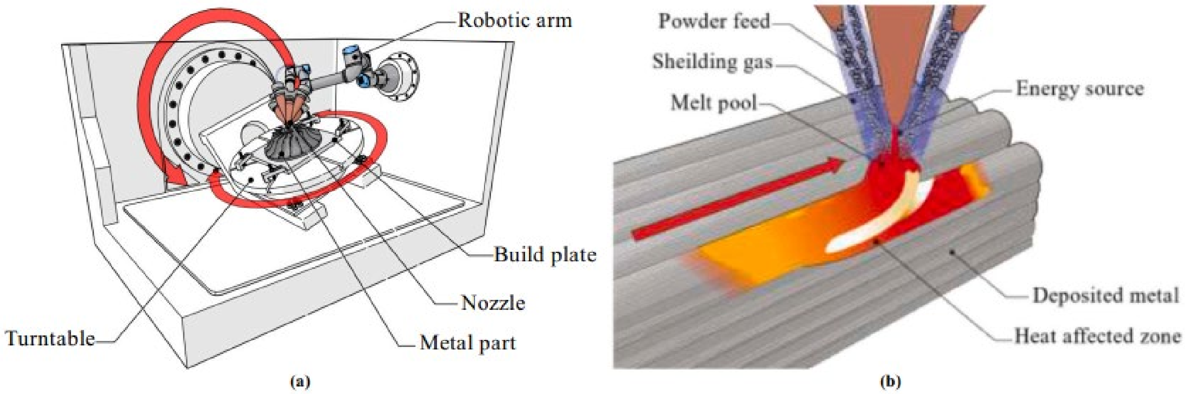

Figure 3(a) Schematic of a typical DED machine (b) Typical powder DED fusion mechanism with melt pool and heat-affected zone schematic.(Armstrong et al., 2022)

Though at a relatively lower production speed, powder feed DED offers greater surface quality than wire feed DED. Though it has significant benefits over other metal AM technologies, DED still struggles to provide preferred surface qualities and reduce porosity and fractures in the created components (Khanzadeh et al., 2019). Several factors, including trapped gas, inadequate fusion, rapid solidification, and poor powder melting, can cause microstructural flaws(Thompson et al., 2015). One major difficulty of the DED method is the large difference in the quality of generated parts. Several factors, including process parameters, laser-material interactions, and defect generation, govern this variability. Though large-scale modeling or testing can improve production quality, these methods are regarded costly and time-consuming. Another way to maximize the quality of DED components is by in-situ monitoring. The enclosed chambers and high melt pool temperatures, which can reach 2000-3000 °C (Era et al., 2023), make this method quite difficult, though. Wire-based DED is a technology like to conventional welding that uses high power to generate thick layers at high deposition rates, hence enabling the affordable manufacture of big components. Parts made using this method, then, often need machining because of notable surface waviness brought on by the creation of massive molten pools (DebRoy et al., 2018).

Binder Jetting

BJ works much like printing ink onto paper. Instead of printing in two dimensions (x, y), the technique uses the third dimension (z) to generate a solid component when metal powder particles stick together using a liquid binder. Usually at ambient temperature(Mirzababaei & Pasebani, 2019), printing helps to remove thermally generated flaws including unwanted grain development and distortion natural with other heat source-reliant MAM methods (Atapour et al., 2020). Furthermore, the surrounding metal powder acts as a transient surrogate support framework. Therefore, no support structures are required, which results in less waste (Ziaee & Crane, 2019). Initially, a fine layer of loose metallic powder fed from a powder hopper is deposited onto a build platform using a re-coater, producing a typical LT of 50–200 µm. Then, using the inkjet printer depicted in Figure 4 (b), moving in the x- and y-direction, liquid binder droplets are selectively deposited onto the current powder indicated in Figure 5(a).

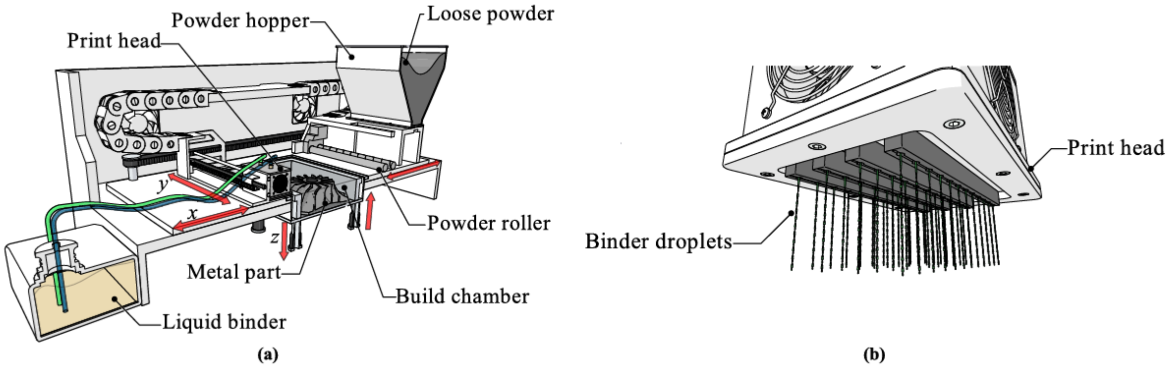

Figure 4 (a) Schematic of a typical BJ machine (b) BJ print head. (Armstrong et al., 2022)

Capillary pressure's influence, together with to a lesser degree gravitational forces, pushes every binder droplet to penetrate and flow into the gaps between the metal powder particles (Figure 5(c)), hence producing a uniform distribution (Figure 5(d)) (Miyanaji et al., 2017).

The mechanical strength, surface finish, and tolerance of green components are determined by this binder distribution vs powder, called the binder saturation level (BSL), whereby the BSL parameter depends on the inkjet print head capacity (Lores et al., 2019). To dry and cure the binder, a heated or UV lamp then passes over the first layer; Figure 5 depicts this sequence.

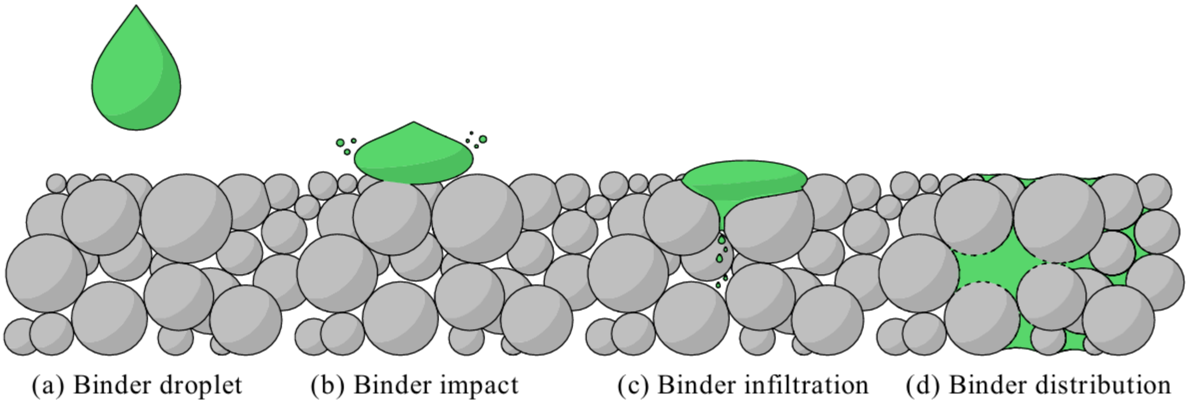

Figure 5 Schematic of binder droplet morphology. (Armstrong et al., 2022)

Material Extrusion

ME is defined by the material extrusion forming a 3D component. Unlike other MAM processes that use loose metal powder, ME machines consume a flexible feedstock akin to MIM media made of metallic powders bound in a polymer matrix that acts as the binding system producing a safer feedstock (Gonzalez-Gutierrez et al., 2018). A typical ME machine shown in Fig. 2 (a) will extrude the bound powder in addition to ceramic release material stored on a separate spool in a heated chamber. Using the heated print head (Fig. 2 (b)), the feedstock is heated to a temperature over the melting point of the polymer binders, extruding the softened material onto a build plate that has been heated. Extruding material in distinct layers equidistant to the preceding layer, the build plate moves on the vertical z-axis; concurrently, the print head linked to a gantry system moves in the perpendicular (x, y) plane to create the shape of the part. Ceramic release material is applied at the same time between the component and any overhanging support structures and the build plate, permitting easy separation after printing. Extruding material layer upon layer tends to produce anisotropy that can be induced by the formation of voids (Fig. 3 (a)) or 'air gaps' between each deposit that can compromise the adhesion between each layer (Carroll et al., 2015; Kok et al., 2018). Therefore, the weakest perpendicular to the plane of material deposition is the strength of the bond and, to more extent, the metal part (Unger et al., 2018). The nozzle's circular profile causes ME to also create components with average surface finishes when the bonded powder is compressed and distorted into a quasi-elliptical shape against the prior layer, shown in Fig. 3 (b). ME components so naturally have undulating side profiles and notches between layers that generate unwanted stress concentrations. Therefore, machining after processing is recommended.

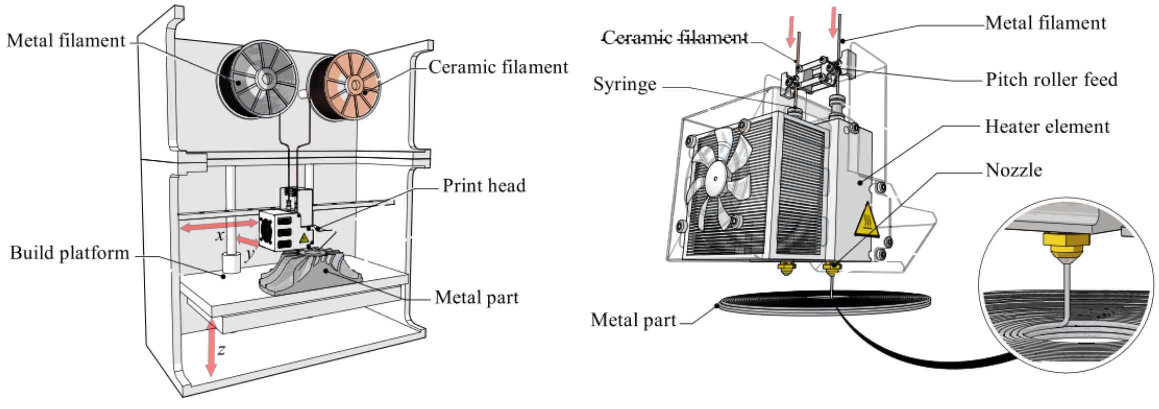

(a)

(b)

Figure 6(a) Schematic of a ME machine (b) Schematic of a typical ME print head mechanism.(Armstrong et al., 2022)

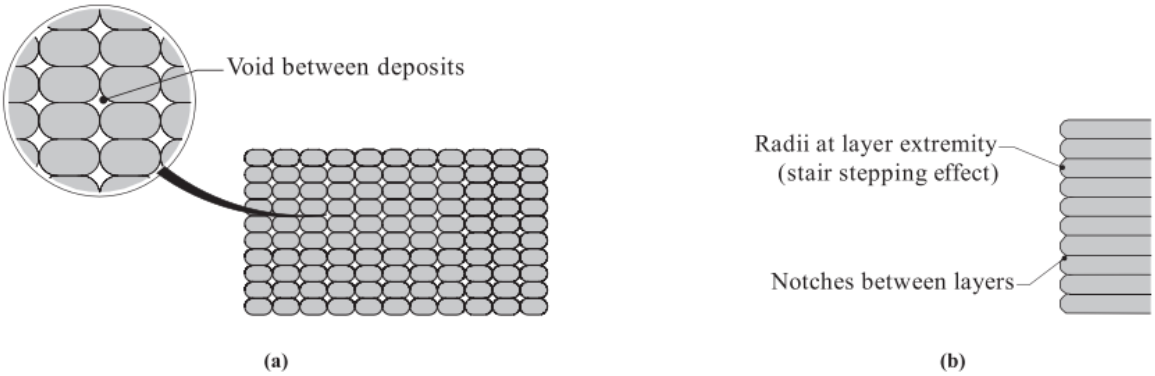

Fig. 3. (a) Schematic of voids between extruded deposits (b) Schematic of radius and notches in extrude material layers.

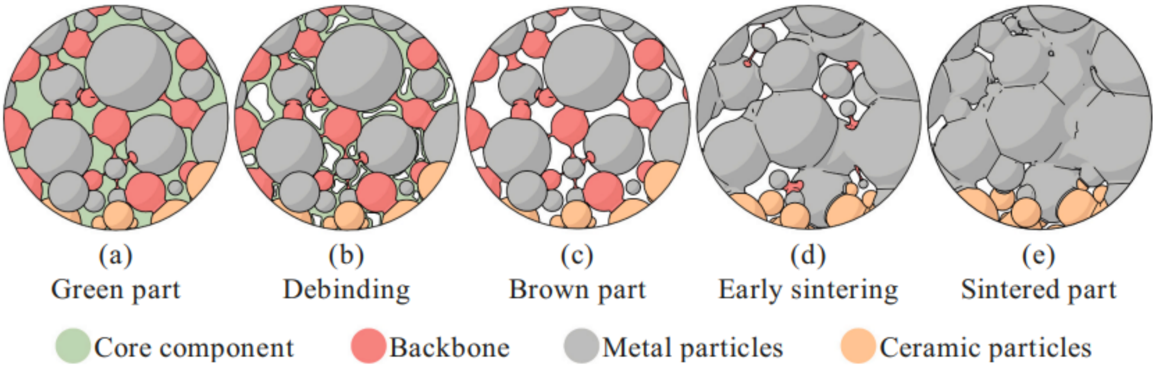

Figure 7Schematic of feedstock morphology - (a) as printed, (b) debinding - thermal decomposition of the core binder component, (c) brown part – following the debinding process, (d) early-stage sintering – thermal decomposition of the residual backbone (e) sintered – thermal densification of metal powder particles. (Gonzalez-Gutierrez et al., 2018)

PBF

Laser Powder Bed Fusion as a part of PBF Process is the main focus on this thesis. Because of its improved capacity to produce metallic and non-metallic components with exceptional accuracy, PBF is generally acknowledged as the main AM technique. Furthermore, PBF might enable free-form production and generate homogenous alloy components with great strength, thereby providing several benefits (Rahmati, 2014). Unlike DED, which employs a laser, electron beam, or arc heat source to melt the feedstock, PBF adds small layers of powder after melting the last one. PBF, on the other hand, has some restrictions regarding bed or box size that prevent it from manufacturing big parts (DebRoy et al., 2018; Elmer et al., 2019; Milewski, n.d.). A subset of PBF, L-PBF uses laser technology particularly for AM. The use of laser, which offers great accuracy and control during the process, is the key difference between L-PBF and other AM methods. As they have various operating concepts that much separate them, this part looks at L-PBF and EB-PBF techniques. Particularly in L-PBF, powdered material is heated, directly liquefied, and then solidified to create solid components. To guarantee great accuracy in manufacturing these components, laser and electron beams are the main heat sources.

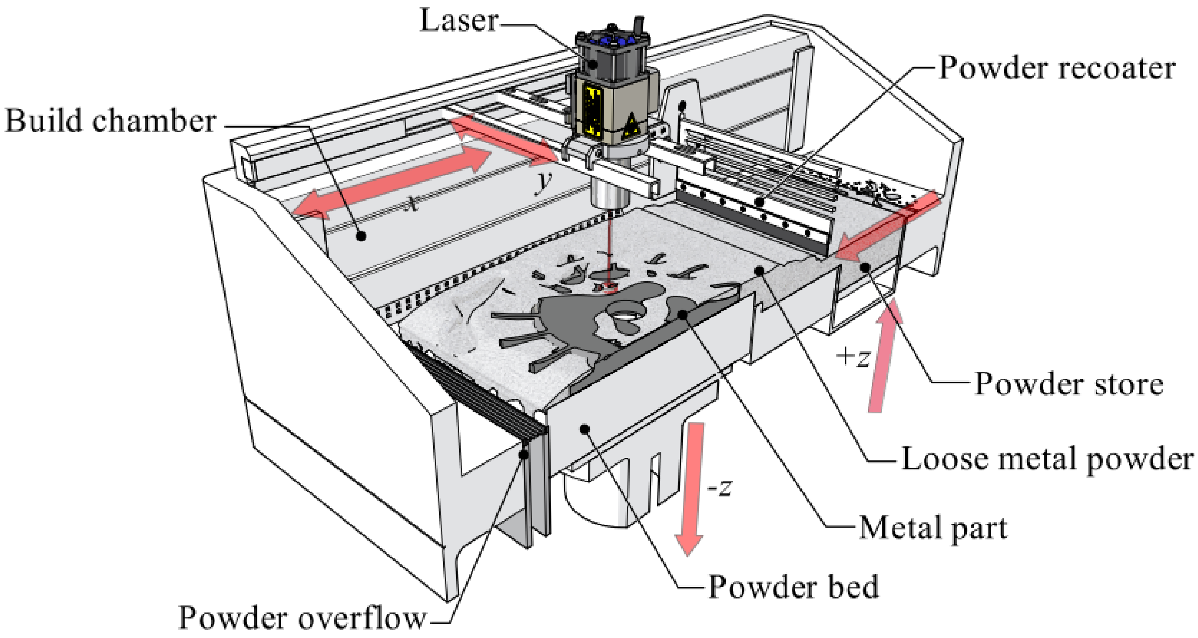

Figure 8 Schematic of a typical PBF machine.(Armstrong et al., 2022)

Using a re-coater blade or roller (Fig. 3), the process advances by covering the prior layer with the following layer of powder from a pre-deposited powder combination. The powder bed's unmelted particles serve as structural supports for the created components. The construction platform lowers following the melting and solidification of a layer of powder, letting a fresh layer spread and melt on top of the last one. Thermal rates in L-PBF might vary from 10^3 to 10 (K/s) (Gu & Shen, 2009). Though it needs support structures, this approach is quite effective at generating complicated shapes with different materials. L-PBF is a very efficient method for manufacturing gradient structures with complex topologies with respect to large-scale production of gradient-structured metals and alloys. There are still challenges to be addressed, though, including a low degree of densification under specific circumstances throughout the process and the tendency for gradient structures to show significantly larger grain sizes, often exceeding 100 nm. Optimizing parameters including power density, powder flow rate, scanning speed, and hatch spacing for every alloy is absolutely vital if one is to meet these difficulties (Song et al., 2024). Using metallic powders in L-PBF presents significant difficulty in finding the suitable process parameter map to produce parts with outstanding microstructure and mechanical properties. Some studies have so focused on LPBF process parameter optimization. These studies fall into three main categories: laser-related, powder-related, and powder-bed-related traits (Abd-Elaziem et al., 2022).

Defects in Metal Additive Manufacturing

Variations in manufacturing parameters—such as laser power, powder shape, layer thickness, and scanning strategy—as well as the initial properties of the feedstock material—as shown in Fig. 5—have the main effects on the generation of defects and the resulting microstructural characteristics in metal additive manufacturing (AM). Based on Taheri's [15] taxonomy, this section lists the most important forms of defects.

Porosity

In general, one of the most often occurring flaws in sintering and melting-based AM techniques is porosity. Usually resulting from inadequate melting or entrapped gasses, it shows as gaps or areas missing material and is especially important in structural components since it reduces mechanical performance (see Figure 9). Usually existing between layers, these flaws could comprise non-melted powder particles ranging from 5–20 µm.

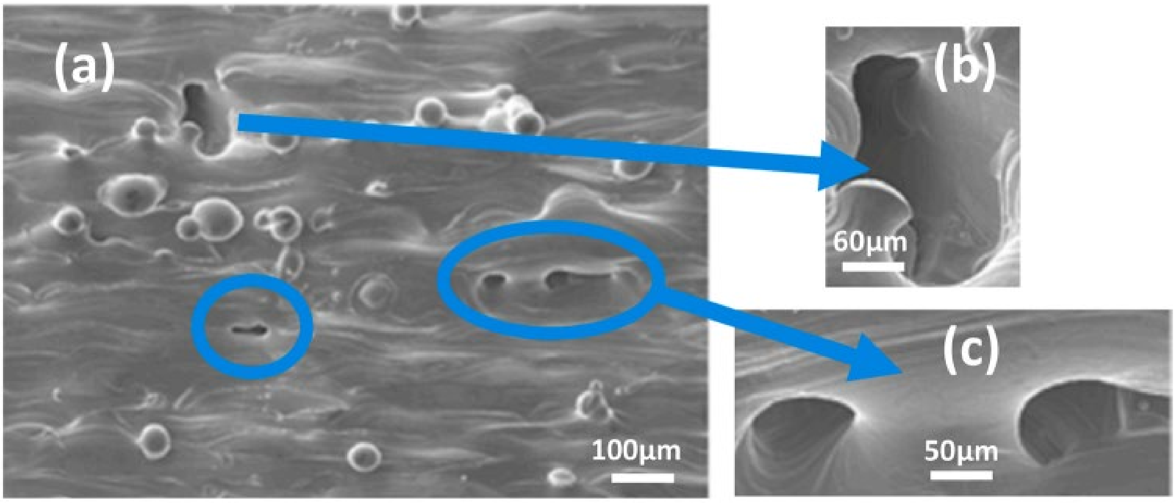

Figure 9 Scanning electron microscope micrographs of Ti-6Al-4 V samples fabricated by SLM; (a) the top surface with a powder layer thickness of 60 µm; (b) Open pores; (c) Cave-like pores. Fig. 4 Alt Text: This graph shows the image acquired with microscope about AM samples, providing details about porosities included in the material. (Qiu et al., 2015)

Production of porosity is intimately correlated with processing conditions and properties of beginning powder. While macroscopic porosity can be classified into gas-induced porosity and lack of fusion (LOF), micropores smaller than the powder grain size are commonly associated to entrapped gas within powder particles.

Because their smaller particle size calls for more energy input to reach complete melting, gas-atomized powders often show better porosity levels. Low interlayer bonding resulting from inadequate energy density during printing can cause holes and LOF faults. Variations in powder form, particle distribution, substrate conditions, and processing laser beam defocusing can also cause LOF.

Inclusions

Mechanical characteristics of AM components are substantially influenced by purposeful or inadvertent inclusion. Usually distributed at modest sizes (~200 µm), intentional inclusions like reinforcing particles help to improve particular mechanical properties without generating stress concentrations. On the other hand, inadvertent inclusions might result from feedstock or process-induced discontinuities, which would produce oxide residues ranging from 0.5 µm to 1 mm. For ductility and fatigue strength especially, such inclusions are detrimental. Reliable identification and quantification of these internal nature flaws call for sophisticated NDT methods.

Cracks

Usually resulting from residual stresses over the yield strength of the material, cracks are discontinuities inside the part structure. They can start from thermal gradients created during layer-by- layer fusion or from cooling. Stress concentrators that help to start and propagate cracks can be poor bonding between neighboring powder layers, geometric imperfections, inclusions, or unmelted particles. Inappropriate energy input, scan approach, or thermal control can increase the likelihood of cracking.

Defects in powder materials and unfused powder

Integrity of AM components is significantly influenced by the quality of the feeding powder. Manufacturing defects in powder manufacture and the presence of contaminants might provide voids or inclusions, therefore compromising part quality. Smaller powder particles may present safety concerns during handling even if they can increase packing density and lower flaws. Unfused powder—which stays unmelted during processing—may become caught inside the part and complicate traditional detection techniques. Furthermore offering a clue of possible powder bed contamination is the existence of unfused powder.

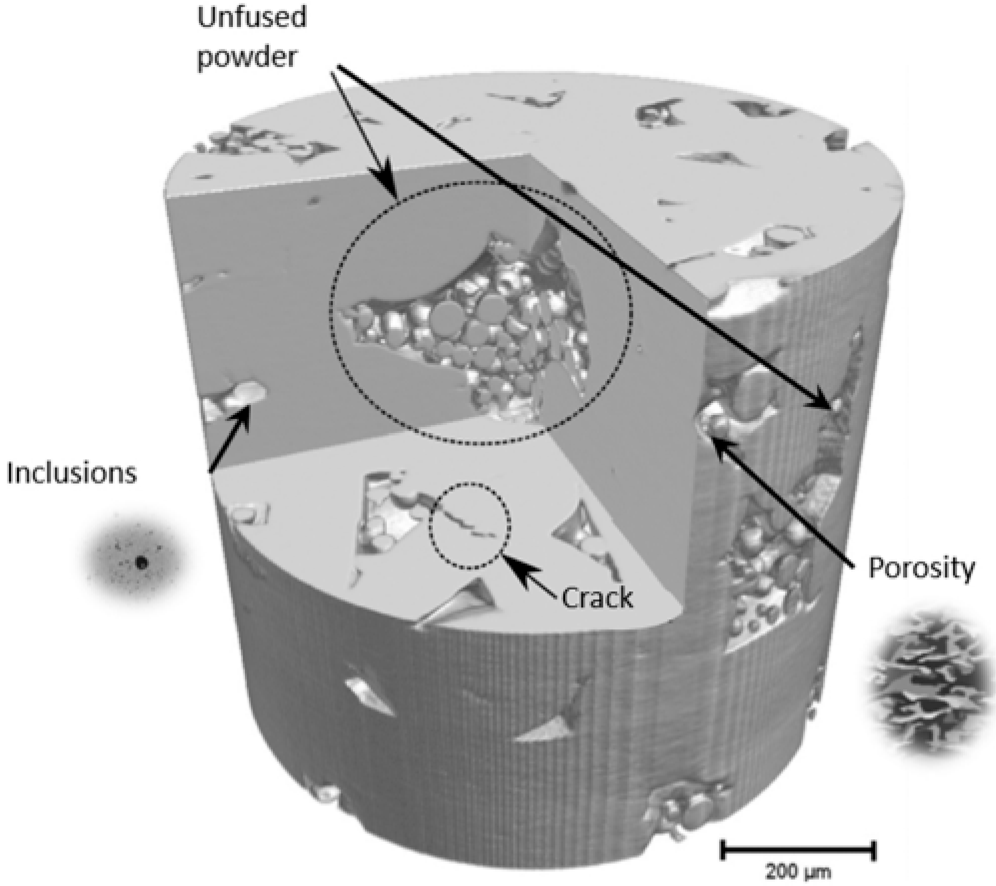

Figure 10 Some of the typical failures found at AM. Fig. 5 Alt Text: Different failures are characterized in the same component to show the typical distribution of this failures. Unfused and trapped powder are usually developed in the interior part of the component. Cracks can be internal or external and its size and shape depends on several factors. Inclusions or porosity have a relevant influence on the final characteristics of the AM component, and they must be detected with advanced techniques. (Kim et al., 2017)

Process Parameters

In metal additive manufacturing (AM), the choice of suitable process parameters is essential since it directly affects the microstructure and fault development of the produced printed item. Mostly involving expensive trial-and-error experiments and computationally demanding mechanistic simulations, research efforts over the past decade have been focused on determining "optimal" processing regimes for diverse materials to ensure defect-free manufacture. The microstructure of the AM part is affected by the thermal history of the AM process, which hence influences its mechanical characteristics including tensile strength, ductility, surface roughness, fatigue life and hardness. Therefore, making excellent AM components depends mostly on a correct knowledge and optimal control of the process parameters. Thus, suitable process parameters should be found for every given design aim, production objective, feedstock material.(Chia et al., 2022)

One of the materials where there has been notable success in reaching near full density utilizing L-PBF technique is stainless steel 316L (SS316L)(Miranda et al., 2016). Together with other techniques to achieve high densities particular to SS316L specimens, this part discusses the work done on main process parameter optimization. Most of the work (Cherry et al., 2015; Liverani et al., 2017; Sun et al., 2016; Tucho et al., 2018; Yakout et al., 2019) on L-PBF parameter investigations makes use of the effect of laser energy density on part densification. The energy density (E) is connected to the main process parameters including laser power (P), scanning speed (v), hatch spacing (h) and layer thickness (t), as stated by Equation 1.(Tucho et al., 2018) the author shows in Figure 9 the factors of interest. Hatch spacing (h) is the distance between consecutive scan vectors and layer thickness (t); laser power (P) is the total energy emitted by the laser in unit time; scanning speed (v) is velocity at which the laser spot moves across the powder bed along the scan vectors.

$$VED = \frac{P}{v\,.\,h\,.\,t} \qquad \textit{Equation 1}$$

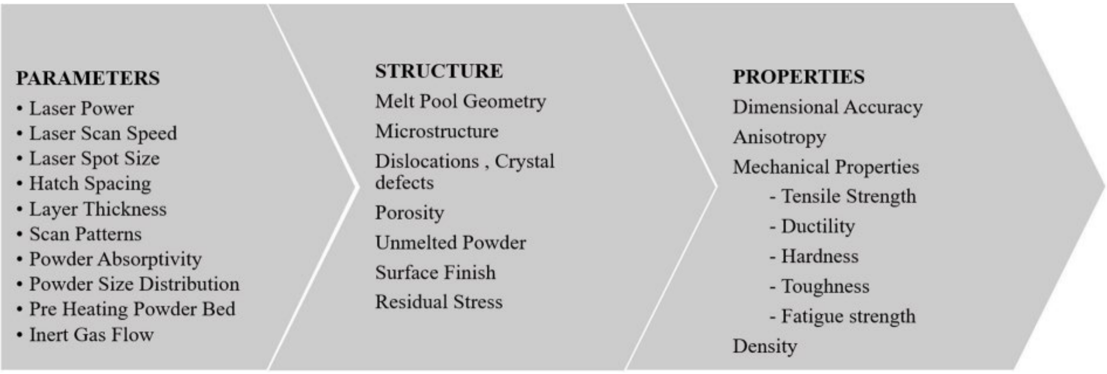

Figure 11 Relationship between process parameters, structure and properties in L-PBF process. (Ahmed et al., 2022)

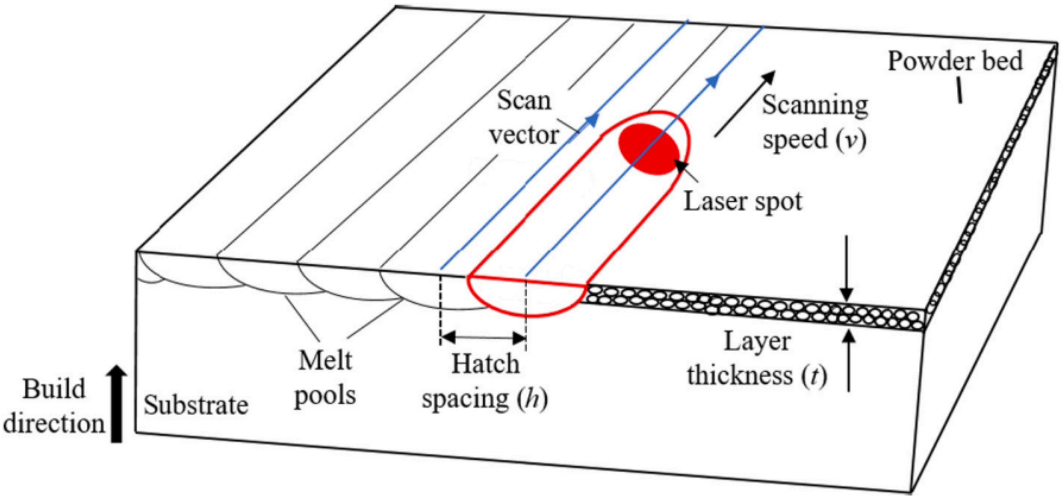

Figure 12 Illustration of process parameters for study in L-PBF process. (Ahmed et al., 2022)

High quality components depend on a thorough study on the interaction of the process parameters and its influence on densification. Yakout et al. (Yakout et al., 2019) did one such work performing full factorial permutation using laser power, scanning speed, and hatch spacing. Yakout effectively produced range of energy densities shown in Figure 10(a) which results in stable melting, continuous beads, and homogeneous melt tracks by using the effects of energy density on resultant densification in L-PBF. Because of formation of voids and lack of powder fusion, lower values of laser energy density shown significant porosity; higher energy density values beyond a certain limit resulted in decreasing densification leading to unstable melt pool, vaporization, and micro-segregation of alloying elements. This may also be easily appreciated from the observations made from the fractography of SS316L specimens created with different laser energy density values as shown in Figure 10(b), (i).

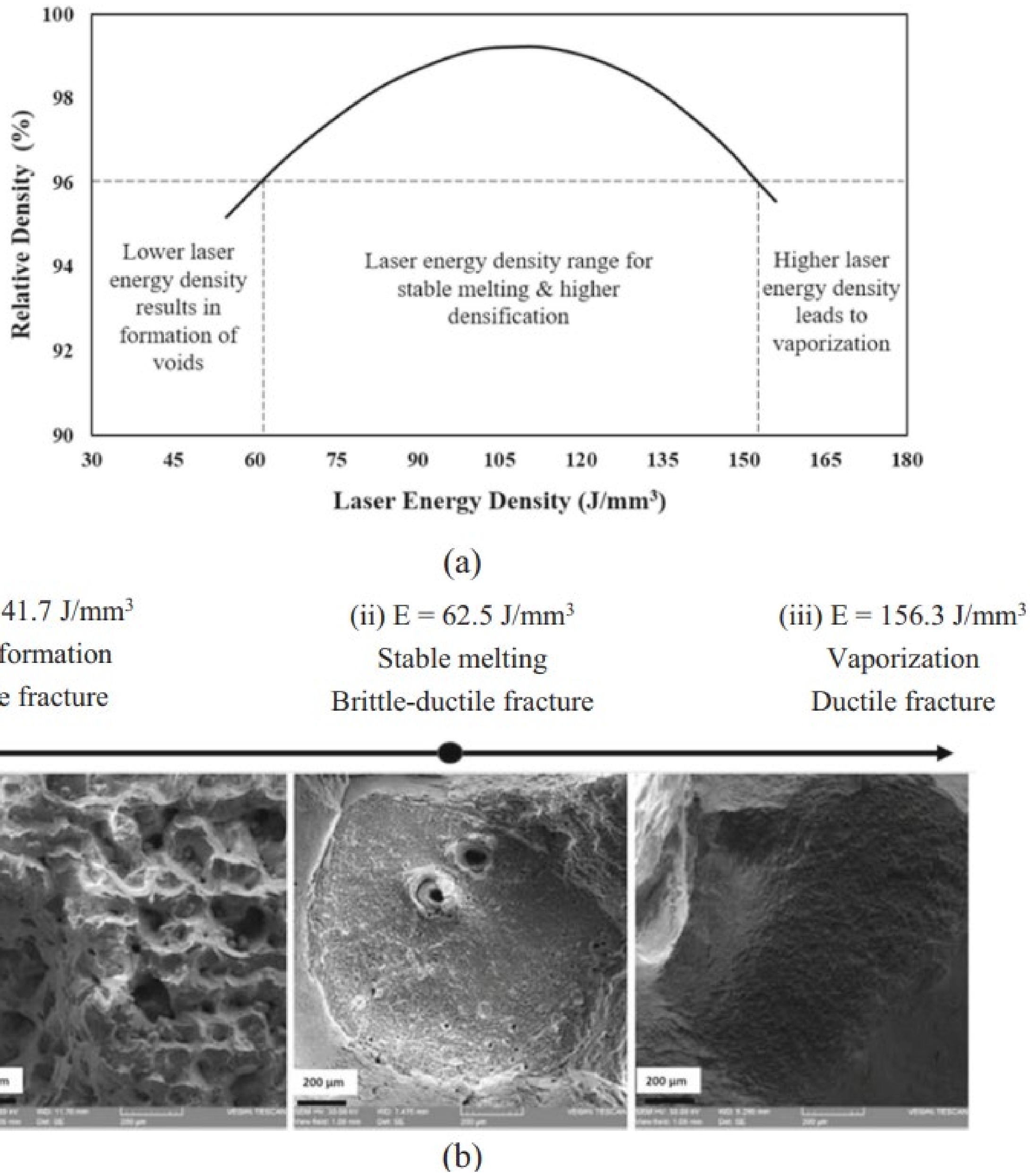

Figure 13 (a) Effect of various laser energy density values on resulting densification (data adapted from (Yakout et al., 2019)), (b) Fractography of SS 316L samples produced at laser energy density value of (i) Lower value of 41.7 J/mm3 results in "brittle fracture" due to presence of voids (ii) 62.5 J/mm3 results in "brittle-ductile" fracture due to less voids present (iii) 156.3 J/mm3 results in "ductile" failure due to vaporization of powder (Ahmed et al., 2022)

Brittle fracture noted in lower energy density value of 41.7 J/mm3 specimen build with significant voids present (ii) Less voids are seen in specimen built with energy density value of 62.5 J/mm3 than in specimen built with lower value (i). Brittle-ductile failure is reported in this regard. Mass metal vaporization is shown by ductile failure observed in specimens constructed with greater energy density value of 156.3 J/mm3. Therefore, reaching sections with lowest porosity flaws depends on the identification of suitable energy density range. Figure 11 shows the ranges of laser energy density obtained from different literature together with their corresponding densities in L-PBF processed SS316L specimens. Arriving at optimal laser energy density, numerous combinations of laser parameters including laser power, scanning speed, hatch spacing and layer thickness have been used. Higher densities (over 99%) have their ideal range of energy density values dispersed between 50 J/mm3 and 150 J/mm3. Furthermore, shown is that the resulting densification values vary even for the same energy density values, for instance for 100 J/mm3, suggesting dependency on the individual values of laser power, scan speed, hatch spacing and layer thickness used. For a two-parameter set with same energy density value of 80 J/mm3, for instance, the parameter set having lower hatch spacing of 0.08 mm shown higher densities of 99.7% compared with parameter set with higher hatch spacing of 0.14 mm with densification of 99.27%. This is mostly due to tighter overlap of melt pools for bonding given by reduced hatch spacing, so lowering porosity. With constant layer thickness of 0.03 mm to investigate the impact of laser energy density in the range of 50–80 J/mm3, Tucho in his experiments additionally adjusted the laser power (150 W to 200 W), scan speed (400 mm/s to 1600 mm/s) and hatch spacing (0.08 mm to 0.14 mm). While the sample built with higher energy density value of 80 J/mm3 results in nearly defect free parts, a comparison of SEM images of the specimen for the energy density range shows that samples built with lower energy density value of 50 J/mm3 results in porosity due of lacks-of-fusion. For SS316L specimens, a good mix is advised to be lower hatch spacing (0.08 mm) and rather high scan speeds (800 mm/s), which will help to achieve density above 99%. Using a modulated laser system, Cherry et al. (Cherry et al., 2015) similarly displayed similar tendencies about rise in energy density resulting in decrease in porosity. The energy density is varied using the exposure time and overlap distance to reach an ideal limit value of 105 J/mm3 hence attaining densification up to 99.6%.

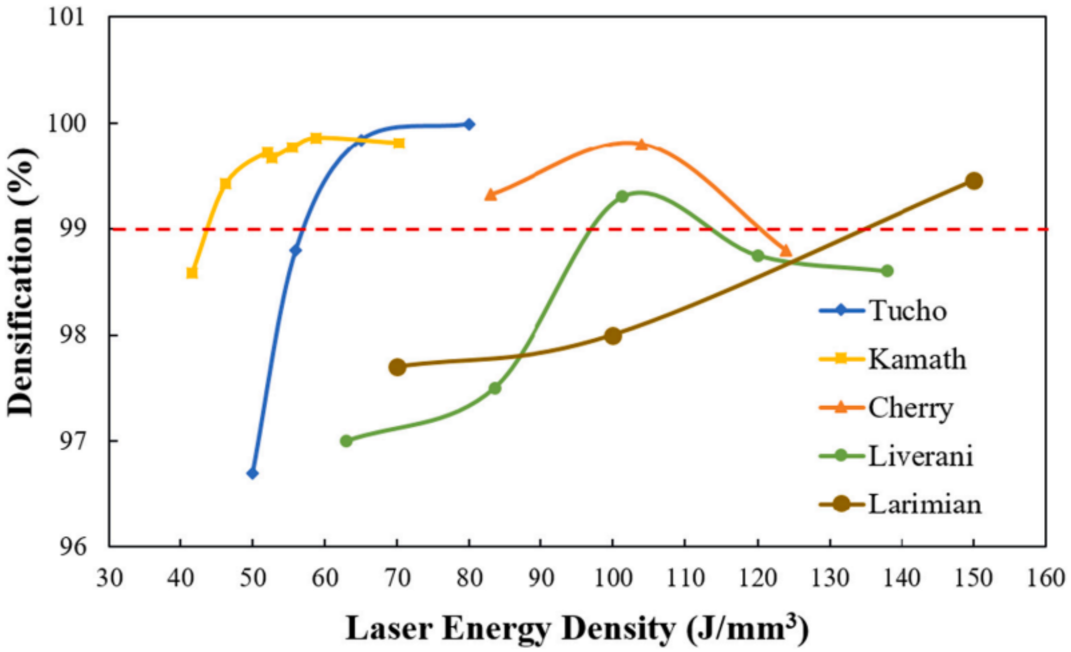

Figure 14 Ranges of energy densities and corresponding densification values collected from various literature for SS316L specimens(Ahmed et al., 2022)

Cherry also noted that growth of pores size was seen and that values beyond 105 J/mm3 exhibited indications of balling action, therefore indicating a limit to which energy density could be raised by low melting element vaporization. Using a mix of laser power in the range of 90–150 W and scan speed between 500 and 900 mm/s, Liverani et al. (Liverani et al., 2017) also shown that an increase in energy density up to a value of 100 J/mm3 boosted densification (99.9%). The study underlined how, among all the parameters, laser power was the main determinant of the energy density influencing L-PBF sample densities. In his study on light weight lattice struts made of SS316L material, Zhong et al. (Zhong et al., 2019) found that, for increasing densities of parts, the optimal energy density falls in the similar range up to 110 J/mm3. Using a reduced scan speed of 50 mm/s produced maximum densification up to 98.22%, AlMangour et al. (AlMangour et al., 2018) demonstrated influence of laser scanning speed on densification. Reduced scan rates lead to heat accumulation needed for complete powder melting and dense structure building.

Individual effects of L-PBF process parameters including laser power, scanning speed, hatch spacing and layer thickness can be also maximally combined to achieve a higher densification. Higher densification and avoidance of balling as advised by Li et al. (Li et al., 2009) depend on an optimum combination combining higher laser power, lower scan speed, narrower hatch spacing and thinner layer thickness. Because lower oxygen concentration and smaller mean particle size help densification, it was also shown that use of gas atomized powder produced better results than water atomized powder. Kruth et al. (Kruth et al., 2010a) showed by density the combined influence of scanning speed and layer thickness.

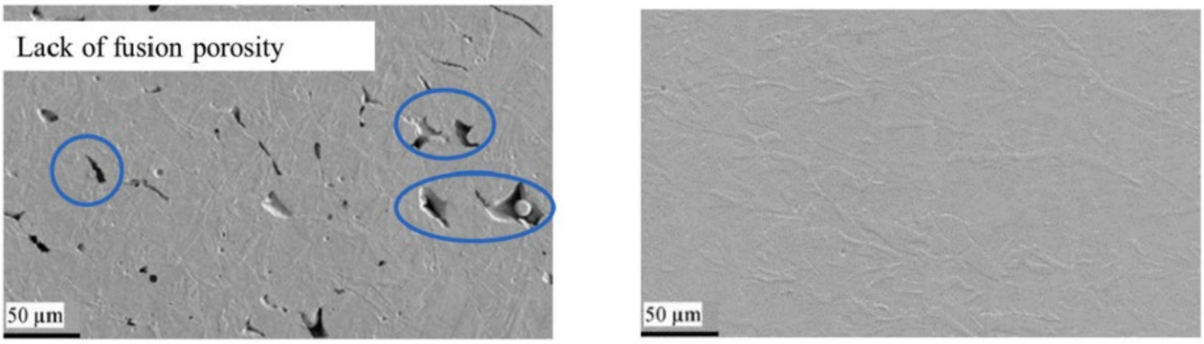

Figure 15 SEM images of higher porosity defects due to lacks-of-fusion observed using energy density value of 50 J/mm3 (left) compared with minimal defects with higher energy density value of 80 J/mm3 (right)(Tucho et al., 2018)

At suitably low scan speeds, the relative densities of samples are nearly independent of different layer thickness values (20 µm, 30 µm, 40 µm, illustrated in Figure 13). But at high-speed values above 350 mm/s, densification was reduced and is more severe for a 40 µm layer thickness value since insufficient laser depth penetration and poor layer bonding resulting from shorter laser exposure duration.

Miranda et al. (Miranda et al., 2016) investigated the impact of single parameter as well as multiple parameter interactions on densification by means of a statistical technique combining ANOVA (analysis of variance) method with experiments. While for laser speed and hatch spacing increasing values resulted in lesser densification due of inadequate powder melting, increasing laser power leads in greater densification in single parameter analysis. High density can be obtained in multiple parameter studies by combining intermediate values of laser power and hatch spacing as shown in Figure 13(a), and by combining intermediate values of laser power and scan speed as shown in Figure 13(b.).

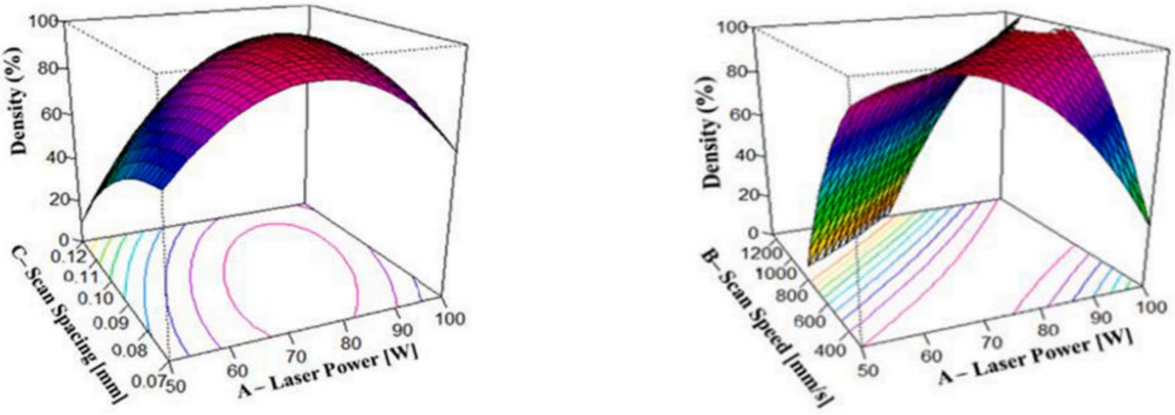

(a) (b)

Figure 16 (a) Combination of power and scan spacing, (b) combination of power and scan speed used for achieving high densification (Miranda et al., 2016)

L-PBF is recognized to be a usually slow additive manufacturing technique, so changing parameters, including scan speed, hatch spacing, and layer thickness, has limits and influences the component quality. Still, attempts have been made to achieve high densification in line with rapid building rates. Liu et al. (Y. Liu et al., 2021) recently employed a 200 μm layer thickness and raised the build rate to 12.4 mm^3/s (2.5–10 times greater than utilizing a lower layer thickness), so attaining a densification of 99.99% in SS316L specimens. It was shown that preventing flaws like unmelted powder and balling depends critically on laser exposure length (120–160 μs) and laser overlap (40%). Increasing layer thickness also helps greatly. Sun et al. (Sun et al., 2016) used faster speed and higher range of power than usually used ranges reported to boost the total build rate by ~72%. Using a power of 380 W and a speed up to 2000 mm/s, Sun et al. produced 10 mm side cubes to reach high-density rates of 99.9%. Using high laser power up to 400 W, Kamath et al. (Kamath et al., 2014) reported a broad range of high speeds (1900 mm/s to 2200 mm/s), obtaining 99.5% densification. Shi et al. (Shi et al., 2020) showed an increase in layer thickness to lower construction time by demonstrating densification above 99% utilizing 250 μm layer thickness and laser power of 400 W with different combinations of scan speed and hatch spacing. Thus, proper parameter selection enables one to achieve good part quality together with high build rates.

The quality of the melt pool created during the laser melting process indicates the laser power and speed applied throughout the operation. Wei et al. (Wei et al., 2011) demonstrated experimentally the effect of melt pool dimension on densification by using an optimal combination of laser power and speed to produce a stable and continuous melt pool, producing higher densifications. Wei et al. also found that, for the same process parameters (98 W power, 90 mm/s speed, and 70 µm hatch spacing), lower layer thickness (~100 µm) produced higher density compared to higher layer thickness values owing to complete powder melting and sufficient bonding between layers.

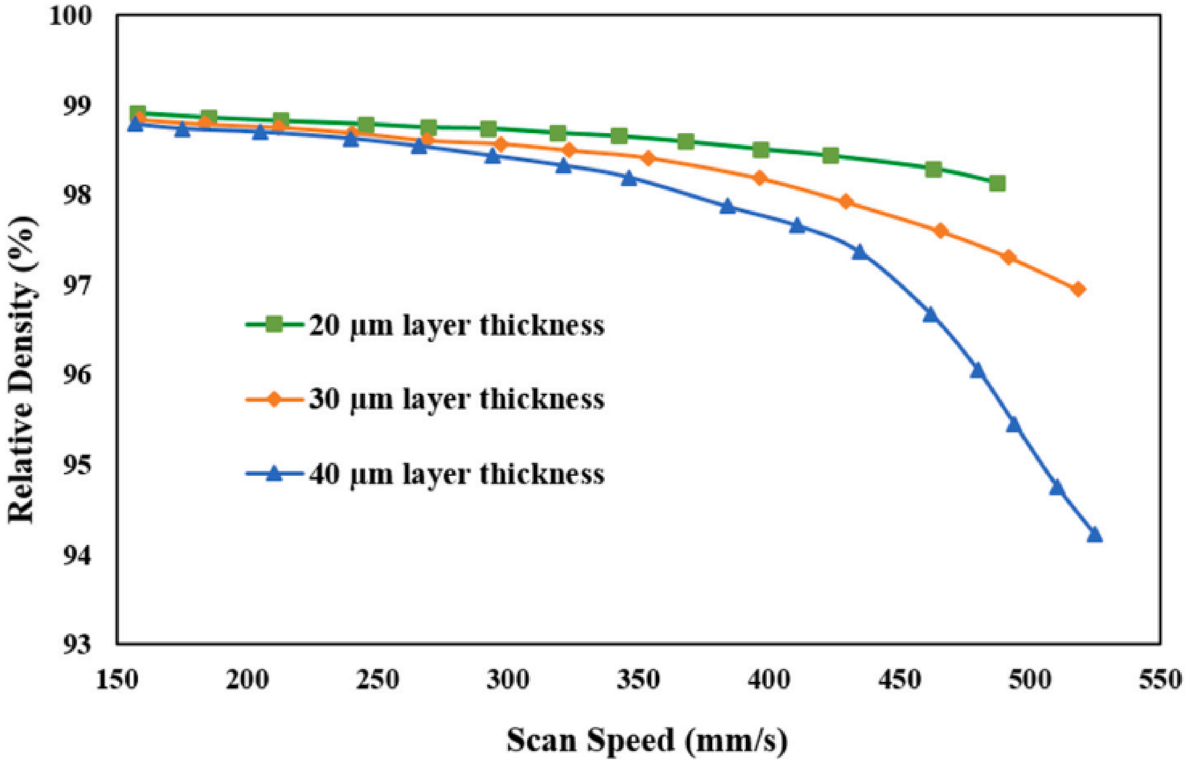

Figure 17 Influence of scanning speed on densification for different layer thicknesses(Kruth et al., 2010b)

L-PBF factors like laser power, scan speed, and hatch spacing have been extensively applied for density control as covered in the previous part. Higher densification does, however, also depend much on the scanning techniques and process parameters.

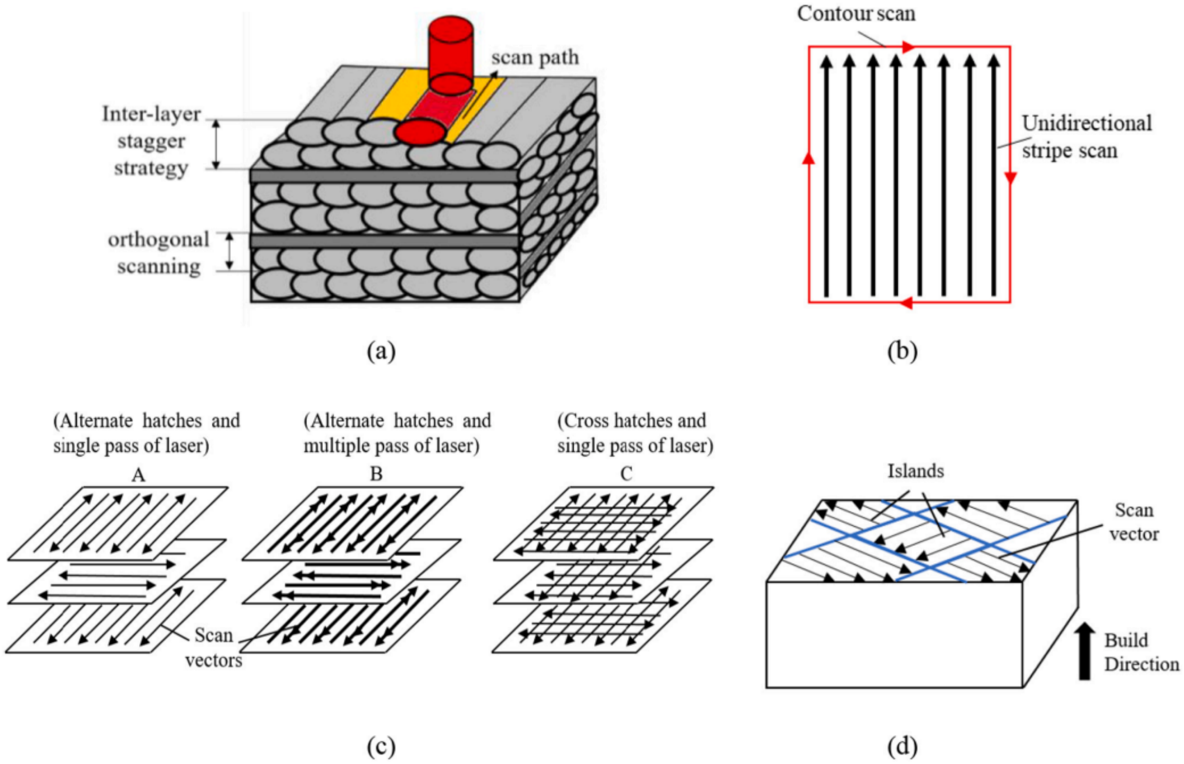

Figure 18 Illustration of different laser scanning strategies used for attaining densification (a) Inter-layer staggered strategy (b) Stripe and contour strategy (c) Different laser scanning strategies (d) Checkered Island strategy. (Ahmed et al., 2022)

Appropriate hatch spacing and laser scanning patterns guarantee enough heat accumulation required for bonding between tracks as seen in work by Wang et al. (Di et al., 2012) using a strategy called inter-layer staggered scanning strategy illustrated in Figure 15 (a) to achieve densification of more than 98% in SS316L samples. Under this approach, the first two adjacent layers are scanned in a staggered pattern, and the next two adjacent layers are scanned orthogonally to the first two layers. This scanning pattern eliminates flaws developed in earlier layers. Experimenting with various laser scanning patterns for a specified process parameter value of laser power (175 W), scanning speed (668 mm/s), hatch spacing (120 μm), and layer thickness (30 μm), Salman et al. (Salman et al., 2019) found Using stripe and contour strategy shown in Figure 15(b), densification up to 99.9% is achieved; in this scan paths are parallel to one another in unidirectional fashion and also includes a contour scan around the perimeter of the build for finishing purpose, so ensuring good overlap between the scanned tracks and leads to almost completely dense samples. Larimian et al. (Larimian et al., 2020) investigated several scanning techniques for 316L stainless steel samples shown in Figure 15(c) as type A, B and C. Compared to samples processed with scanning strategy type - B (97.7%), type - C (98%), the samples processed using scanning strategy type - A attained higher densities

(99.45%). Higher cooling rates produced by the scan approach type-A produced a refined structure and great densification. Likewise, different scanning techniques are employed to obtain high quality parts; one such strategy depicted in Figure 15(d) divides the construction layers into independent and randomly scanned sub areas (Yusuf et al., 2017). Scanning vectors of nearby islands perpendicular to one another results in each layer with tracks scanned in several directions. Because of equal melting of powder in all directions of the melted powder layer, this checkered technique produced densification of 99%.

Optimizing Process Parameters

Optimization of the process parameters is done to enhance different targets. The targets vary from physical conditions (melt pool modes and aspect ratios); defects (relative density, porosity and distortion tolerance); mechanical properties (surface roughness, tensile and fatigue properties); microstructural properties (grain phases, grain size, grain aspect ratio, grain boundary angle and grain misorientation); manufacturing performance (time, energy, cost and efficiency). Conversely, the main parameters are controllable process parameters constrained by the machine's capabilities and customizability. The complicated metallurgical process involved in AM allows one to identify the main parameters just by considering bulk energy input during the operation. Especially in PBF, the effects of the heat power (P), scanning velocity (v), hatch spacing (h), and layer thickness (t) on the AM component quality are most usually studied. Many times, these four factors are described as a volumetric energy density (VED). Apart from VED, several parameter combinations have been suggested, including linear input energy density, linear energy density, and surface energy density. Although VED is a widely used technique for evaluating the energy input, the overt physical simplification has demonstrated to be unreliable.(Chia et al., 2022)

Ensuring component dependability and performance in Laser Powder Bed Fusion (L-PBF depends critically on the identification and measurement of internal flaws like pores, cracks, and lack-of-fusion voids. Commonly used experimental methods for this aim include several ones following ASTM B962 criteria, the Archimedes test is a conventional and extensively used method for approximating bulk porosity depending on density variations by immersion in a fluid. This approach cannot localize flaws in the part, though, and has low spatial resolution. With 3D volumetric information regarding interior structures, X-ray computed tomography (CT) presents a non-destructive alternative that permits thorough study of pore size, distribution, and shape. Particularly helpful for assessing lack-of-fusion and keyhole defects, optical and SEM-based image analysis of polished cross-sections also permits defect quantification; this is destructive and confined to the observed plane. Although they demand access to specific facilities, more sophisticated techniques such neutron diffraction can be utilized to evaluate residual stress and porosity in bigger or denser sections. Performance-based techniques including thermal conductivity measurements and vibration analysis have lately attracted interest as indirect means of defect identification.(Mohr et al., 2020) These provide a non-destructive, maybe in-situ mode of evaluation depending on the interaction between mechanical or thermal behavior and internal defect content. Though all these techniques might be time- and resource-intensive, stimulating the development of data-driven Machine Learning (ML) models to anticipate fault content based on process parameters and sensor data helps to overcome their shortcomings.

Design of Experiment (DoE)

DoE is a statistical method designed to maximize the process or product under variation of several variables or parameters so enabling the choice of factors and ideal values for that process or product. The application of DoE is summed as follows: all conceivable combinations between the collection of parameters and the selected parameters, considered important, are varied from their lowest to greatest value. For instance, Figure 16 shows a three-parameter DoE with two tiers. The Figure 16 clearly depicts the three parameters selected with two levels (the minimum and the maximum), so producing eight possible test circumstances.

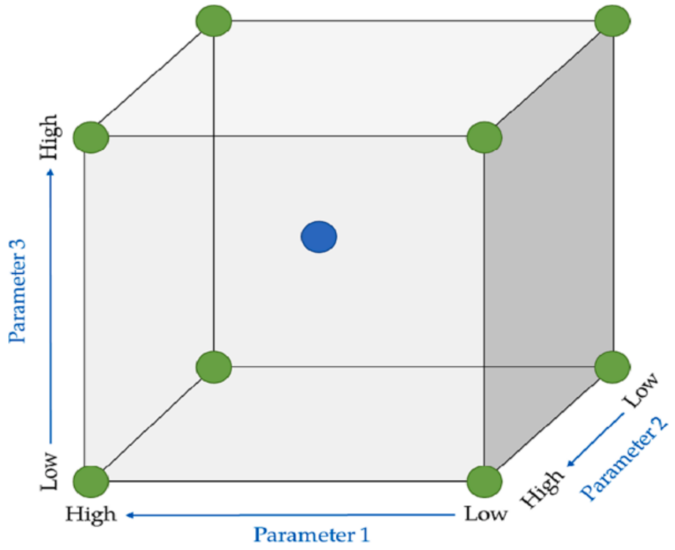

Figure 19. Exemplification of DoE of three parameters with two levels each.

There are several kinds of DoE techniques available, each with a different manner of major parameter analysis. Some types of DoE are: full factorial, Taguchi, Central Composite Design and Box-Behnken. Graphically, Figure 17 compares a DoE method on the left with the same data using RSM applied with a second-order polynomial model on the right: Using the RSM approach, it is visually simpler and faster to identify an optimal response for the analysis based on the provided example in Figure 17. (Pereira et al., 2023)

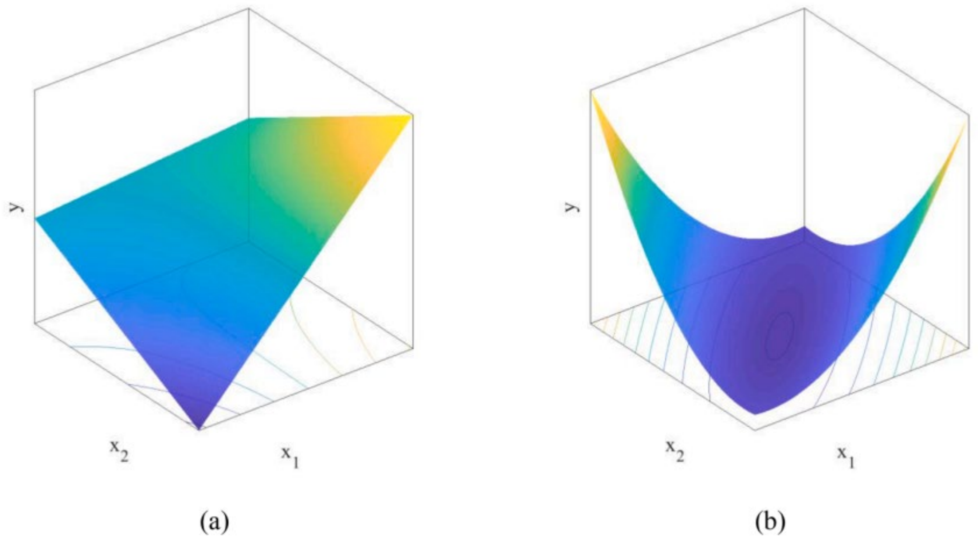

Figure 20 Examples of the (a) factorial and (b) RSM adjustments obtained by the DoE methodology.(Pereira et al., 2023)

DoE in AM

Rising as a breakthrough manufacturing tool with great promise is additive manufacturing (AM), sometimes known as 3D printing. To achieve ideal performance and quality in 3D printed goods, nonetheless, this calls on a complete awareness of the printing settings and their influence on the resultant good. This work presents a Design of Experiments (DOE)-based method to examine the impact of printing parameters on mechanical characteristics of 3D printed objects. The objective is to maximize these values to improve performance while reducing environmental impact, time, and material consumption. The bibliographic research sought to guide on which are the most investigated and pertinent printing parameters in the quality of the final part. Given the several characteristics for the definition of 3D printing, it was thus feasible to specify a reasonable range of initial parameters for investigation.

The chosen printing parameters are methodically changed in the experimental design to produce an extensive dataset for study. Tests follow to get the information. After that, the gathered data is subjected to the Analysis of Variance (ANOVA) technique to create behavioral equations and find important impacts. This helps us to grasp the links between the mechanical characteristics and the print settings more deeply.

The DoE approach is applied to specify several configurations once the parameters are established, and subsequently, the fabrication of the components starts. These were specimens for upcoming mechanical testing. Among the mechanical tests are bending, tension, and compression tests. It is then obtained from the mechanical tests, different mechanical properties in which they are inserted in Minitab® for a data analysis, collecting as results Pareto graphs showing which parameters have the most influence on the analyzed property, as well as an equation of the property's behavior.

By means of an optimization based on the behavior equations of every mechanical property, the ideal values for the various printing conditions are obtained, therefore enabling a more affordable and efficient future work.(Pereira et al., 2023)

Multi-objective optimization

Optimization is the practice of using generally computational, usually computational techniques to give the user the optimal response or solution for a particular condition. Where the aims and limits of the project are always taken into account, this response can be made of a single factor, or a mix of factors and values of the problem variables. Optimization is the process of minimizing (or maximizing) an objective function with constraints (Abraham & Jain, n.d.). The great majority of actual problems in the field of optimization are related to obtaining different goals that must be achieved simultaneously, which, thus, are usually conflicting and produce the non-existence of a single solution optimizing all the several goals. Multi-objective optimization problems, in which the analyst or project owner is in charge of studying and considering the aims and objectives, then allows the analyst or project owner to select one of the best solutions from the set offered by the optimization. Optimization is warranted since this approach always seeks and delivers good effects on results, such as economic, performance, competitive, quality, among others (Choze et al., 2022).

Non-Destructive Testing (NDT) in Metal Additive Manufacturing

With an emphasis on their capacity to identify particular faults, methodology, accuracy, restrictions, and applicability, this part summarizes the present state of several non-destructive testing (NDT) techniques applied in metal additive manufacturing (AM).

Acoustical Emission Testing (AE)

Acoustic Emission (AE) testing tracks transient elastic waves produced by fast energy release from confined sources like inclusions or fissures. Using frequency domain tools including Fast Fourier Transform (FFT), Wavelet Transform, and Local Mean Decomposition, these waves are acquired using sensors then examined. FFT offers a broad spectrum; wavelet transform solves this by allowing time-frequency localization, so lacking time resolution.

Signal frequency, noise, and material attenuation among other factors affect AE data. Thus, strong feature extraction techniques and preprocessing strategies are absolutely important. For internal flaws like cracks especially, AE testing provides real-time defect detection during AM operations. Its performance is shown in applications involving structural health monitoring and flaw detection in Ti-6Al-4V parts.

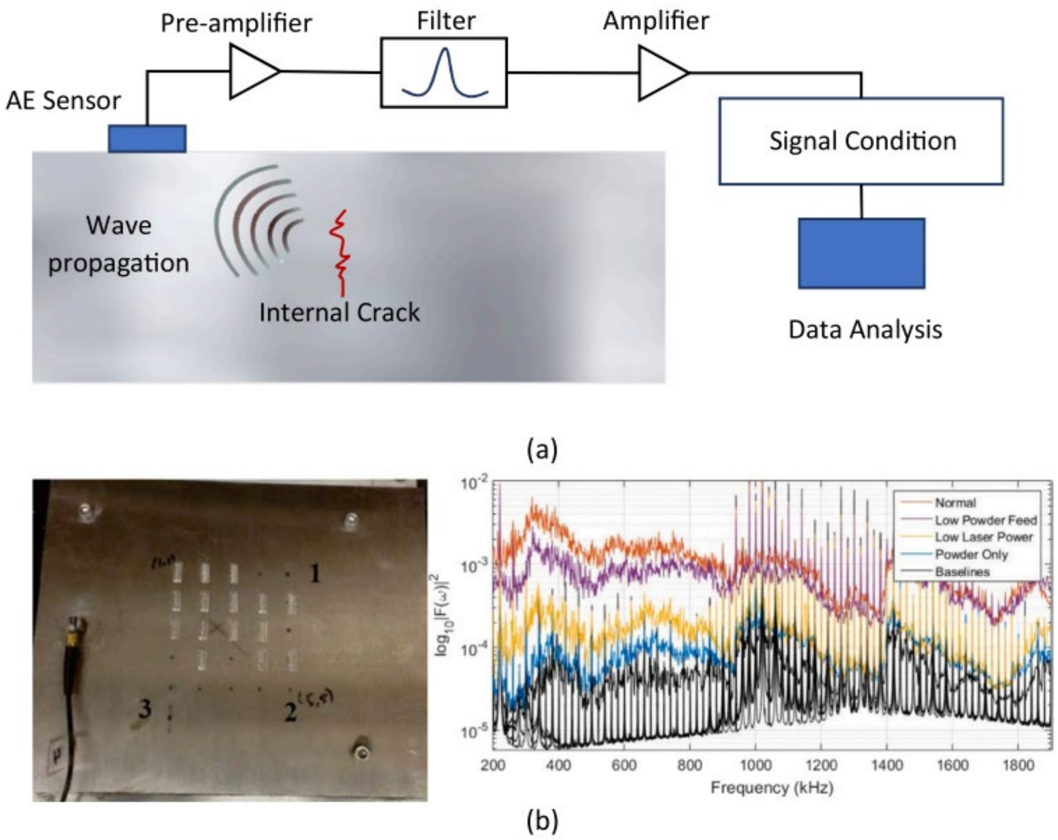

Figure 21 (a) AT procedure for internal fault detection; (b) Transducer placement on Ti-6Al4 V AM plate (left), average filtered power spectrum of the transducer taken in the passband for each of the five scenarios (right) (Segovia Ramírez et al., 2023a)

AE in AM suffers difficulties with noise sensitivity, sensor location, and sophisticated data processing notwithstanding its potential. To improve pattern identification, new methods call for convolutional neural networks (CNNs) and machine learning models. Ongoing areas of development are preamplification, transducer selection, and new sensor designs—e.g., air-coupled or ice-encapsulated.(Segovia Ramírez et al., 2023b)

Eddy Current Testing (ET)

Electromagnetic induction underpins Eddy Current Testing (ET). An alternating current flowing through a coil close to a conductive medium causes eddy currents in the material. Surface or near-surface flaws affect these and produce detectable changes in impedance.

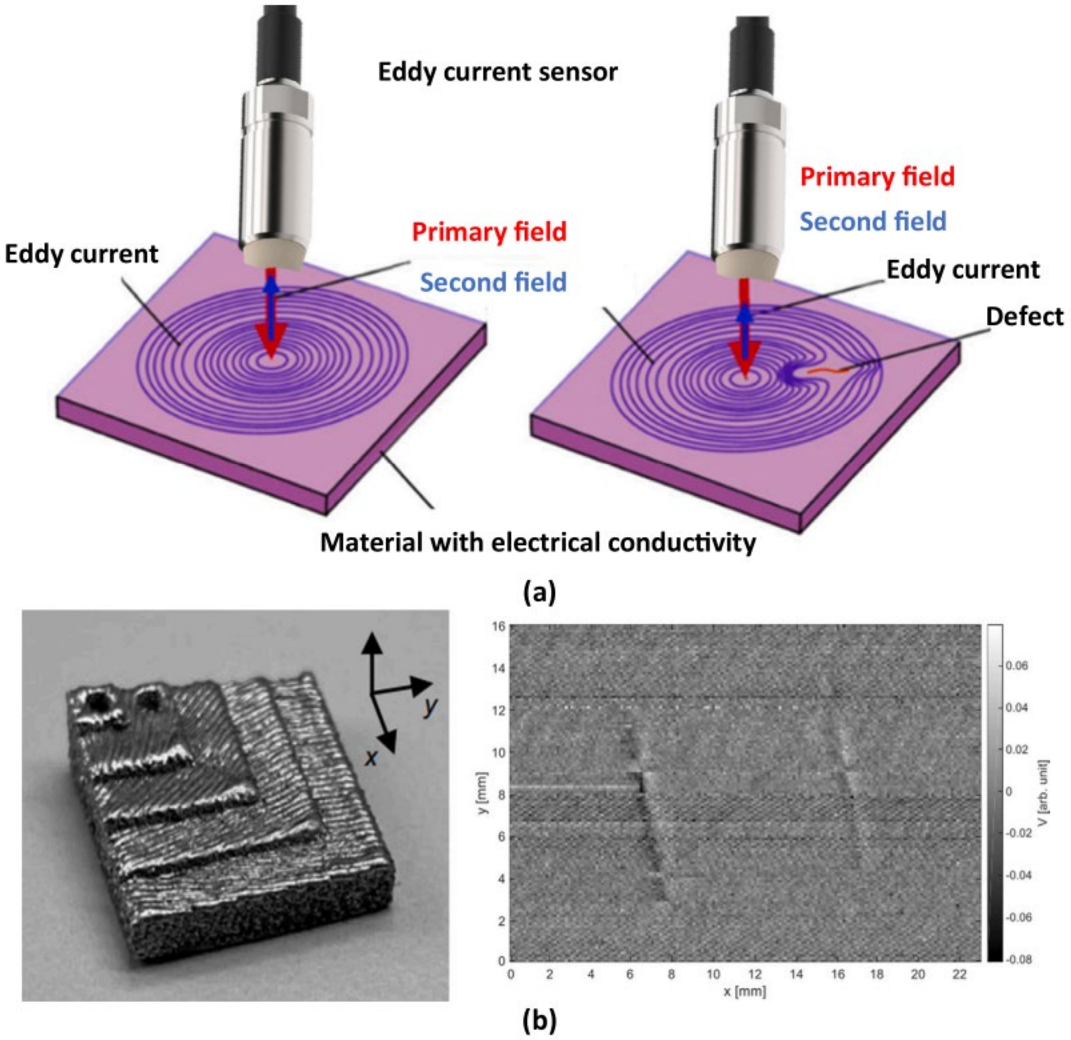

Figure 22 ET condition monitoring process; (a) Diagram for the measurement process. (b) Gas-atomized AM component for ET and ET amplitude image of one layer (Ehlers et al., 2022)

For conductive materials such as aluminum, steel, and zinc, ET is ideal. It is fast, non-contact, and relevant to complicated geometries. Its application is limited, nevertheless, by its sensitivity to surface roughness, material conductivity, and magnetic permeability fluctuations. In AM, variations in magnetic property and uneven surface finishes provide difficulties.

ET has been effectively used in powder bed fusion (PBF) and wire arc additive manufacturing (WAAM) systems despite these constraints. Depending on the material and frequency, typical detectable flaws run from 350 µm down to 5 mm. Multi-frequency configurations and signal processing advances are raising detection accuracy.(Ehlers et al., 2022)

Infrared Thermographic Testing (TT)

From the surface of a component, infrared thermography (TT) picks emitted infrared radiation to identify thermal irregularities brought on by subsurface flaws. Under Stefan-Boltzmann and Planck's equations, TT has low operating risk and quick inspection speed effective for real-time monitoring.

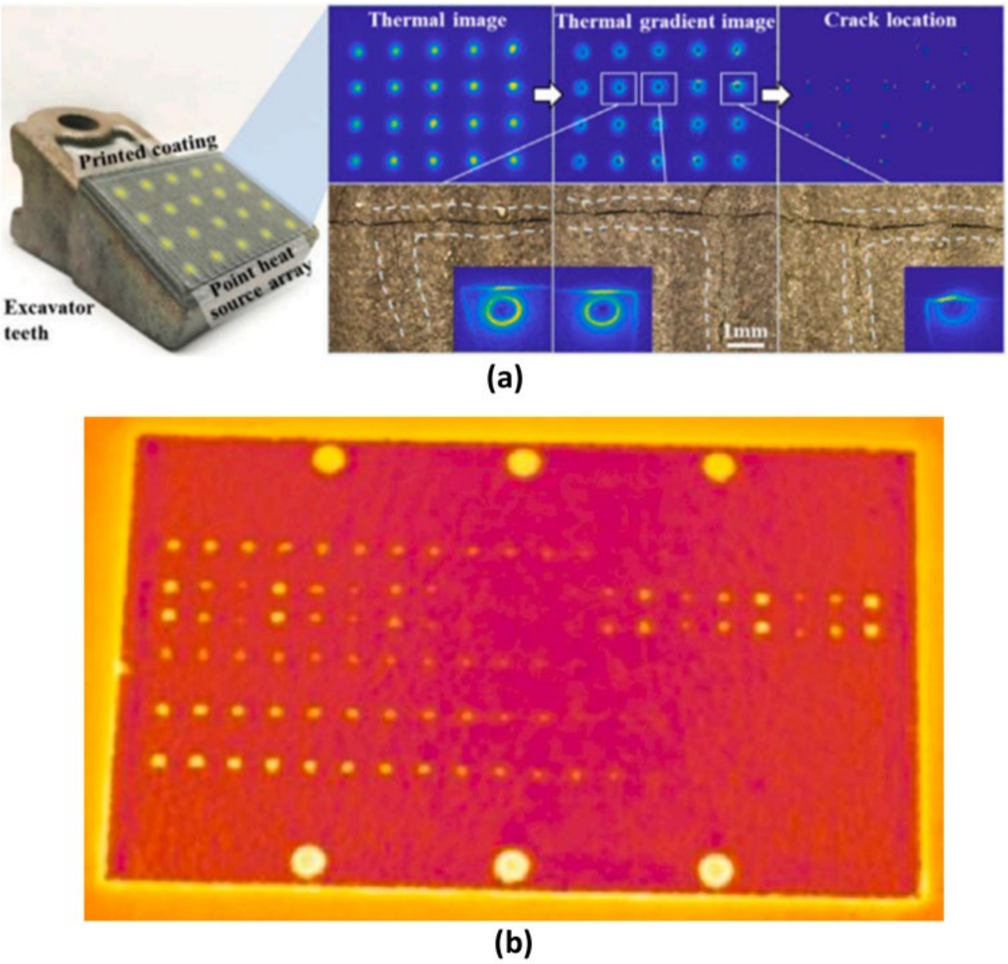

Figure 23 (a) Thermal image about showing crack location. (b) Thermogram of AM material (Mireles et al., 2015; Shi et al., 2021)

Thermographic cameras translate infrared radiation into temperature maps; but, limited resolution and sensitivity make minor flaws (<500 μm difficult to find. When looking at circular objects, image distortion can also result from the square pixel architecture of detectors.

By analyzing heat diffusion behavior, TT helps find delamination and vacancies. Defect contrast is improved in active thermography, in which external heat sources—such as ultrasonic waves or hot air—are used. Further helping to find defect signatures are pattern recognition systems.(Segovia Ramírez et al., 2023b)

Magnetic Testing (MT)

Surface and almost surface discontinuities in ferromagnetic materials are found via magnetic testing (MT). The technique consists of magnetizing the component and tracking magnetic flux leakage with magnetic particles.

Although MT is limited to ferromagnetic alloys including nickel and cobalt-based systems, accurate and reasonably priced for identifying fractures, inclusions, and voids. As such, its relevance in AM is limited, particularly considering the predominance of non-ferromagnetic materials like titanium.(Segovia Ramírez et al., 2023a)

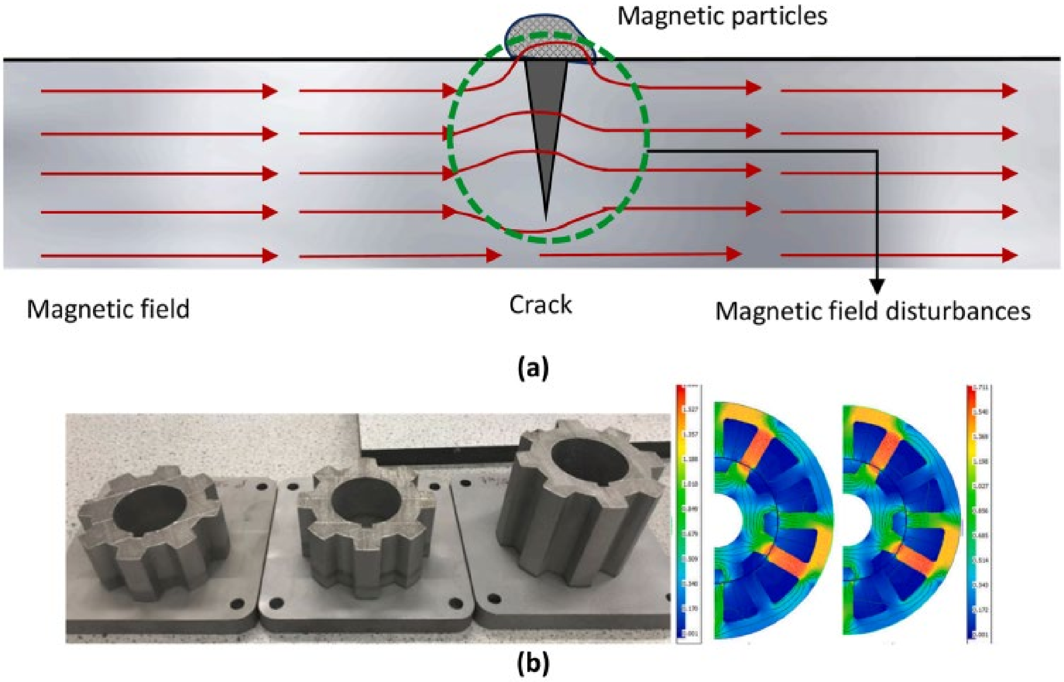

Figure 24 (a) Diagram of MT. (b) AM components and simulation of magnetic field lines (Segovia Ramírez et al., 2023b)

Penetrant Testing (PT)

Using colorful or luminous solutions that pass through surface-breaking flaws by capillary action, Penetrant Testing (PT) The surface is cleansed and a developer is used to extract the penetrant from defects, therefore rendering them visible following a dwell time.

Simple, cheap, and adaptable to many materials—metals, ceramics, plastics—PT is It is not appropriate for porous or very rough AM surfaces, though, and only picks surface flaws. There is little research on PT in AM; its value is usually less than that of volumetric techniques.(Segovia Ramírez et al., 2023a)

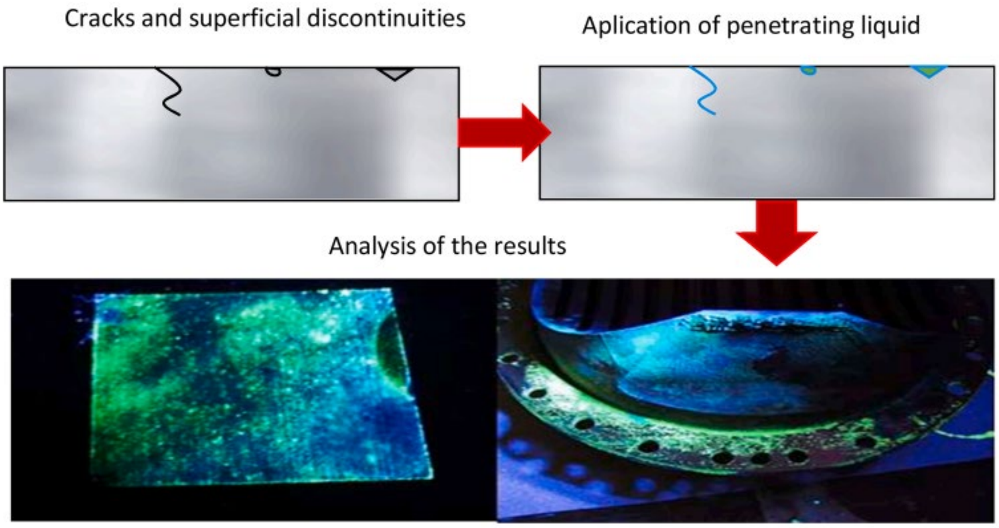

Figure 25 Diagram of PT.(Segovia Ramírez et al., 2023b)

Radiographic and Computed Tomography (RT & CT)

By use of density variations, radiographic testing (RT) images internal structures using X-rays or gamma rays. Although efficient, angular dependency and safety issues compromise RT's dependability.

Conversely, computed tomography (CT) provides high-resolution 3D imaging by voxel-based reconstruction and rotational X-ray projections. AM makes much use of it for porosity and crack identification. Among the most reliable NDT techniques, CT offers complete volumetric examination and can find flaws down to 10 µm depending on voxel size and material.

Data collecting time, cost, and less sensitivity in thick or dense areas are among the challenges. Current directions in study are noise suppression and advanced image processing—e.g., ML-based segmentation.(Segovia Ramírez et al., 2023b)

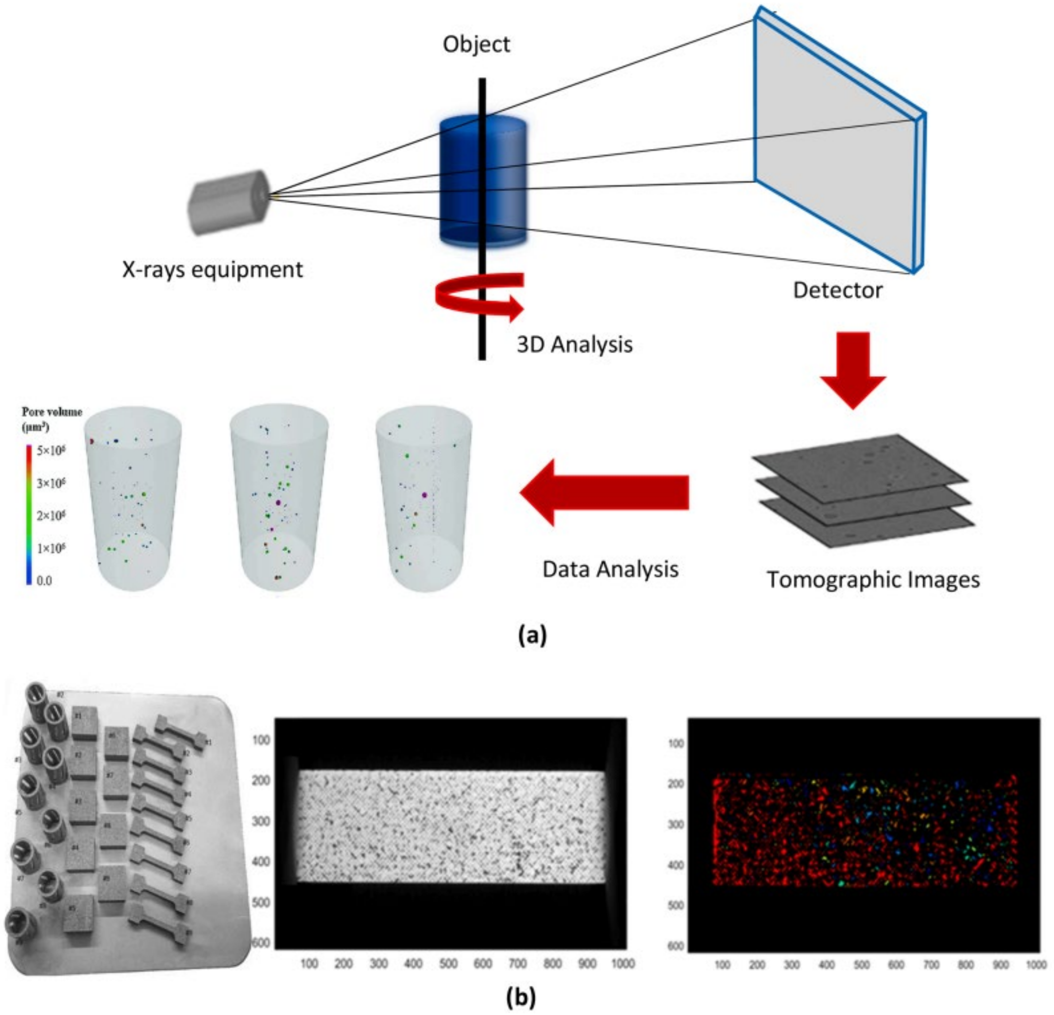

Figure 26 (a) CT procedure. (b) AM manufactured components in Ni-Mn-Ga alloy and reconstruction of CT images to detect porosity and inclusions (Ituarte et al., 2022)

Ultrasonic Testing (UT)

Sending high-frequency sound waves into a component, ultrasonic testing (UT) analyzes the reflected signals from flaws. It supports normal incidence pulse-echo, angle beam, and through-transmission among other modes.

With great sensitivity (defects as little as 50–100 μm), UT can identify porosity, fractures, and inclusions. It covers thick components and complicated geometries. Quantitative study is made possible by the link between ultrasonic velocity and porosity.

Among the new advancements are phased array systems, ice-coupled transducers, and immersion techniques. Finding flaws positioned parallel to the wave direction and deciphering results on rough AM surfaces still provide challenges. Under active development to increase dependability are Total Focused Methods (TFM) and other imaging techniques.

Every one of these NDT methods presents special benefits and drawbacks. Their interaction with real-time sensing and machine learning creates interesting directions for improved metal additive manufacturing quality assurance.(Segovia Ramírez et al., 2023b)

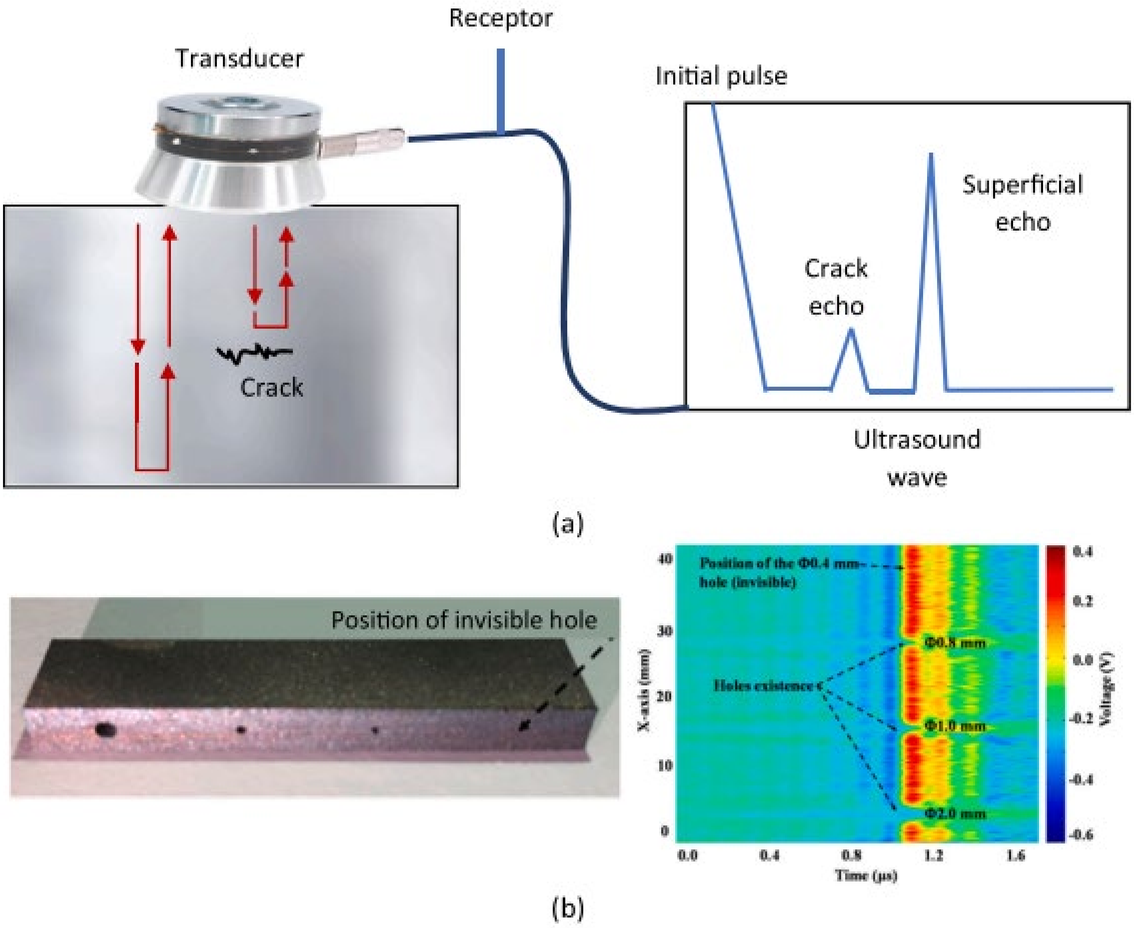

(a)

(b)

Figure 27 (a) Diagram about ultrasonic configuration to detect cracks with UT. (b) Real Ti-6Al4 V AM component for the tests and results of the UT (Yu et al., 2020)

Modal Analysis as a Non-Destructive Evaluation Tool in Metal AM

Modal analysis has attracted more and more interest among the non-destructive testing (NDT) techniques under investigation for quality assurance in metal additive manufacturing (AM) because of its cost-effectiveness, sensitivity to material properties, and possible for automation. Metal AM techniques such Selective Laser Melting (SLM) and Laser Powder Bed Fusion (L-PBF) naturally generate components with complicated geometries and process-dependent microstructures. Localized changes in the thermal history of the melt pool follow from variations in process parameters including laser power, scan speed, hatch spacing, and layer thickness. These temperature fluctuations influence microstructural evolution, hence producing heterogeneities in grain size, residual stress distribution, and defect development (e.g., porosity, absence of fusion, or unmelted powder)(Leuders et al., 2013). Consequently, the mechanical performance of the last part becomes sensitive to these criteria, which presents a major obstacle to standardizing and certifying especially in industries like aircraft and biomedical engineering. (West et al., 2017)

Although they provide high-resolution insight into interior structures, traditional defect characterisation techniques such as X-ray Computed Tomography (CT) are generally too costly, time-consuming, and challenging to scale for in-line investigation. By using the natural link between a structure's dynamic response and its physical characteristics, modal analysis offers a non-invasive and reasonably low-cost substitute. Natural frequencies, damping ratios, and mode shapes control the response of a structure under mechanical excitation—that of an impact or vibration. Particularly sensitive to the shape, material stiffness, mass distribution, and boundary conditions of the part are these modal characteristics.

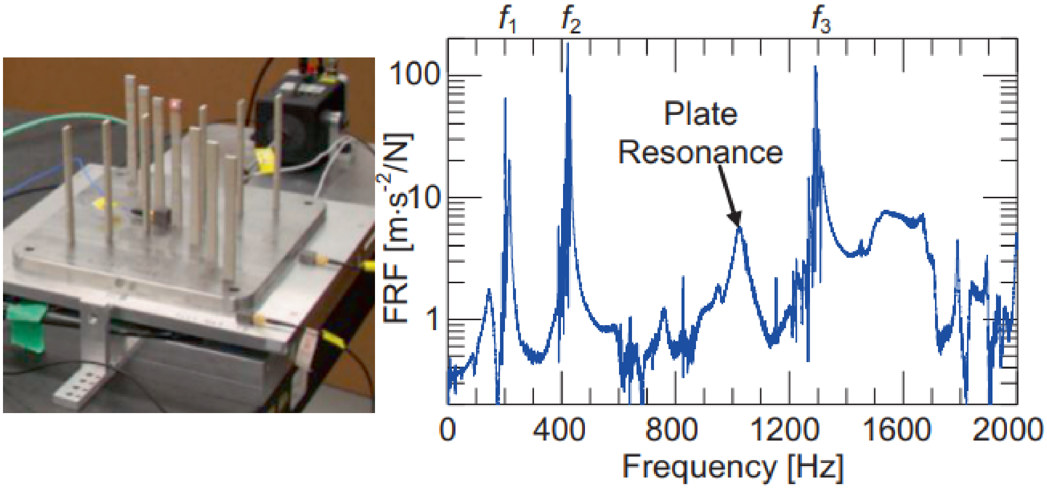

Figure 28 Photograph of modal test setup and representative FRF (West et al., 2017)

In the context of AM, flaws such as keyholes, delaminations, or sub-surface porosity cause localized mass and stiffness decrease that modulates the resonance frequencies and mode forms of the component. Therefore, one can deduce the existence, degree, and maybe the position of such flaws by doing experimental modal analysis (EMA) and matching the measured modal parameters to defect-free reference models or finite element simulations. Recent studies have confirmed that this method can identify even small variations in microstructure or density, which are generally connected with mechanical performance deterioration (Gebhardt & Hötter, 2016).

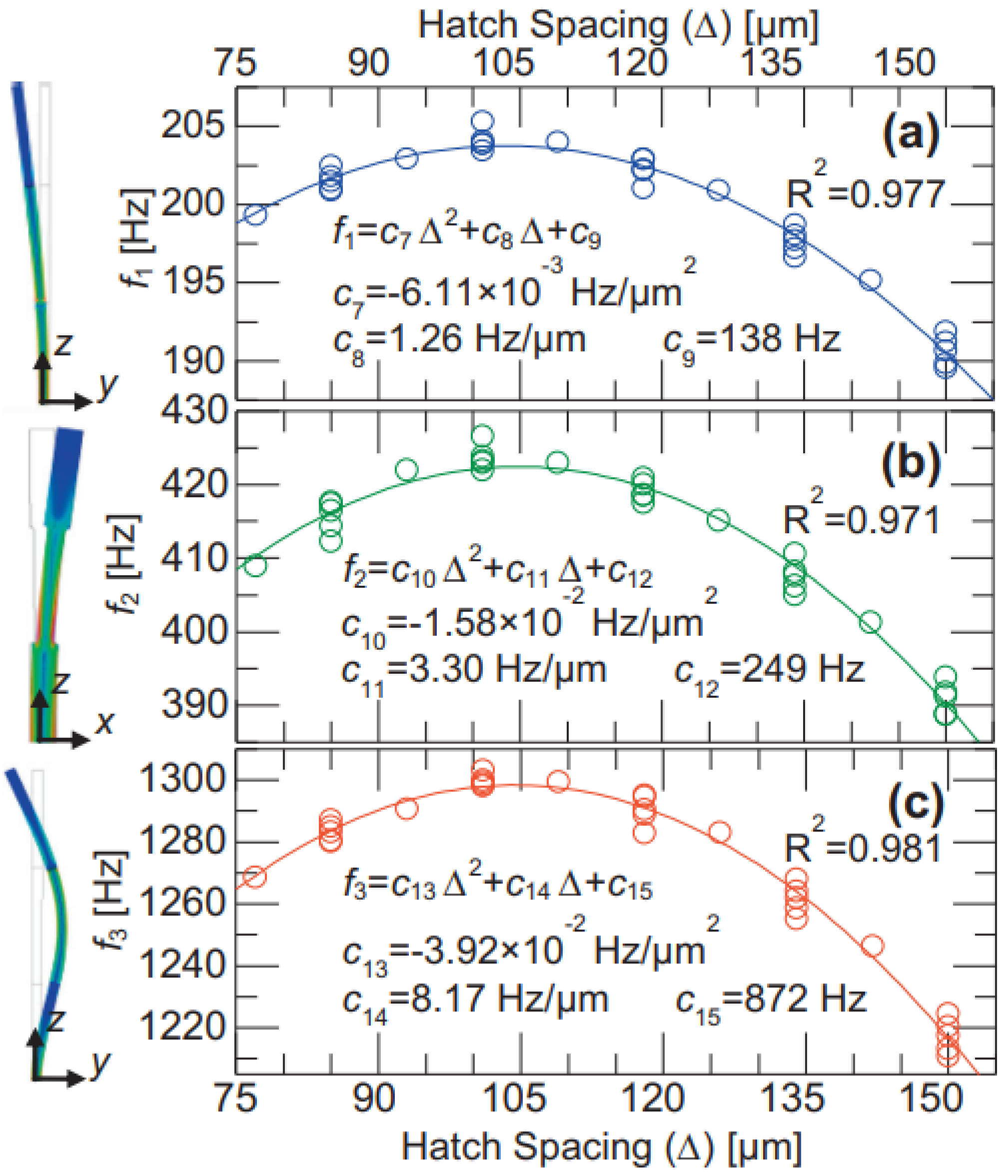

Figure 29 Natural frequency of first three modes of a beam as function of hatch spacing, with associated modes as insets.(West et al., 2017)

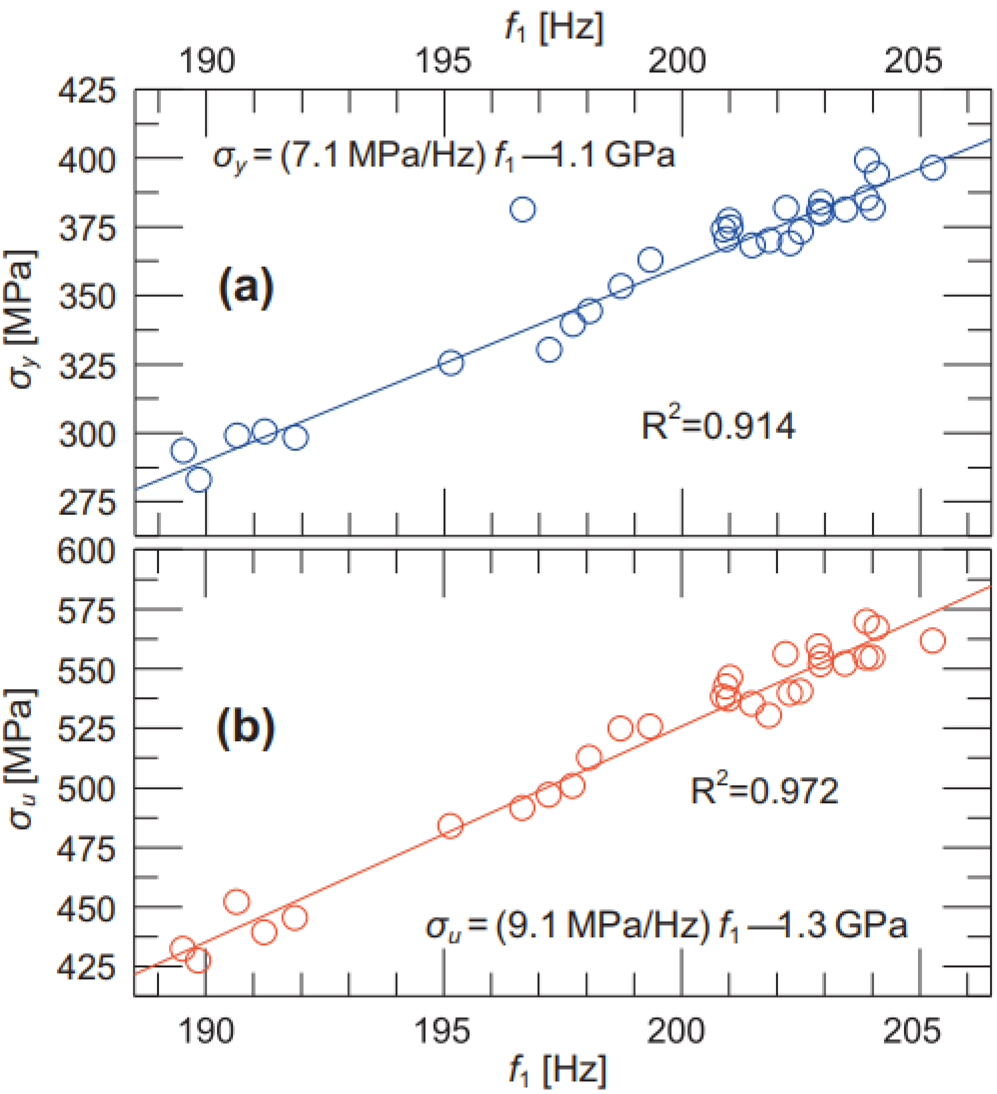

Figure 30 Yield strength and ultimate strength of a beam as functions of first mode natural frequency.(West et al., 2017)

Moreover, indirect assessment of mechanical properties can also be accomplished by modal analysis. Changes in resonant frequencies have been found to be quantitatively connected in metal AM samples to changes in Young's modulus, yield strength, and ultimate tensile strength. Particularly when destructive testing is not practical due to part cost or manufacturing volume limitations, this link creates opportunity for adopting modal testing as a surrogate tool for mechanical testing (Tapia & Elwany, 2014). To track layer-wise changes in the construction, modal analysis can also be used either ex-situ, following the part's fabrication, or perhaps in-situ employing embedded sensors and real-time data collecting methods.

The fact that modal analysis fits machine learning (ML) methods is among its most intriguing features. Supervised learning models can be taught to estimate mechanical performance directly from modal response data by compiling a database of modal parameters and associated known fault states or mechanical attributes. This combination of modal testing and ML lays a basis for smart, autonomous quality control systems in AM—capable of fast screening and certification of printed components without significant post-processing.

Modal analysis is not without restrictions notwithstanding these benefits. It calls for exact mode identification—especially in complicated geometries—strong control of boundary conditions during testing, and enough spatial resolution to identify pertinent modes. Furthermore, intrinsically connected to the size, kind, and location of the anomaly relative to the modal deformation fields is defect detectability. Still, modal analysis is fast becoming a useful and potent method for NDT in metal AM as excitation and sensing equipment—such as laser Doppler vibrometers and instrumented hammers—alongside signal processing and ML-based interpretation with increasing precision.

Non-destructive evaluation: machine learning approaches

Many factors affecting component quality influence additive manufacturing (AM) techniques. To guarantee part integrity and reduce failure, the sector is thus turning towards predictive fault detection and condition-based monitoring (Farrell & Deering, 2018). Though the terms Non-Destructive Testing (NDT) and Non-Destructive Evaluation (NDE) have been used synonymously historically, a clear differentiation is required. NDT mostly consists in the gathering of unprocessed diagnostic data free of interpretation. Conversely, NDE uses data analysis to define defect processes, therefore offering information on size, form, and type of damage (Obaton et al., 2020).

With integrated monitoring and computational evaluation, NDE can be seen as a development of NDT including diagnostic and prognostic powers. Leveraging materials science, statistics, and computer science, this multidisciplinary approach supports condition-based maintenance and lifetime evaluation (Bond, 2014). New technologies and advanced algorithms are progressively being included into NDE techniques to improve fault identification and enable service-life extension in AM components.

Review of state-of- the-art NDE in AM is given in this part, which offer the most varied and fast developing set of tools for AM quality assurance(García Márquez & Peinado Gonzalo, 2022).

5. Machine Learning in NDE for AM

ML includes supervised, unsupervised, and reinforcement learning among other methods able to extract patterns from challenging datasets. For classification, grouping, regression, and optimization challenges these techniques are extensively used. Parameter optimization, defect categorization, quality prediction, and cost reduction in AM depend critically on ML

5.1 Support Vector Machine (SVM)

In AM, SVM has great application in both classification and regression problems. It optimizes the margin between data by spotting a hyperplane separating them into groups. Non-linear data is handled using kernel functions including sigmoid, linear, and Gaussian ones. Particularly with image-based data from visual or CT inspections, SVM shines in porosity and fault classification.

With SVM using CT scan data, Gobert et al. (Gobert et al., 2018) found part discontinuities and improved classification accuracy by 20%. Using SVM for VT inspection, Zhang et al.(Zhang et al., 2018) claimed 90% accuracy; CNN somewhat exceeded this at 93%. To improve classification resilience, SVM has also been coupled with optimization methods as OCA.

5.2 Artificial Networks (ANNs)

With enough training, ANNs model non-linear relationships between inputs and outputs, hence attaining excellent classification accuracy. Most often used architectures are convolutional neural networks (CNNs) and multilayer perceptron (MLP). Comprising convolution, activation, and pooling layers, CNNs are particularly suited for image-based analysis.

In AM data analysis, Baturynska et al. (Baturynska et al., 2019) revealed MLP performed somewhat worse than CNN; nonetheless, CNN showed great promise given suitable datasets. CNN with wavelet-transformed AE data allowed Hossain and Taheri (Hossain & Taheri, 2021) 96% classification accuracy. Using wavelet-based AE signal encoding, Shevchik et al. (Shevchik et al., 2018) presented Spectral CNN (SCNN), hence improving categorization. For AM NDE applications, CNNs provide outstanding accuracy and minimal computing costs.

5.3 Deep Belief Network (DBNs)

DBNs can learn unsupervised and comprise stacked Restricted Boltzmann Machines (RBMs). Using DBN, Ye et al. (Ye et al., 2018) showed 96% accuracy in denoised acoustic data classification, above MLP and SVM. Ye et al. (Ye et al., 2018) obtained 83.4% accuracy by using DBN to VA imaging as well. These experiments imply DBNs are useful for AM real-time fault monitoring.

5.4 K-Means Clusterings

Unsupervised clustering method K-Means divides data into groups according to Euclidean distance. It works well for image data segmenting and acoustic signal classification. Wu and colleagues (Wu et al., 2016) categorized AM layer failure modes using it. Combining K-Means with PCA, Grasso et al. (Grasso et al., 2017) found overheating areas in picture data, therefore obtaining strong fault segmentation.

5.5 Particle Swarm Optimization (PSO).

Inspired by swarm behavior, PSO is a global optimizing technique. It helps to maximize ANN architecture and processing limits effectively. For flaw detection, Jian et al. (Jiang et al., 2020) used a PSO variant in UT and wavelet-transformed AE data, hence increasing accuracy by about 10%. Though PSO has strengths, its success mostly relies on dataset properties and parameter adjustment.

5.6 PCA—the principle component analysis

PCA is a dimensionality reduction method converting correlated information into orthogonal components. ML pipelines make extensive use of it for preprocessing and feature extraction. For VA image data, Zhang et al. (Zhang et al., 2018) enhanced SVM classification accuracy by use of PCA. Successfully spotting local hotspots, Grasso et al. (Grasso et al., 2017) merged PCA with K-Means for thermal picture clustering. Often coupled with supervised classifiers to boost performance and cut computation time, PCA increases ML model efficiency.

Materials and Methods

Sample Modeling

First, the particular machine handled the production; the CAD files were designed for sample modeling. The procedures started with the building of the CAD files, which modeled for each component 96 cubes and CD files. Figures 31 show the exact sample measurements. Pre-selected process parameters for every component were entered at this stage using Materialize Magics. It is important to realize that every component received a certain laser speed, laser power, and hatch distance, which produced distinct characteristics for every component once it was produced.

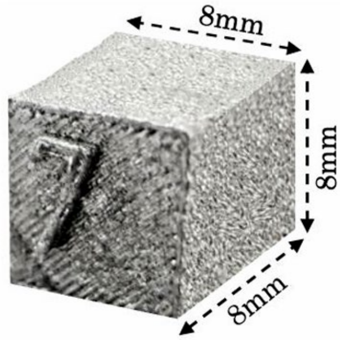

Figure 31 Nominal dimension of the cubic samples

Design of experiment

The Design of Experiment (DoE) covers all the process parameter values applied in this work. There are various parameters one can change before beginning the L-PBF procedure. These values are the required machine settings for component production from powders. These four kinds of process parameters help to simplify things: laser related, scan-related, powder-related, and temperature-related ones. Laser power, wavelength, spot size, pulse length, and pulse frequency are among the laser-related properties. Scan-related properties include hatching distance, scan speed—the speed of scanning—and the particular pattern utilized for scanning. Particle size and distribution, particle shape, powder bed density, layer thickness, and material characteristics define the elements related to powder. Among the temperature-related features are the powder bed's temperature, the powder feeder's temperature, and the consistency of temperature. Improving the quality of products depends on the suitable process parameters being chosen. The interaction of these elements is crucial to underline since sometimes changing one parameter yields the same effect as changing another. Usually, one should keep a balance between all the criteria. The major objectives of this thesis research are to maximize production rate and improve quality of the output; so, it is imperative to select the ideal process parameters. Although every process element influences the effectiveness of the process, only the most important people were taken into account to get the intended outcomes. Table 3 reports three process parameters: laser power (P), laser speed (v), and laser hatch distance (h), from which 64 experimental data points were chosen in consideration. Our knowledge of the machine and an unpublished preliminary analysis guided the choice of process parameters. These process parameters were then defined using EP Hatch Prima software, producing 64 unique Cam and CLI files. Table 3 lists the laser power as between 100 and 340 W; the scan speed and hatch distance ranged from 400 to 1000 mm/s and from 0.1 to 0.2 mm, respectively. The great range of values resulted in a significant change in an appropriate term called volumetric energy density (VED), which measures the input energy per unit volume of the powder bed. Originally proposed in references, the idea of VED was first shown to have significant relevance by means of comparison between several sets of parameters. The relative density of materials processed using L-PBF is assessed in this thesis using VED, first indicated in Equation 1, where:

VED = Volumetric energy density [J / mm^3]

P = Laser power [J]

v = Scanning speed [mm/s]

h = Hatching distance [mm]

l = Layer thickness [mm]

Table 1 Process parameters used to print each samples

Sample	Power [W]	SS [mm/s]	HD [mm]	Layer thickness [mm]	VED [J/mm3]
1	100	400	0.1	0.03	**83**
2	100	400	0.11	0.03	**76**
3	100	400	0.12	0.03	**69**
4	100	400	0.13	0.03	**64**
5	100	600	0.1	0.03	**56**
6	100	600	0.11	0.03	**51**
7	100	600	0.12	0.03	**46**
8	100	600	0.13	0.03	**43**
9	100	800	0.1	0.03	**42**

10	100	800	0.11	0.03	**38**
11	100	800	0.12	0.03	**35**
12	100	800	0.13	0.03	**32**
13	100	1000	0.1	0.03	**33**
14	100	1000	0.11	0.03	**30**
15	100	1000	0.12	0.03	**28**
16	100	1000	0.13	0.03	**26**
17	150	400	0.1	0.03	**125**
18	150	400	0.11	0.03	**114**
19	150	400	0.12	0.03	**104**
20	150	400	0.13	0.03	**96**
21	150	600	0.1	0.03	**83**
22	150	600	0.11	0.03	**76**
23	150	600	0.12	0.03	**69**
24	150	600	0.13	0.03	**64**
25	150	800	0.1	0.03	**63**
26	150	800	0.11	0.03	**57**
27	150	800	0.12	0.03	**52**
28	150	800	0.13	0.03	**48**
29	150	1000	0.1	0.03	**50**
30	150	1000	0.11	0.03	**45**
31	150	1000	0.12	0.03	**42**
32	150	1000	0.13	0.03	**38**
33	200	400	0.1	0.03	**167**
34	200	400	0.11	0.03	**152**
35	200	400	0.12	0.03	**139**
36	200	400	0.13	0.03	**128**
37	200	600	0.1	0.03	**111**
38	200	600	0.11	0.03	**101**
39	200	600	0.12	0.03	**93**
40	200	600	0.13	0.03	**85**
41	200	800	0.1	0.03	**83**
42	200	800	0.11	0.03	**76**
43	200	800	0.12	0.03	**69**
44	200	800	0.13	0.03	**64**
45	200	1000	0.1	0.03	**67**
46	200	1000	0.11	0.03	**61**
47	200	1000	0.12	0.03	**56**
48	200	1000	0.13	0.03	**51**
49	250	400	0.1	0.03	**208**
50	250	400	0.11	0.03	**189**
51	250	400	0.12	0.03	**174**
52	250	400	0.13	0.03	**160**
53	250	600	0.1	0.03	**139**

54	250	600	0.11	0.03	**126**
55	250	600	0.12	0.03	**116**
56	250	600	0.13	0.03	**107**
57	250	800	0.1	0.03	**104**
58	250	800	0.11	0.03	**95**
59	250	800	0.12	0.03	**87**
60	250	800	0.13	0.03	**80**
61	250	1000	0.1	0.03	**83**
62	250	1000	0.11	0.03	**76**
63	250	1000	0.12	0.03	**69**
64	250	1000	0.13	0.03	**64**
65	300	400	0.1	0.03	**250**
66	300	400	0.11	0.03	**227**
67	300	400	0.12	0.03	**208**
68	300	400	0.13	0.03	**192**
69	300	600	0.1	0.03	**167**
70	300	600	0.11	0.03	**152**
71	300	600	0.12	0.03	**139**
72	300	600	0.13	0.03	**128**
73	300	800	0.1	0.03	**125**
74	300	800	0.11	0.03	**114**
75	300	800	0.12	0.03	**104**
76	300	800	0.13	0.03	**96**
77	300	1000	0.1	0.03	**100**
78	300	1000	0.11	0.03	**91**
79	300	1000	0.12	0.03	**83**
80	300	1000	0.13	0.03	**77**
81	350	400	0.1	0.03	**292**
82	350	400	0.11	0.03	**265**
83	350	400	0.12	0.03	**243**
84	350	400	0.13	0.03	**224**
85	350	600	0.1	0.03	**194**
86	350	600	0.11	0.03	**177**
87	350	600	0.12	0.03	**162**
88	350	600	0.13	0.03	**150**
89	350	800	0.1	0.03	**146**
90	350	800	0.11	0.03	**133**
91	350	800	0.12	0.03	**122**
92	350	800	0.13	0.03	**112**
93	350	1000	0.1	0.03	**117**
94	350	1000	0.11	0.03	**106**
95	350	1000	0.12	0.03	**97**
96	350	1000	0.13	0.03	**90**

Manufacturing the 96 cubic samples to offer a more comprehensive examination on VED, process parameters, and porosity development, see Table 2.

Table 2 DOE: Selection of process parameters used to print the samples

Power	SS	HD
100	400	0.1
150	600	0.11
200	800	0.12
250	1000	0.13
300		
350		

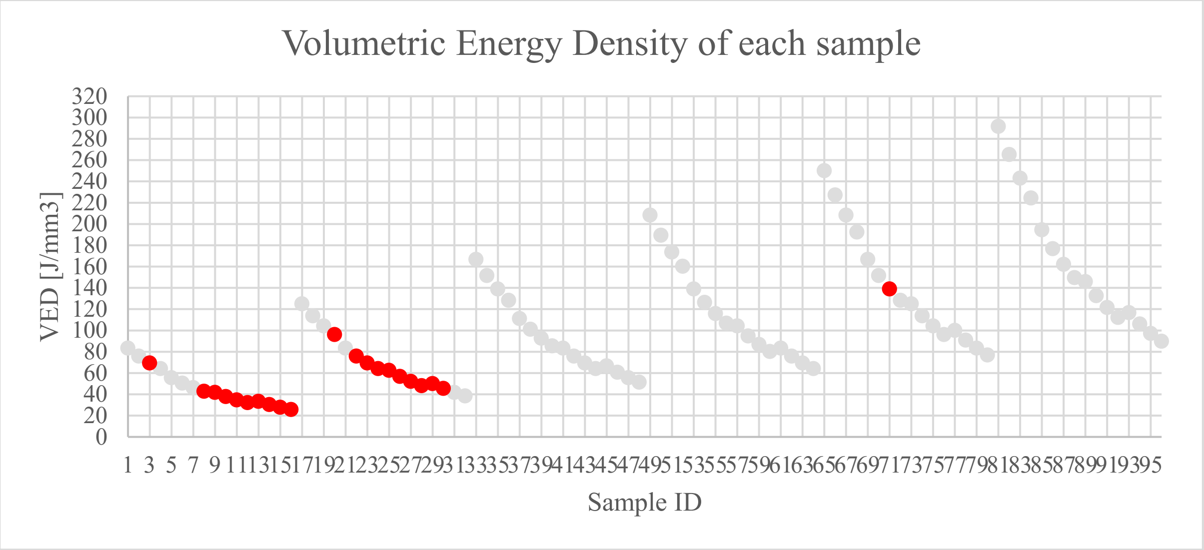

Figure 32 Schematic of VED trend to print each sample (Red: failed during printing)

During the printing process, 21 samples were failed. Resulting in a total of 75 successfully printed.

Samples Manufacturing

The PrintSharp 250 (Fig. 33) PBF machine meant for medium- volume operations generated the samples. It provides tremendous flexibility in terms of part management and is especially meant for the industrial production of sophisticated components. Table 3 details the machine's technical characteristics.

Figure 33 Prima Additive Print Sharp 250

Table 3 The technical parameters of the PrintSharp 250

Category	Specification
Dimensions (LxWxH)	3500 (L)- 1100 (W)- 2450 (H) mm
Weight	2000 kg
Power Supply	380 V/50 Hz/8kW
Type of laser	Yb (Ytterbium) Fiber Glass
Laser Power	200 W/ 500 W (Optional)
Laser Focus Diameter	70 – 100 µm
Beam Wavelength	1060 – 1080 nm
Building Volume	250 x 250 x 300 mm
Beam Deflection Speed	8 m/s
Positioning Speed	10 m/s
Build rate	12 – 30 cm³/h
Layer Thickness	0.02 – 0.1 mm
Layer Width	0.1 mm (single line width)
Recoater Specs	Travel: 650 mm
Building Platform z-axis	Travel: 300 mm/Speed max : 6 mm/s/Res: 0.01 mm
Heating Platform	Up to 200°C
Monitoring of O₂ Level	Below 100 ppm
Permissible Room Temperature	15 – 30°C
Gas (Consumption – running/filling)	7 l/min (running)
System Fill Consumption	20 l/min (up to filling)
Cam Software	Materialise Magics
Control & Other Software	Eplus control software (EPC)
Industrial Interfaces	Ethernet

The materials used were gas-atomized AISI316L stainless steel powder, supplied by Oerlikon. Before starting the production process, the build chamber was thoroughly emptied to a residual oxygen level of less than 0.1%. High-purity Argon was used to preserve an inert atmosphere within the construction chamber and minimize the likelihood of oxidation. A scanning approach was employed using a bidirectional stripe scanning pattern with a 67° rotation between each succeeding layer. The layer thickness of all samples was set to 30µm in this project [180].

In Fig. 33, the highlighted section illustrates the laser in operation during the LPBF process. The laser accurately melts a small layer of metal powder to create the desired shape. The process of melting is fundamental to LPBF, as it enables the fabrication of complex and highly 58 accurate metal parts through the sequential deposition of layers. Fig. 33 illustrates the manufactured samples on the building platform after the completion of the building process. After completing the production process, all parts stuck to the building platform were removed from the workspace and meticulously cleaned. Finally, the samples were cut from the platform employing a Wire Electrical Discharge Machine (W-EDM). It is worth noting that the samples were labeled during the production with a numerical value (sample ID in Table 3) to signify their distinct process parameters. The x-axis corresponds to the recoater orientation, while the z-direction aligns with the building direction.

Sample characterization

First, the W-EDM was used to separate the parts from the platform. Then, the density of the components was determined using an Archimedes balance. After conducting density measurements and analysis, specific components were chosen for tomography and metallography analysis. Finally, the microstructure of these samples was analyzed using an optical microscope for metallography data and the VGStudio software for XCT data.

Cutting Machine

At this specific step, the samples were chopped using the G.cut WEDM machine. Fig. 34 shows this machine. Section 1 matches the cutting machine's software interface, where the auto process, wire movement settings, start and stop buttons for cutting management are handled. Section 2 shows the X, Y, and Z coordinate directions, which help to guarantee the cutting is carried out in the proper orientation. The machine consists mostly in Section 3, where the cutting action is performed and the workpiece is positioned. The platform has to be clamped-attached to the W-EDM to initiate the process. The reference point for the x and y coordinates was then created by surface touching the wire and the platform using the particular program running on the computer attached to the machine. The machine loaded the suitable dimensions and precise orientation after changing the exact place for the wire beginning point to start the cutting action. At last, the printed parts were divided and ready for more work.

Figure 34 Key components of the WEDM machine: Section 1 (software controls), Section 2 (coordinate display), and Section 3 (cutting area).

The wire-cutting machine cuts the samples with the best accuracy using an electrically charged thin wire. This technique generates electrical discharges between the wire and the workpiece, hence progressively eliminating material along the cutting direction. The quick and effective production of the sparks, as depicted in Fig. 35, removes little amounts of metal and produces the intended workpiece form. Deionized water is continuously flowing to cool the workpiece and wire during the cutting process, therefore preventing too much heat and eliminating the eroded particles. Water is thus also utilized as a dielectric, which is necessary for the occurrence of the electrical discharge process. The terms "time on" and "time off" relate to the length of the on-time electrical pulses and the off-time gaps between them correspondingly. The parameter "ton" controls the energy and length of every spark, therefore affecting the surface quality and cutting speed directly. Conversely, "toff" reduces the possible thermal damage by allowing a limited cooling interval, therefore improving the cutting process's accuracy. Maximizing the cutting efficiency and guaranteeing the great quality of the final product depend on these criteria.

Archimedes density

The relative densities of SLM generated are found using the Archimedes method. This technique weights one sample in two different fluids. Usually, air is the fluid used in reference. The second fluid is distilled water, acetone—or ethanol. Although distilled water is usually used, the possible development of air bubbles on the sample surface may make it only sometimes suitable. This phenomena is especially observed in lattice structure components when air bubbles stop the whole entry of water into the interior of the mesh due to the high surface tension of the water. The Archimedes density measuring technique was applied for every sample in order to compute its geometrical and Archimedes density per ASTM F3637-23. First the measuring chamber is set ready, and the beaker is filled with 0.997 g distilled water. The device is then precisely calibrated to gauge the dry weight (w_{dry}) of the sample as shown in Fig. 35 (part 1). Once the sample's dry weight is known, it shows on the digital monitor as shown in Fig. 36, part 3. After completing this operation, the device is reset to a zero value and the sample is positioned on the filter, as shown in Fig. 35 part 2, to be totally submerged in distilled water. The sample was totally submerged in the water after all the bubbles produced were removed. By now the weight was recorded as $w_{immersion}$. The sample was then taken from the water, laid on the wet wipes, and quickly reweighed as indicated in Fig. 35 (part 1) to determine the absorption level of the water. This step produced the wet weight, denoted w Wet. Moreover, using the relative approach, the theoretical density of the powder was set to be 8.1 $g/\mathrm{cm}3$. After that, using the specified equations, the relative Archimedes density percentage and total porosity percentage for every sample were calculated:

$$\rho_{Archimedes} = \rho_{liquid} \cdot \frac{W_{dry}}{W_{dry} - W_{immersion}}$$

$$\rho_{Geometrical} = \rho_{liquid} \cdot \frac{W_{dry}}{W_{wet} - W_{immersion}}$$

$$\text{Total Porosity Percentage} = \frac{\rho_{theoretical} - \rho_{bulk}}{\rho_{theoretical}} \cdot 100\backslash\%$$

$$\text{Relative Archimedes Density Percentage} = \frac{\rho_{Archimedes}}{\rho_{theoretical}} \cdot 100\backslash\%$$

Where:

$\rho_{archimedes}$ = Archimedes density (apparent density) [g/cm^3]

$\rho_{geometrical}$ = Geometrical density (bulk density) [g/cm³]

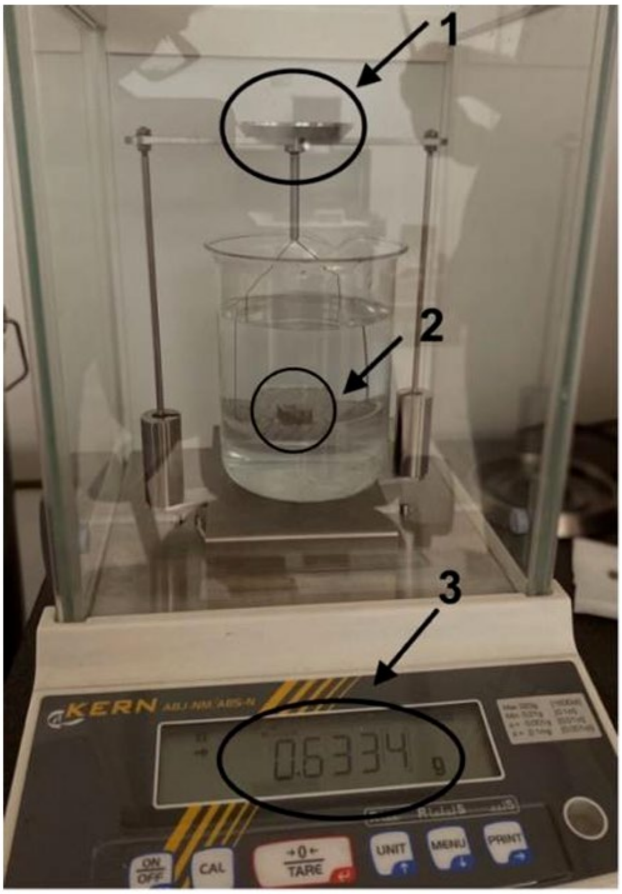

Figure 35 The illustration of the measurement setup for Archimedes density is 1) a position for measuring the dry and wet weight, 2) place for measuring the immersion weight, and 3) a digital display for showing the weight values.

X-Ray Computed Tomography

Combining multiple X-ray images captured around a rotational axis, XCT uses algorithms to build 3-D representations. Three main XCT methods have emerged recently, each improving data collecting speed. Initially, the XCT technique gathers density information along each beam of X-rays linearly displaced in the opposite direction of an X-ray detector. Until a complete 360° of data is obtained, the scanner turns in a little increment repeatedly. Using a two-dimensional X-ray array covering the whole object width and a one-dimensional detector array positioned at the X-ray beam edges, the second technique employs The third method uses a two-dimensional detector with a fully three-dimensional X-ray beam cone. The beam scanner moves its x-ray source and detector in a straight line to scan a slice of the xy plane. This is repeated since the source and detector show little movements in the z-axis for the measured object. Whereas the cone beam scanner reveals the object whole, the fan beam scanner simultaneously exposes a whole slice of it. Every scanning technique has a complete 360°

rotation to cover the whole object. Figure 37 lists every XCT method. XCT assessments center on image quality, most especially contrast and resolution. X-ray penetration lowers resolution and so reduces the maximum magnification of XCT pictures by object size. Reducing magnification alters scan voxels and compromises image clarity. Measuring high-density materials becomes challenging with low X-ray penetration, which also limits object size. This is so because consistent contrast calls for longer exposures. XCT scanners measure a specific region or utilize a reference coupon with similar characteristics rather than scanning the full product. Image quality gains from this. This method might improve scan quality but neglect to catch the object of interest, therefore biassing the results.

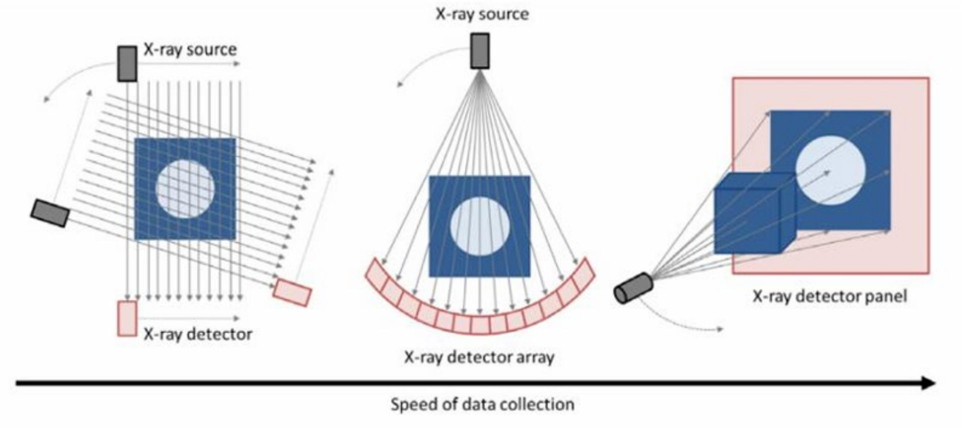

Figure 36 Three different beam XCT schematics. The fan beam image shows a curved detector, whereas the cone beam image shows a flat panel detector. All of these schematics can be employed in each case.

Archimedes density measurement data led eleven samples to be selected for XCT study. Tomographic technique analysis of these samples allowed their porosity percentage and density to be determined, which would be compared with other techniques. Furthermore, we gathered thorough information on porosity distribution, geometries of porosities, their diameters, and other pertinent characteristics; these will be discussed in the section on results and discussion. Initially, the samples were arranged on the holder according to this technique as shown in Fig. 38(a). A copper filter was placed before the X-ray gun in Fig. 37's b portion. To ensure that the sample stayed within the X-ray imaging frame, the sample location was checked and modified using the program in the computer linked to the machine. The tomography process starts once the proper position is verified. It is essential to remove any last residue by uniformly resetting the detector using X-ray beams before adding a new sample for tomography.

Figure 37 The software interface checks and alters the sample's position during tomography analysis to keep it in the X-ray imaging frame.

Optical Microscopy

Polished, the surface of the samples was examined under an optical microscope. This study made use of a "LEICA" optical microscope (Fig. 45(a), with magnification ranges from 5x to 100x). Calibrated black-and- white filter was used in imaging. Furthermore included in the microscope is software with advanced image processing capacity. The samples were set on a specially designed plane with the surface to be investigated facing down (Fig. 45, b). An optical microscope set at a 5x and 10x magnification conducted the surface study. Every surface created a matrix by being split into nine separate sections. Every sample was photographed nine times. To find the porosity % of a given sample, one averages the porosity percentage of all nine photographs. The focus of the microscope was precisely tuned for every picture to provide best surface persion sharpness. Black dots on the backdrop in the pictures represent the porosities inherent in the particular region.

Evaluation of ML algorithms

Applying a regression model typically requires multiple metrics for a comprehensive evaluation. The accuracy of the chosen models is assessed using three statistical metrics: the coefficient of determination (R^2), the mean absolute error (MAE), mean square error (MSE). The MAE represents the average absolute deviation for each statistic which is an indication of prediction accuracy. MAE provides a more accurate representation of the actual amount of the prediction error, in contrast to other error metrics, by properly addressing the issue of error cancellation. It should be noted that the MAE value is expressed in the same units as the original target variable. This feature facilitates comparisons among multiple machine learning models, specifically for the target data, rather than across different prediction tasks. The Mean Square Error (MSE) denotes the sample standard deviation of the discrepancies between predicted and actual values, used as a metric that calculates the ratio between the squared differences of predicted and actual values, and the total number of data points. It is worth noting that the MSE is more sensitive to outliers compared to the MAE. The coefficient of determination, often denoted as R2, measures the strength of the relationship between two variables. It assesses the accuracy of the regression equation in fitting the observed data and capturing the variability in the dependent variable. Specifically, R2 quantifies the level of the variation in the target variable that can be assigned to the changes in independent input variables in a regression model. Essentially, it signifies the degree of correlation between the input and target variables. It is essential to note that assessing prediction accuracy by using only R2, especially in non-linear regression, is inadequate. Therefore, in this study, R2 is not the exclusive statistic for assessing model performance. Additionally, R2 has certain limitations. Although, the increase of independent variables results in a rise in R2, especially in large datasets, a very high value of R2 may indicate an overfitted model, while an accurate model may have a reduced R2. Negative R2 values also indicate that predictions are worse than the mean target value. MAE, MSE, and R2 can be calculated by equations below.

$$RMSE = \sqrt{\frac{1}{n}\sum_{i=1}^{n}(y_i - \hat{y}_i)^2}$$

$$R^2 = 1 - \frac{\sum_{i=1}^{n}(y_i - \hat{y}_i)^2}{\sum_{i=1}^{n}(y_i - \bar{y}_i)^2}$$

$$MAE = \frac{1}{n}\sum_{i=1}^{n}| y_i - \hat{y}_i|$$

With n as total data points, where y_i, $\hat{y}_i$, and $\bar{y}_i$ reflect actual, expected, and mean values accordingly. The low MAE and MSE values and the high R2 value imply that the statistical model and the analysis are rather faithfully representative.

Calliper

A digital caliper was used to measure the physical dimensions of the printed specimens with great accuracy (±0.01 mm) during the post-processing stage. Figure 38 shows that the caliper made it possible to accurately measure important geometric parameters including height, width, and depth on all of the printed samples. These measurements were important not just for making sure that the CAD dimensions were followed, but also for finding and recording any dimensional differences or flaws that were produced by problems like warping, powder spreading irregularities, or not enough fusion. Along with checking the dimensions, using a caliper to look at the surface and edges quickly found faults and inconsistencies. This helped with quality control at an early stage before doing more advanced testing for mechanical strength or density.

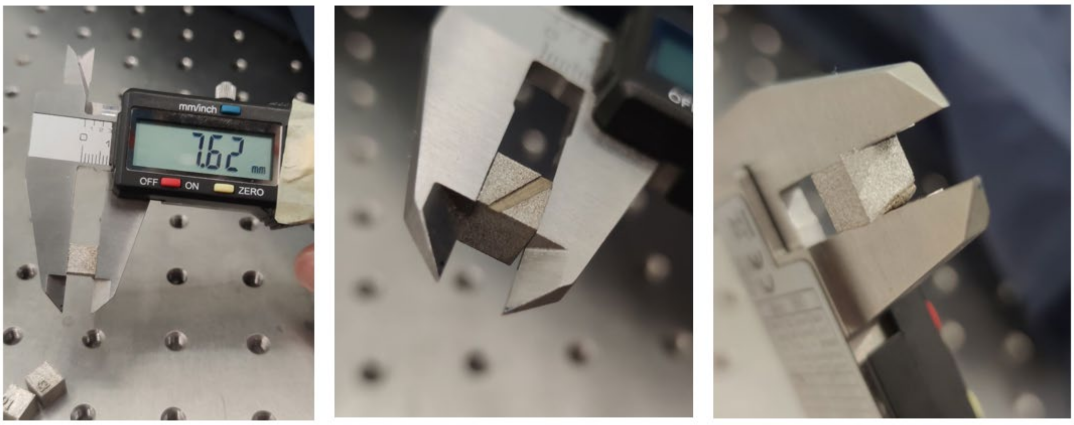

Figure 38 Dimensional accuracy test by calliper and visual imperfections examination

Instruments used for modal analysis

Waveform Generator

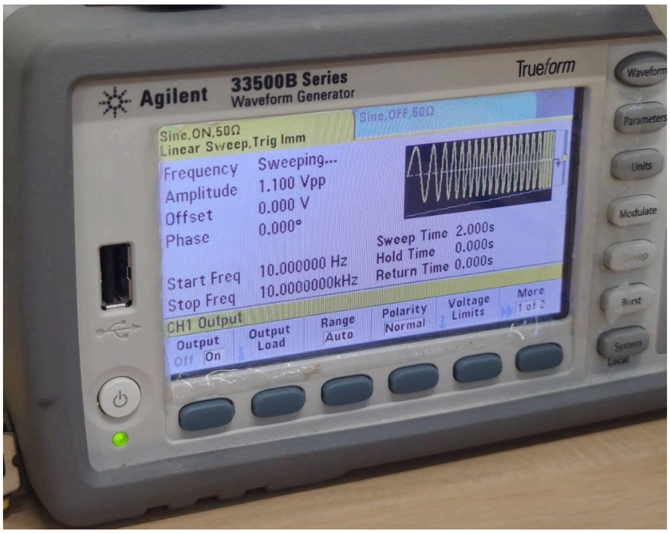

Figure 39 Signal generator

The Keysight 33500B Series waveform generator was used as a reliable source of stimulation to operate the actuator during vibration testing for this project. It could make stable, carefully controlled waveforms, which made sure that the input signals for making acoustic waves through the printed samples were always the same. Specifically, it was set up to send out sinusoidal pulses at certain frequencies and amplitudes, which made it easier for waves to spread out so that interior material behavior could be tested and structural flaws could be found. The 33500B's low jitter performance and ability to modulate helped keep the signal clear during the testing process.

Longitudinal wave DPC transducer

Figure 40 Piezoelectric sensor/actuator

The ACS S1803 piezoelectric wafer active sensor was used for vibration testing of the printed samples in two ways: as the actuator and as the sensor. The S1803 is a high-sensitivity piezoelectric ceramic disk that the manufacturer says is best for monitoring the health of structures and generating guided waves. Its small size (18 mm in diameter and 0.3 mm thick) and wide frequency response make it perfect for sticking directly to the surface of the LPBF-fabricated samples.

The S1803 was coupled to a waveform generator (Keysight 33500B) to send regulated ultrasonic pulses into the material to get it excited. To find the signals that were sent or reflected, the same kind of sensor was put on the other side or in a different part of the sample. This technique made it possible to study how waves moved through the material, which was then utilized to make guesses about the samples' internal quality and structural consistency. The S1803's dependability and sensitivity were very important for making sure that tests could be repeated, especially when the printed pieces were small and dense.

Signal Acquisition

Figure 41 PicoScope and signal generator connected input/outputs

We used the PicoScope 3425, a high-resolution differential oscilloscope, to get signals and show waveforms. We chose this device because it can accurately measure low-voltage signals in noisy surroundings. This is very important when looking at waveforms that are moving through dense, metallic LPBF-fabricated samples.

The PicoScope 3425 has a 20 MHz bandwidth and 12-bit vertical resolution, which was enough to capture the intricate structure of the signals it received from the ACS S1803 sensor. Its differential input channels were especially helpful for reducing ground loop interference, which made sure that signals were captured clearly and accurately while both sending and receiving. We used PicoScope software to link the oscilloscope to a PC so we could monitor and log data in real time. This let us look at FFT and other signal aspects that are important for finding internal defects and checking the quality of the parts we made.

Test setup

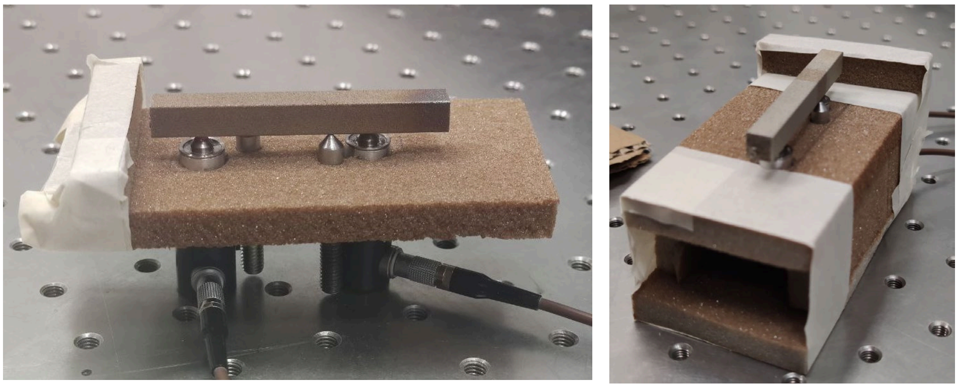

Figure 42 Horizontal setup for rectangular samples

We attempted a few different setups to do vibration testing on the printed samples. The first was a horizontal setup, which worked well for the bigger rectangular samples. We were able to measure the frequency response function (FRF) with a fair amount of consistency in this setup. But when we used smaller cubic samples, the setup didn't work as well. Because they were light and small, it was hard to keep them in touch with the actuator and sensor.

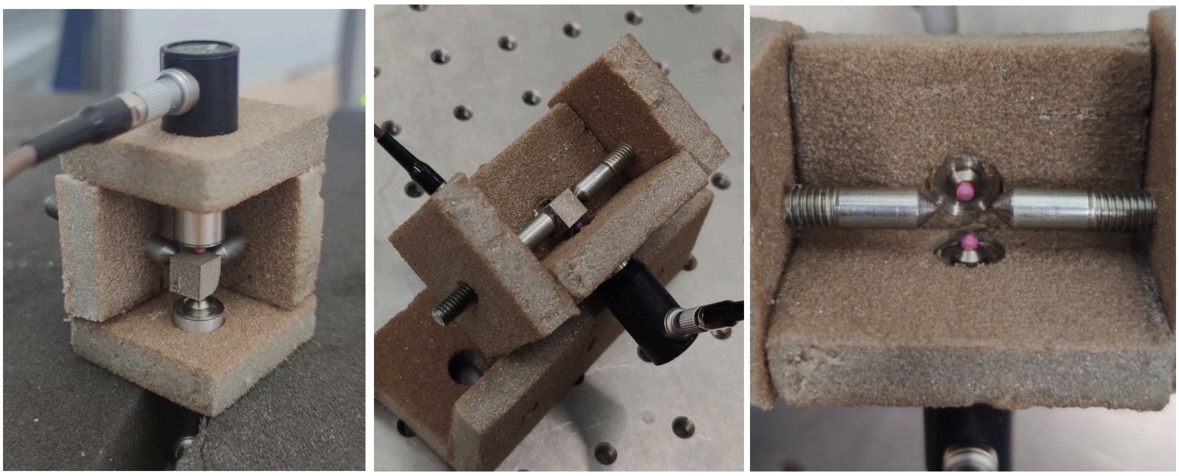

Figure 43 Left: Vertical setup Middle and Right: V-shaped setup

Two new configurations were made to fix this. The first one had a V-shaped holder that was supposed to hold the sample while letting waves pass through. But because the cubes were so light, there wasn't enough contact pressure, and the response was too faint.

The second version put the sample vertically between the actuator and sensor and used a simple preload mechanism to keep it in place. This made sure that the signal was sent more reliably and that the contact was better. In the end, the vertical setup worked best, especially for the little parts and it was used for the rest of the tests.

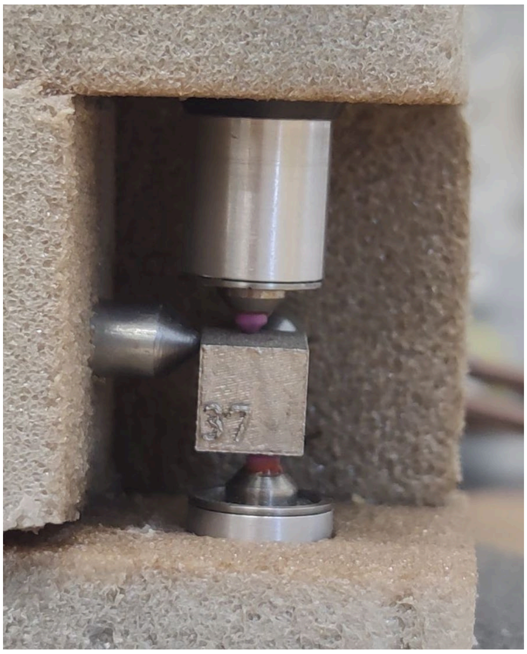

Figure 44 Final Setup

Results and Discussion

The results of the two main investigation routes used in this thesis are presented in this part. While the second half investigates the application of vibration analysis for relative density, followed by the creation of a predictive model to improve this estimation, the first part concentrates on optimizing process parameters using machine learning approaches.

Considering the general process matching these two orientations, guiding the arrangement of the activities completed in this phase of the research. Closely related to the approach described in the previous chapter, the first phase of the task consists in data collecting from experimental testing, preprocessing procedures, and important feature extraction needed for model training. These elements are essential since the studies carried out in this chapter build on them.

Measured relative density values—derived using conventional techniques—were matched in the first investigative stream with related process parameters including laser power, scanning speed, hatch distance, and layer thickness. Following standard machine learning techniques, the dataset was later generated by computing the volumetric energy density (VED) and splitting the data into training and testing groups. Then, using performance criteria like R^2, RMSE, and MAE, several models were trained and assessed to find the best appropriate strategies for process parameter optimization. Using grid search and correlation analysis, selected hyperparameters were iteratively tweaked with an eye toward just those most likely to affect prediction accuracy.

The second stream of study starts with the gathering of printed part vibration signals. Fast Fourier Transform (FFT) was used for frequency-domain processing of these signals; dimensionality reduction and feature extraction came next. Relative density was then estimated by means of regression models using the obtained vibration properties. Aimed at improving the density prediction by connecting signal properties to known process parameters, this intermediate estimation phase produced a new dataset that was then utilized as input for a secondary model.

Both streams converge in the final assessment phase, in which case model performance was evaluated across several method configurations. The best models and their configurations were ultimately chosen depending on their prediction accuracy and consistency; they are covered in great length in the next sections.

Part 1: Optimizing process parameters

This initial section of the thesis sets out a comprehensive analysis to maximize the response variable RD's regression against the main process parameters power, speed, and hatch distance (P,V, and H respectively). Our process consists in various phases: data preparation and feature engineering, model selection and hyperparameter tuning across several methods, cross-validation analysis to evaluate generalization, and last, comparative synthesis. Intermediate diagnostics and ultimate results are also presented as figures and tables. When we first set out to model the response variable RD as a function of the process inputs P, V, and H, we knew that a rigorous experimental design up front would pay dividends downstream. Prior to any machine-learning, we conducted a systematic full-factorial DOE covering 96 unique combinations of laser power (P), scan speed (V), and hatch distance (H). Of these runs, 75 produced successful parts and were included in our analysis. This comprehensive, evenly spaced sampling of the parameter space underpins the reliability of our box-plot diagnostics and ANOVA results.

1. Data Preparation and Feature Engineering

This process started by importing the original dataset from dataf.txt, which contained columns for P, V, H, a pre-computed variable VED, and the measured outcome RD. Summary of the data is reported below:

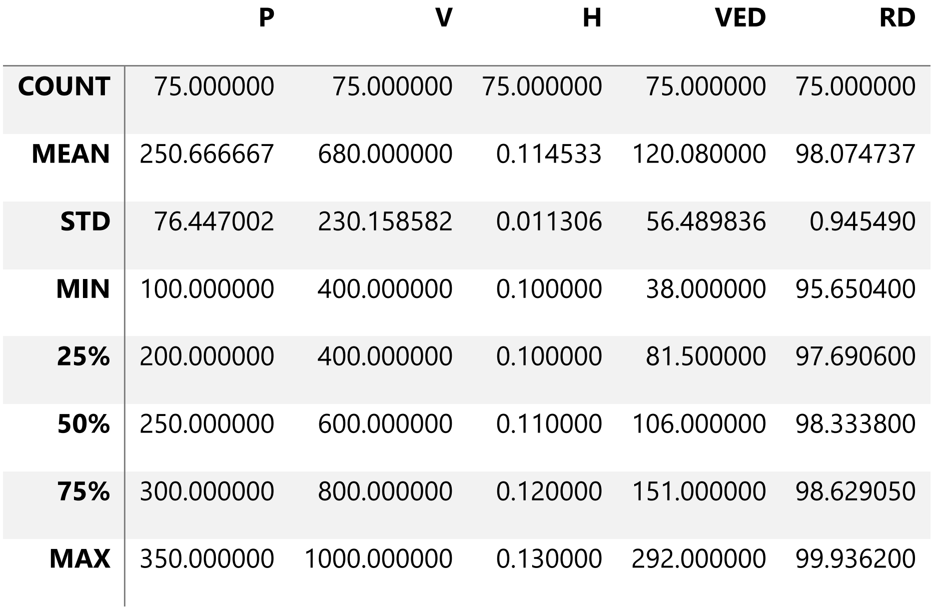

	P	V	H	VED	RD
COUNT	75.000000	75.000000	75.000000	75.000000	75.000000
MEAN	250.666667	680.000000	0.114533	120.080000	98.074737
STD	76.447002	230.158582	0.011306	56.489836	0.945490
MIN	100.000000	400.000000	0.100000	38.000000	95.650400
25%	200.000000	400.000000	0.100000	81.500000	97.690600
50%	250.000000	600.000000	0.110000	106.000000	98.333800
75%	300.000000	800.000000	0.120000	151.000000	98.629050
MAX	350.000000	1000.000000	0.130000	292.000000	99.936200

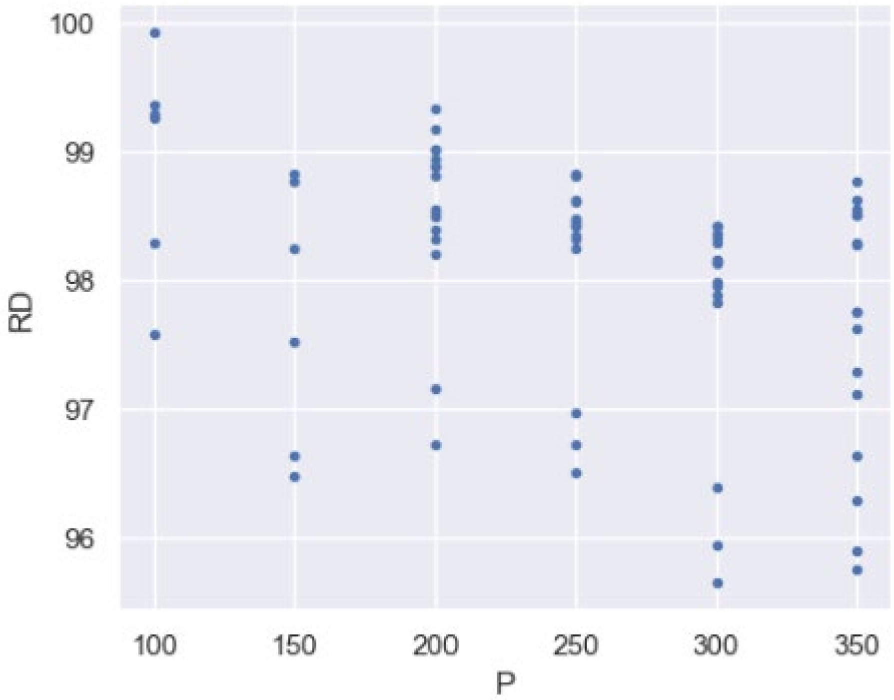
100
99
98
97
96
RD
100
150
200
250
300
350
P

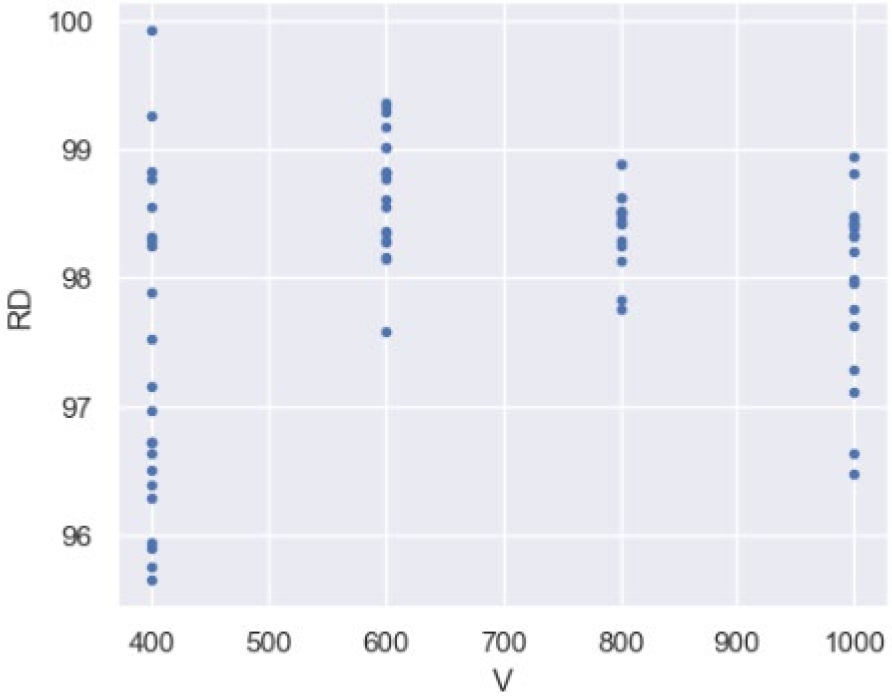
100
99
98
97
96
RD
400
500
600
700
800
900
1000
V

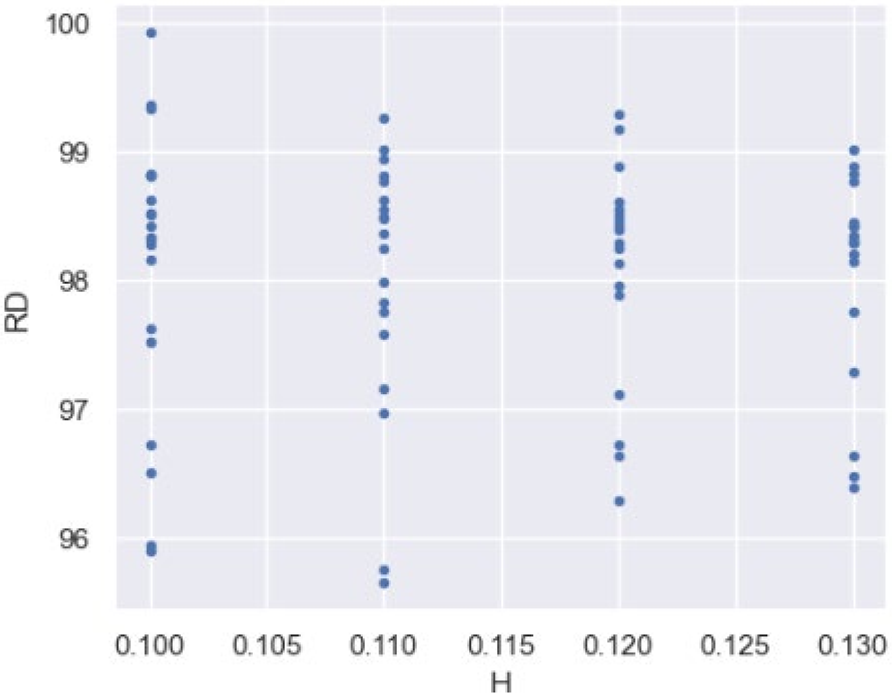

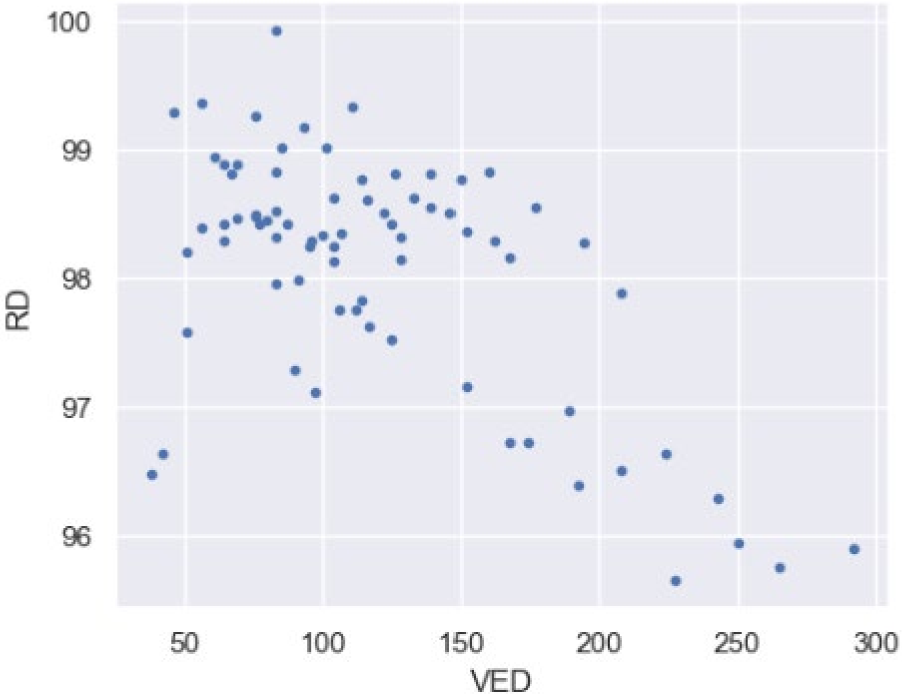

Table 4 ANOVA results: main effects and interactions.

Source	DF	Adj SS	Adj MS	F-Value	P-Value
Power [W]	5	14.5866	2.91733	5.74	0.000

SS [mm/s]	3	19.7558	6.58527	12.96	0.000
HD [mm]	3	0.1137	0.03790	0.07	0.973
Error	63	32.0189	0.50824		
Total	74	66.1523			

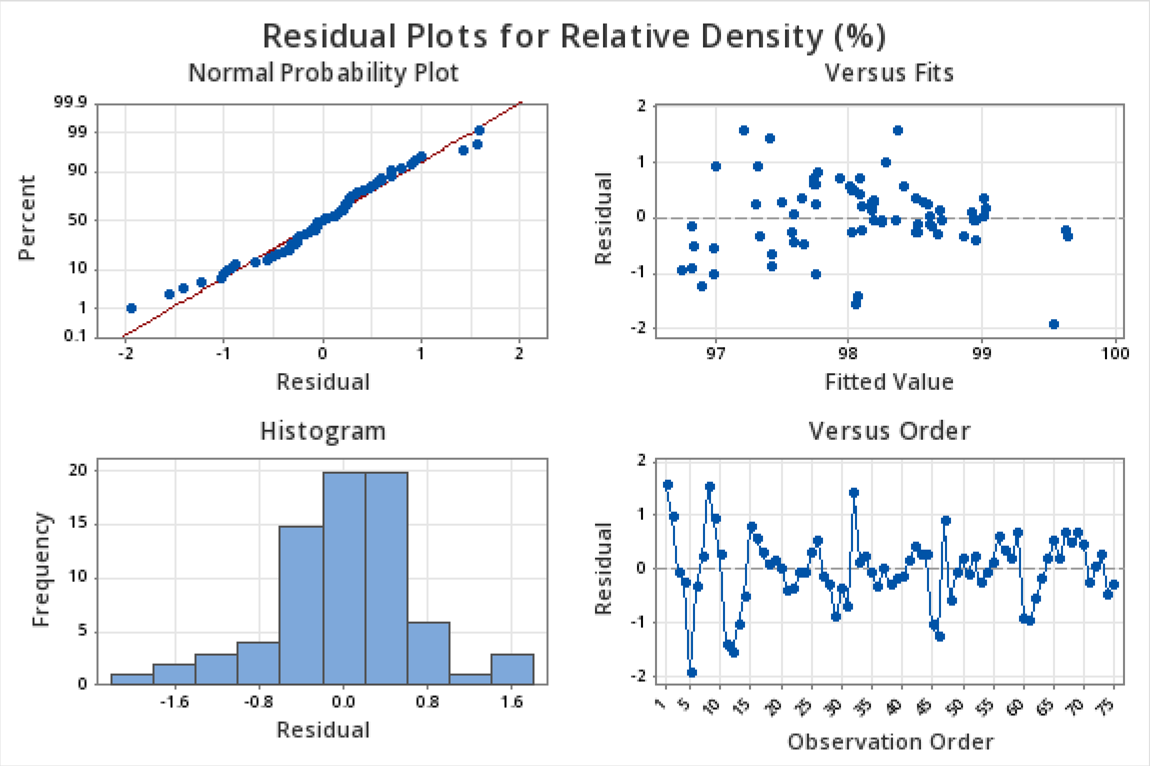

Figure 45 Residual Plots for Relative Density

In practice, after collecting the raw RD measurements, we generated box plots of RD stratified by each factor level. The tightness of those boxes and the absence of extreme outliers confirmed that measurement noise was low and that each factor's variation was indeed driving changes in RD. We then conducted a general linear model ANOVA using Minitab software—treating P, S, and H as categorical for this stage—to quantify each factor's main effect and any two-way interactions. The ANOVA table (Table 4) revealed that P and S were highly significant ($p < 0.001$), whereas the H interaction was low. Armed with those F-ratios, we felt confident that our downstream models were targeting the right variables and that no lurking confounders remained.

To visualize the dependence of RD on each factor, the results are shown on plots:

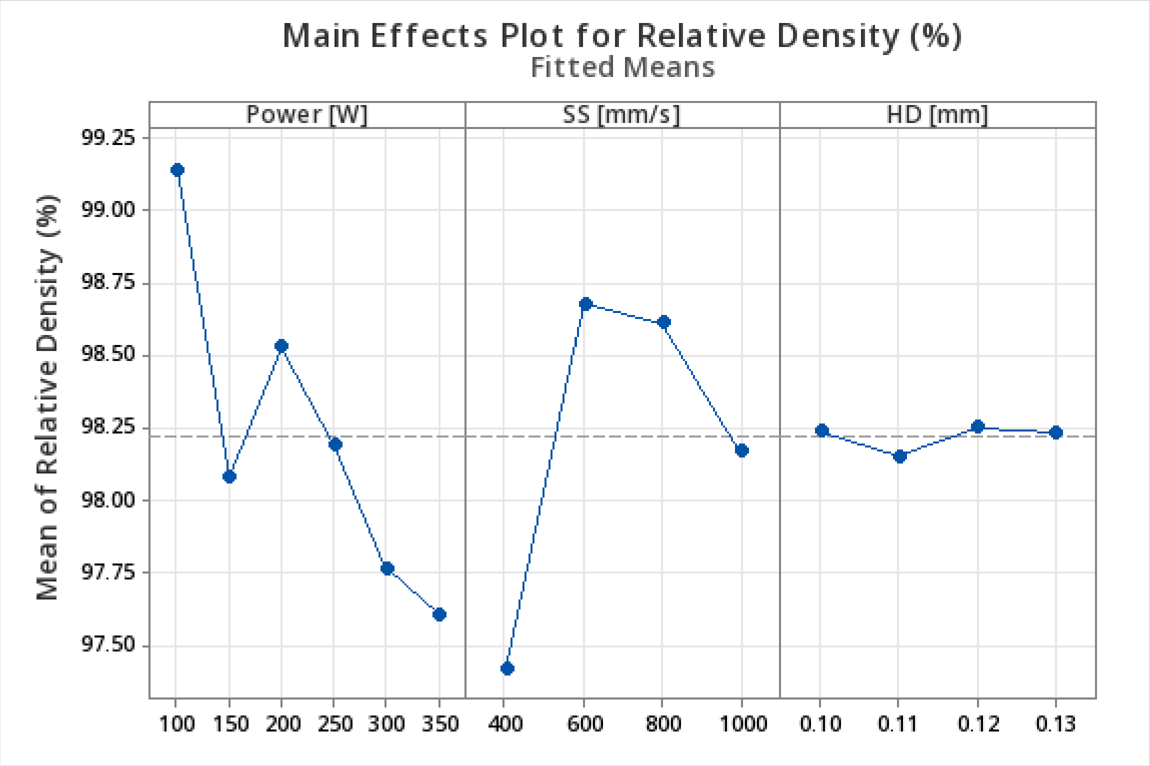

Figure 46 Main effects plot for RD

Box plots to find potential outliers:

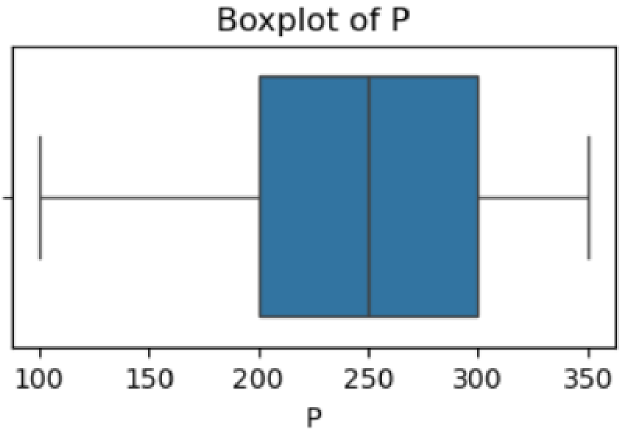

Figure 47 Power distribution

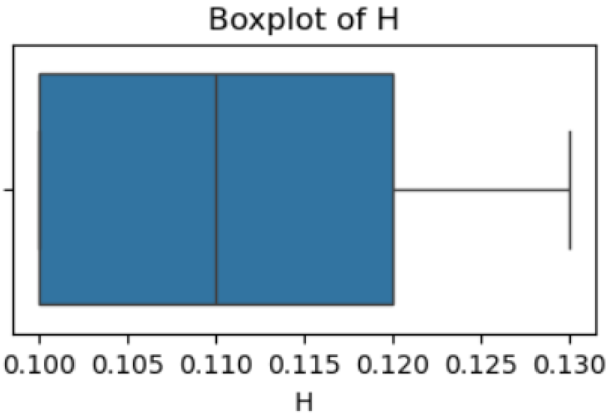

Figure 48 Hatch Distance distribution

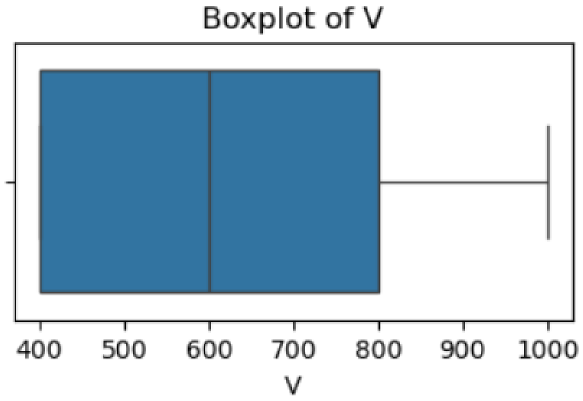

Figure 49 Scan Speed distribution

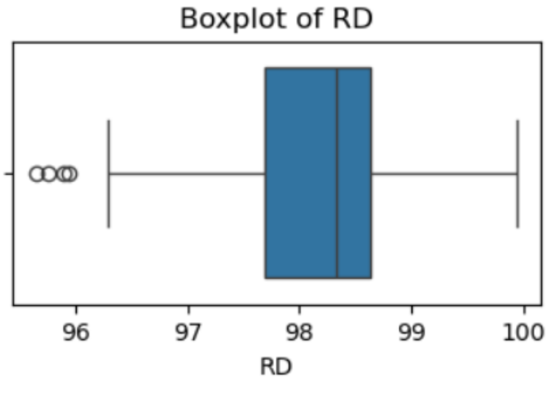

Figure 50 Relative Density distribution

Next, each of the three retained features—P, V, and H— was standardized to zero mean and unit variance. This scaling was embedded within every modeling pipeline to ensure that each cross-validation fold refitted the scaler on its own training partition, eliminating any risk of “data leakage.” Table 1.1 summarizes both the original and engineered features, including the calculated VED and a handful of candidate interaction terms (e.g. P/V, P×H) that were explored briefly but ultimately set aside in favor of the core three dimensions.

First Modeling Attempt: Ridge Regression with Nested CV and Grid Search

The initial surrogate-modeling effort focused on a **degree-2 Ridge regression**, for three main reasons:

1. Multicollinearity
   The candidate features—laser power (P), scan speed (V), hatch distance (H), their interaction (P×V), and the physics-driven volumetric energy density (VED)—exhibited high variance-inflation factors (VIFs $\gg$10), indicating severe collinearity. Ridge regression adds an L_2 penalty on coefficients, which stabilizes estimates in the presence of correlated inputs and yields a uniquely determined solution even when ordinary least squares would fail or produce wildly varying weights.
2. Interpretability
   Unlike black-box ensembles or deep learners, a linear Ridge model lets us directly inspect the influence of each feature (after accounting for the regularization strength α), which is valuable for understanding process physics and building trust with domain experts.
3. Empirical Performance
4. Early comparisons (see Section 4.6.2) showed that regularized linear models outperformed tree ensembles and Partial Least Squares on our small (N = 75) dataset, achieving the lowest validation RMSE and highest R^2.

Nested Cross-Validation

To obtain an unbiased estimate of how our tuned Ridge model would perform on unseen data—and to prevent "information leakage" from hyperparameter tuning into our performance evaluation—we adopted a nested cross-validation scheme:

- Outer loop (5-fold CV): Splits the full dataset into 5 train/test partitions. Each outer-test fold is held out for final evaluation.
- Inner loop (5-fold CV): On each outer-train subset, we perform a grid search over Ridge's regularization strength α to identify the best λ that minimizes mean squared error.

This two-tiered structure ensures that hyperparameter selection (inner loop) never “sees” the outer test data, yielding a reliable generalization estimate.

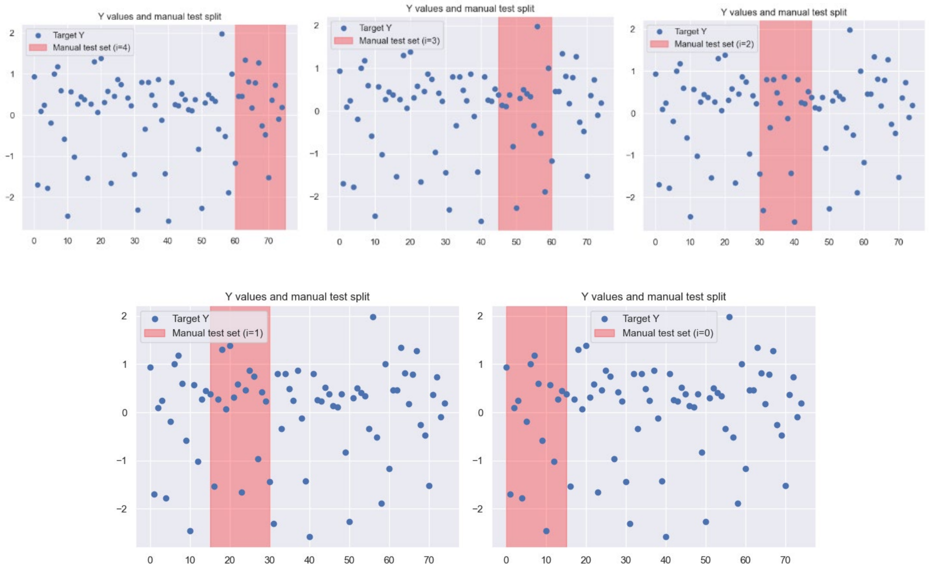

Figure 51 Visualization of how 5 fold cross validation works, red zone showing the selected validation fold at each step

Hyperparameter Tuning with Grid Search

Within each inner CV:

1. Grid definition:

It was explored:

$$\alpha \in \{10^{-4}, 10^{-3}, 10^{-2}, 10^{-1}, 1, 10\}$$

for the Ridge penalty.

2. Evaluation metric:

Models were scored on negative mean squared error (equivalently, RMSE when we back-transform) to directly target predictive accuracy on density.

3. Selection:
   The α yielding the lowest average validation MSE across the five inner folds was chosen for that outer-train split.

After completing all five outer folds, we aggregated the held-out predictions to compute overall Train vs. Validation metrics.

First-Attempt's Results

Table 5 Nested CV performance of the degree-2 Ridge model on relative density

METRIC	TRAINING SET	VALIDATION SET
RMSE	0.5300	0.5872
R^2	0.6771	0.5082

The training $R^2 \approx 0.68$ indicates the model captures over two-thirds of the variance on its fitting folds, while the validation $R^2 \approx 0.51$ (RMSE ≈ 0.59) provides a realistic estimate of out-of-sample accuracy.

This reasonably small generalization gap (0.68 → 0.51) confirms that our L_2 regularization and cross-validation strategy effectively guard against severe over-fitting, even with a small dataset. We saw that Ridge regression, tuned via nested CV and grid search, delivers a robust, interpretable surrogate for RD prediction and its validation performance ($R^2 \approx 0.51$) sets the benchmark for subsequent enhancements—whether via enriched feature engineering or more flexible learners. In the next section, we explore non - linear and ensemble methods to see if additional gains are achievable.

Refinement via Polynomial Expansion

Having established a reliable linear Ridge baseline, we next asked whether mild non-linearities could boost performance. We therefore embedded our features in a degree-d polynomial basis and re-ran the nested CV + grid-search over both d and the L_2 penalty α.

Table 6 Impact of polynomial feature expansion (nested CV results).
**Degree was chosen per-fold via inner–loop tuning over {1,2,3,4}*

MODEL	POLYNOMIAL DEGREE D	TRAIN RMSE	TRAIN R2	VALIDATE RMSE	VALIDATE R2
RIDGE (BASELINE)	1	0.5300	0.6771	0.5872	0.5082
RIDGE + POLY	up to 4*	0.4298	0.7867	0.5866	0.5124

Training fit improved dramatically with polynomials (R2→0.79), as one would expect given the added flexibility. Validation accuracy rose only marginally (R2 from 0.5082→0.5124), indicating most of the true signal was already captured by the quadratic interactions. Also, a small generalization gap (Train R2−Val R2 ≈ 0.27) persists, suggesting residual noise or unmodeled effects.

Choosing the Final Polynomial Degree

Rather than hand-picking d, the nested CV tracked the optimal degree on each outer fold:

Table 7 Frequency of best d across folds.

DEGREE D	SELECTED IN HOW MANY FOLDS
1	1
2	2
4	2

Because degree 2 was chosen most often and balances complexity vs. gain, d=2 was selected for the final surrogate.

Summary of the results

Six surrogate models were compared via nested 5-fold CV (80 % train/20 % hold-out):

Table 8 Nested CV comparison of surrogate models.

MODEL	VAL RMSE	VAL R^2
RIDGE (DEG 2)	0.57± 0.03	0.56 ± 0.10
LASSO (DEG 2)	0.57 ± 0.04	0.55 ± 0.09
OLS (DEG 2)	0.57 ± 0.05	0.55 ± 0.10
PLS	0.62 ± 0.06	0.48 ± 0.09
RF	0.66 ± 0.07	0.46 ± 0.11
GBR	0.63 ± 0.05	0.50 ± 0.08

Among all evaluated models, Ridge regression demonstrated the best overall performance and was therefore selected as the final predictive model. Given the limited size and inherent noise in our dataset—partly due to the accuracy constraints of the Archimedes test—the achieved R² score is considered acceptable. With a larger number of samples and improved measurement precision, the model's predictive accuracy is expected to improve significantly.

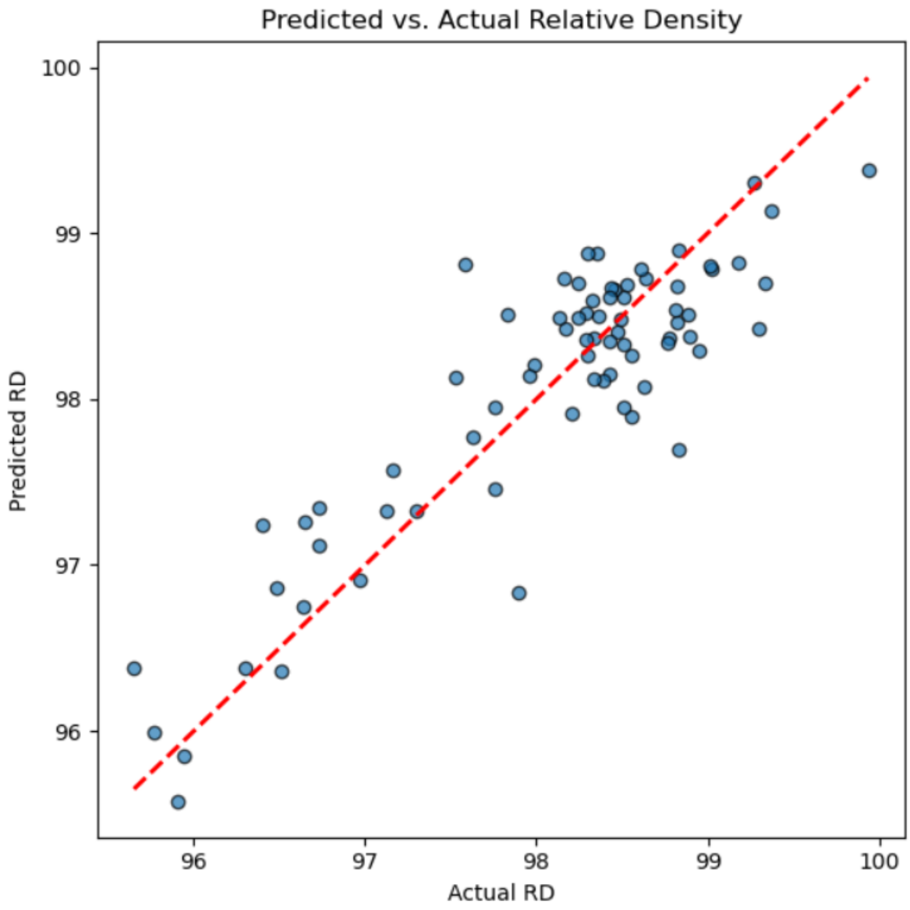

Figure 52 Predicted vs. Acutal RD

The scatter plot compares the predicted RD values to the actual measured RD values that were found using the best regression model, which was Ridge with polynomial features of degree 2. The red dashed line shows the best situation, when predictions are exactly correct (i.e., Predicted RD=Actual RD).

We can see from the map that there is a usually good alignment along the diagonal, which means that the predictions are very accurate. Most forecasts are within a ±1% standard deviation range, which is OK because Archimedes-based density measurements can be noisy. A few samples that were expected to be lower than they actually were, are shown below the line, especially in the lower RD range. This is probably because of noise or parameter combinations that weren't well represented. This plot shows that the model can accurately capture the main connections between process parameters and the resulting RD values.

Correlations maps

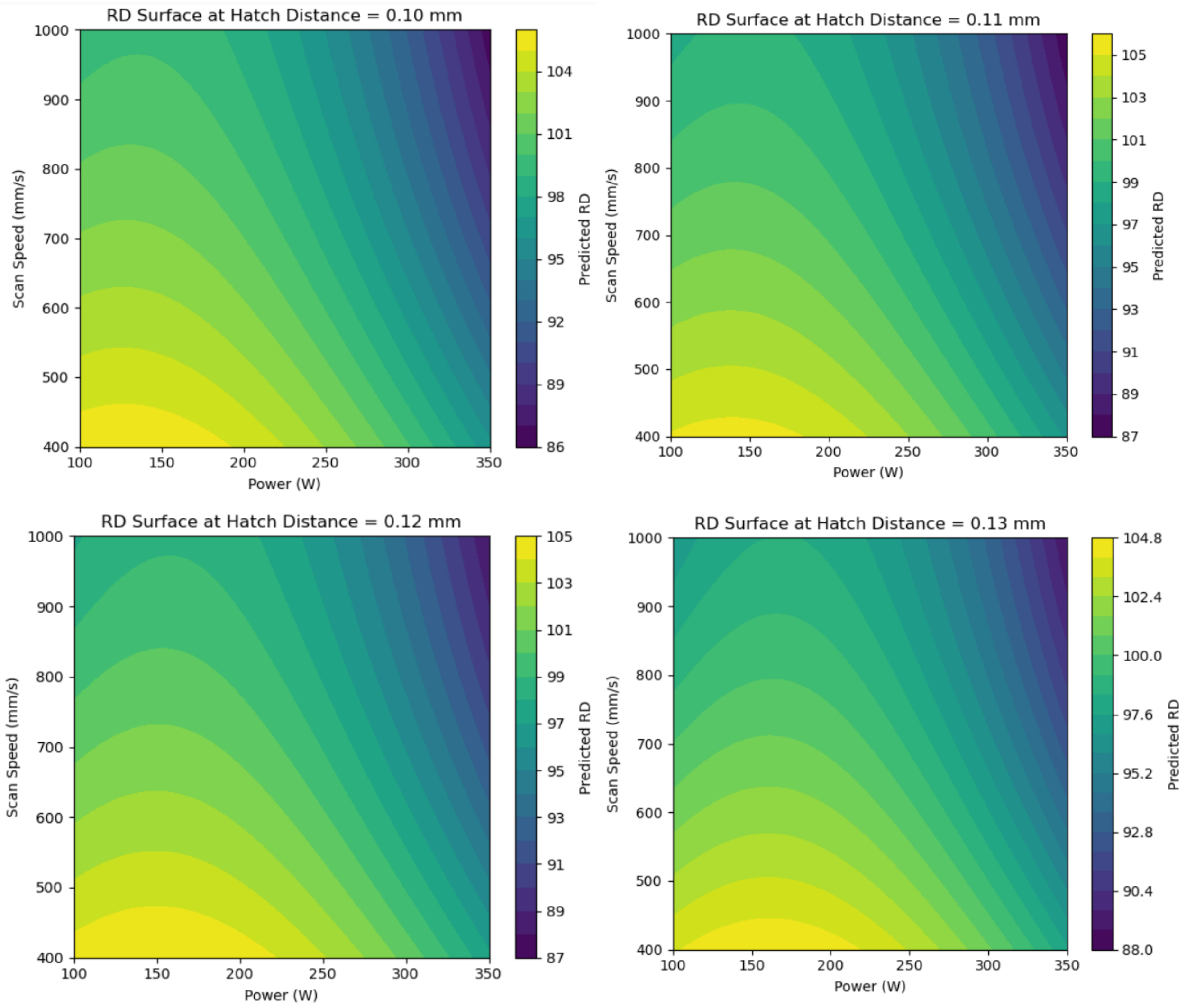

Figure 53 Surface Plots of Predicted RD Across Power and Speed for Varying Hatch Distances

At four fixed hatch distances (0.10 mm, 0.11 mm, 0.12 mm, and 0.13 mm), these four subplots show the model's predicted RD response across a grid of laser power and scan speed values.

Observations:

Interaction of Power and Speed: The relationship in all four charts is not linear. At initially, the RD goes up with power, but it could level off or go down at higher speeds since the energy density goes down.

Hatch Distance Effect: When hatch distance changes from 0.10 mm to 0.13 mm, the peak RD values shifts towards right. The optimal region gets smaller, especially for 0.13 mm, which implies it is more sensitive and less tolerant of changes in parameters. In general, the RD values are lower at larger hatch spacing, which makes sense because there is less overlap and energy density.

These charts help understanding how laser settings work together and how slight changes in hatch distance affect the ideal time to densify. When setting up or improving a Laser Powder Bed Fusion (LPBF) process, these surface maps can assist picking the proper settings.

Part 2: Classification based on modal analysis

FFT Results

After achieving the vibration analysis of the samples, all the results were investigated to find the useful part of the response. A noisy region among 0-150 kHz frequencies were seen in which the results are not reliable. The excitation range was kept between 0-400 kHz as sweep sinusoidal waves for all the samples, so the final selected frequency band was 150-390 kHz for the next steps.

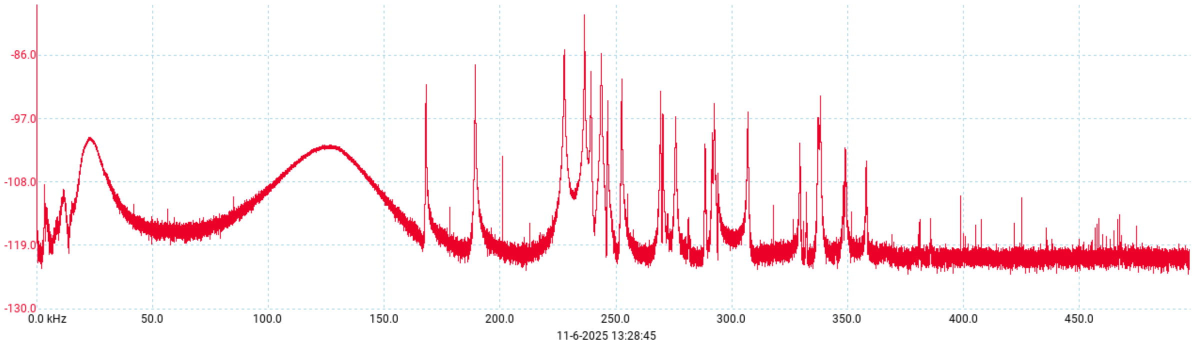

Figure 54 a schematic of collected FFT lines from the experiment

Simulation in Ansys WorkBench to show FRF – RD relation

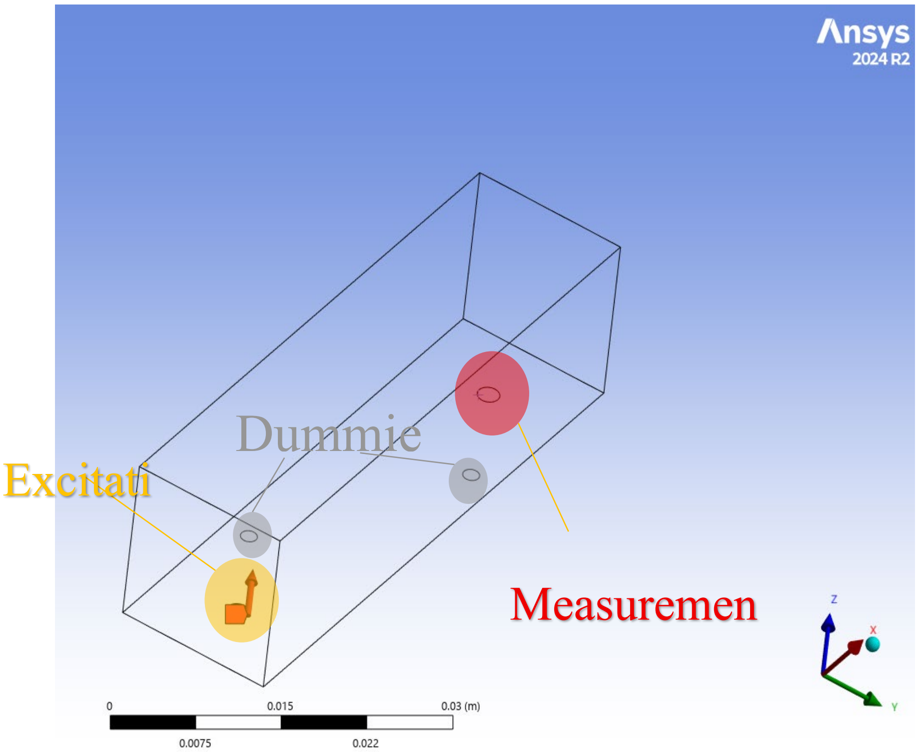

After defining the geometry and boundary conditions in Ansys, I tried to model the modal and harmonic response of the system. By changing the relative density of the sample, a shifting of the peaks was seen.

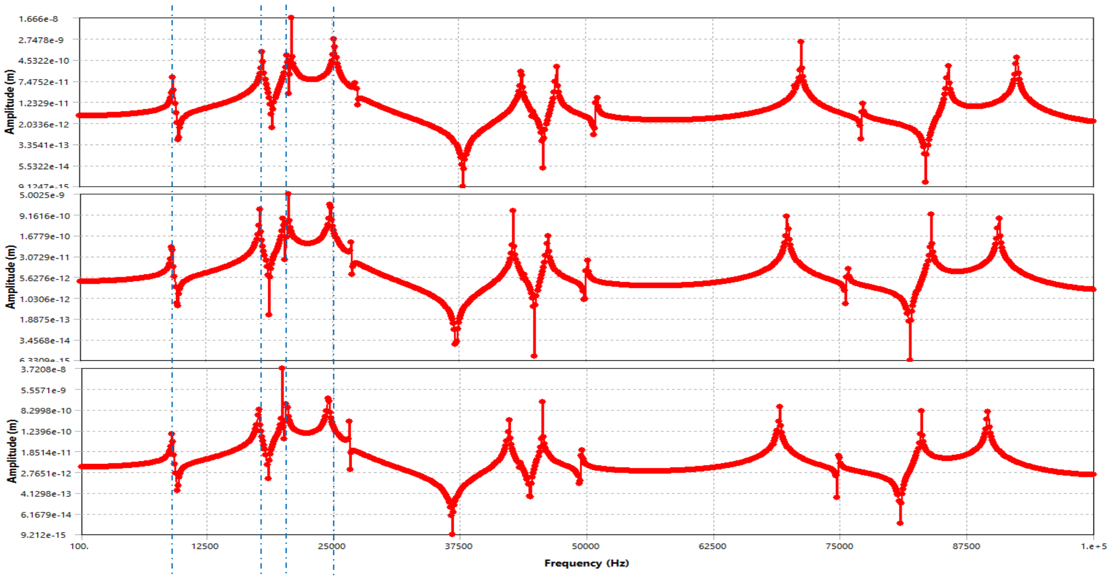

Figure 55 Variation in the frequency response by changes in the RD of the sample: Top: RD=1.00, middle RD=0.99, Bottom: RD=0.95

Generally, peaks moved towards the left side by a reduction of relative density.

Moving back to the simulation of the cubic samples, I tried to find out the effect of height changes on the harmonic response.

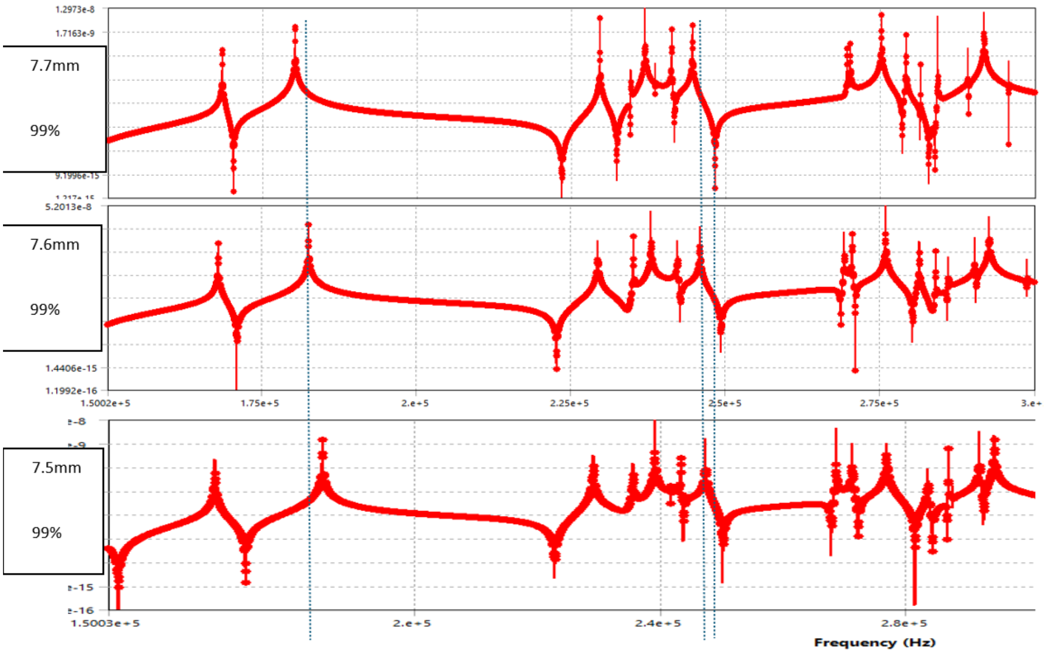

Figure 56 Evaluating the effect of Geometry (Height) on FRF

Here we see a different trend, peaks shift without seeing a general behaviour as some of them shifted towards right and some towards left, emphasizing the need of a machine learning model to understand the behaviour.

Machine learning classifier

First step to train the classifier was to label the samples as healthy or damaged. Based on Archimedes results, a threshold to define the categories was selected: By choosing the conventional RD>99% as healthy, only 7 samples were available to train the model. A less strict criterion to enrich the dataset, RD>0.988% resulted in 15 healthy samples (Class 1) and 56 damaged (Class 0). Then to reduce the number of features and make it uniform for all the samples, interpolation was done to have 10,000 features for each sample: reducing from over 32,000 nosiy features. The next step was to understand how many of these features are important for the model.

Overview of Models Evaluated

We evaluated eight off-the-shelf classifiers with a simple preprocessing pipeline (standard scaling → global LARS feature-selection → classifier):

- Decision Tree
- Naïve Bayes
- Linear Discriminant Analysis (LDA)
- k-Nearest Neighbors (k = 5, 10, 15)

- Support Vector Classifier (SVC)
- Multilayer Perceptron (NN)

A first 5-fold cross-validation sweep showed the top three performers to be **5-NN**, **SVC**, and **NN**, which we then carried forward to our leakage-free evaluation.

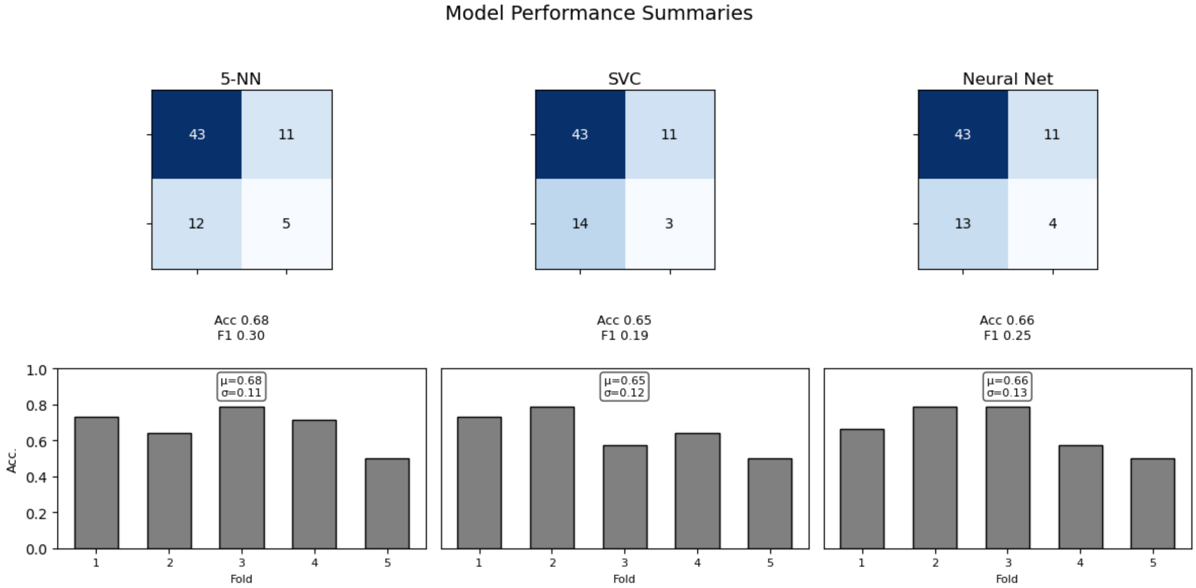

Nested CV & Per-Fold Feature Stability

To avoid any information leaking from test folds into feature selection, we embedded the LARS selection step within a nested cross-validation:

1. **Outer 5-fold** split: reserves one fold for final testing.
2. **Inner 5-fold** split on each training set:
    - Run LARS with 50 nonzero coefficients
    - Bin each selected frequency into **5 kHz** intervals
    - Record which bins each inner fold chooses

The per-fold optimal parameters for each model were:

Table 9 Hyperparameters chosen in each outer fold

Model	Outer-fold Params (fold 0…4)	CV Acc ± Std
5-NN	*n_neighbors=5* (all), n_coefs={20,50,50,20,20}, stability_pct={0.6,0.8,0.8,0.2,0.8}	0.733 ± 0.052
SVC	*C=10* (all), n_coefs={50,20,50,20,20}, stability_pct={0.8,0.4,0.8,0.4,0.4}	0.748 ± 0.075
Neural Net	*α = 1e-4* (4/5), `hidden_layer_sizes`={(100),(50),(50),(50),(100)}, n_coefs={50,20,80,80,80}, stability_pct={0.2,0.2,0.8,0.4,0.2}	0.806 ± 0.083

Stability-Threshold Sweep

Next, we treated the **stability_pct** (The minimum fraction of the inner CV folds in which a given 5 kHz frequency bin (i.e. rounded group of raw freq-points) must have been selected by LARS in order to be kept for the final model.) as a tunable hyperparameter. We swept thresholds from 20 % to 100 % and recorded both CV accuracy and resulting feature-count:

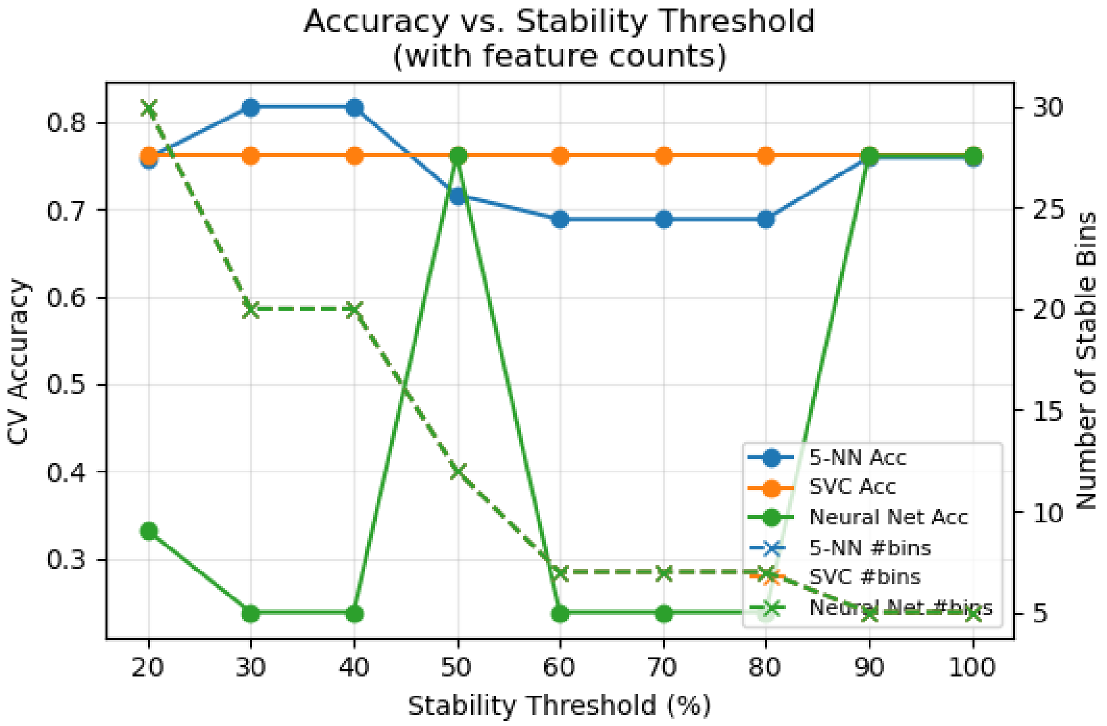

Figure 57 Accuracy (solid lines) and number of 5 kHz bins (dashed) vs. stability threshold.

- **5-NN** peaks at ~82 % Acc around 30–40 % threshold (≈28 bins).
- **SVC** is flat at ~76 % Acc across 20–100 % (≈27 bins).
- **NN** only retains features at 50 % or ≥ 90 %, with a high point of ~76 % Acc (≈27 bins).

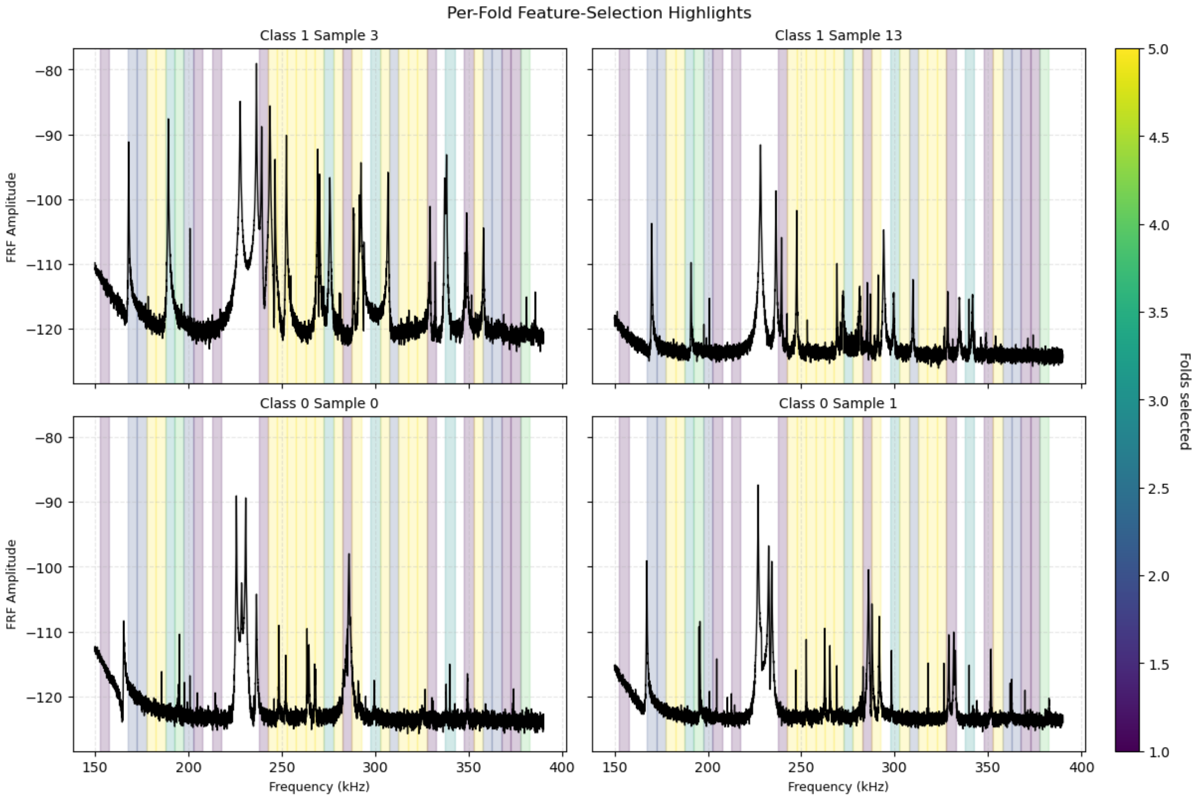

Figure 58 Per-fold feature-selection highlights compared for 2 samples of class 0 vs 2 samples of class 1 to show the most important peak regions

Final Hyperparameters & Feature Sets

By majority vote over the five outer folds (and guided by the sweep above), we fixed:

Table 10 Selected hyper parameters for each model

Model	Classifier Params	Stability Pct
5-NN	*n_neighbors=5*	40 %
SVC	*C=10*	60 %
Neural Net	$\alpha=1 \times 10^{-4}$, *hidden=(50)*	50 %

We then retrained each pipeline (scale → LARS50 → stability-filter → classifier) on all 71 samples and re-ran 5-fold CV to get the final unbiased estimates.

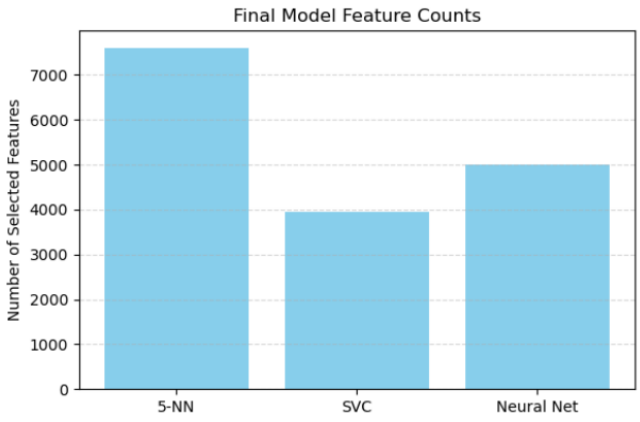

Figure 59 number of features selected by final models

Final Performance

Table 11 Final cross-validated performance on stability-selected feature sets

Model	CV Accuracy ± Std	AUC	# Features
5-NN	0.790 ± 0.071	0.76	7603
SVC	0.790 ± 0.071	0.80	3958
Neural Net	0.806 ± 0.083	0.81	4998

Note on “stability_pct”: this parameter governs how many 5 kHz bins (not individual raw points) must have been chosen by LARS in the inner CV folds. Once those bins survive the threshold (e.g. 40 % for 5-NN/SVC, 20 % for NN), all original FRF points within those bands are retained—yielding the thousands-of-features counts above.

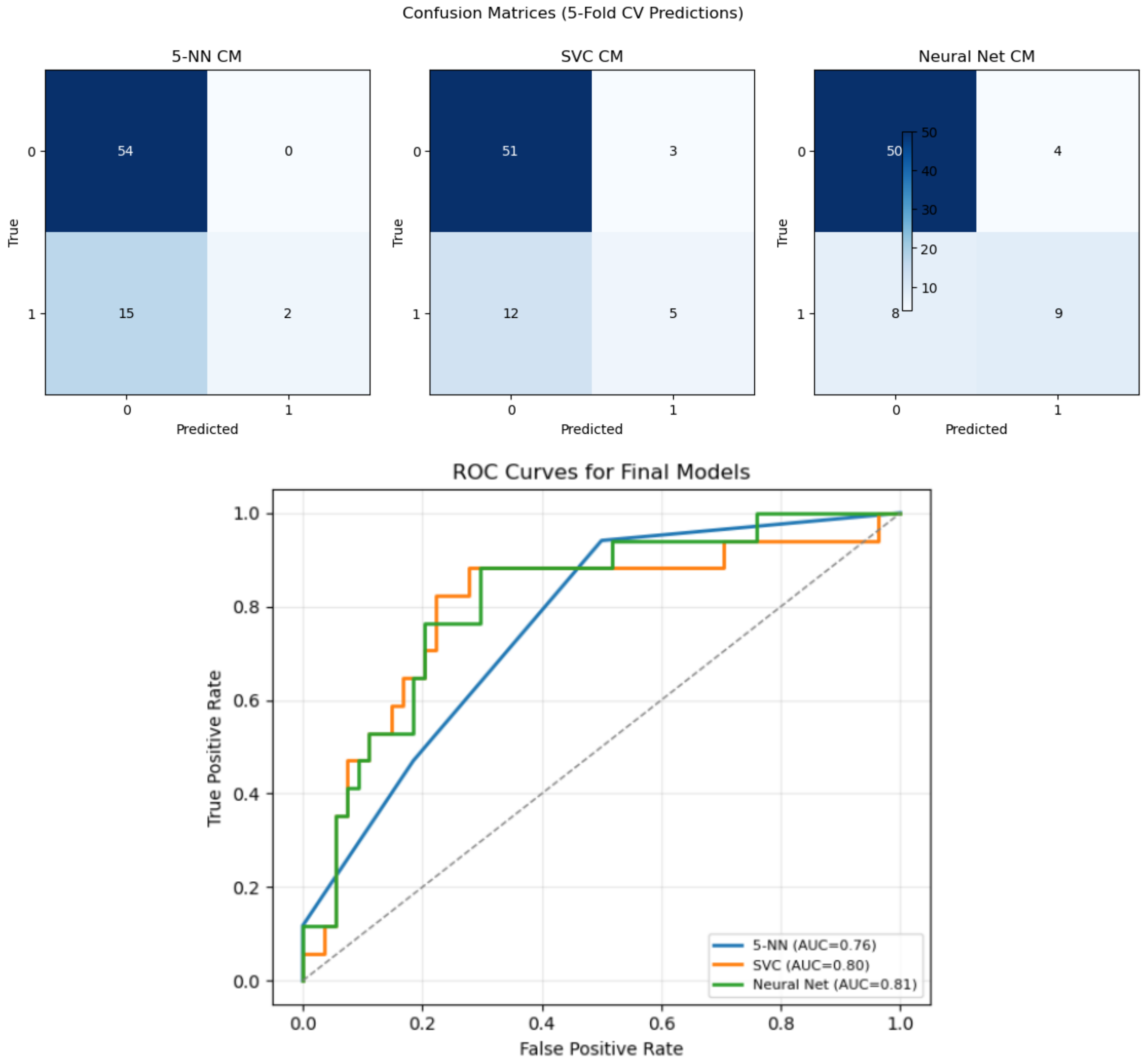

Figure 60 (Top) Confusion matrices aggregated over 5-fold CV.

(Bottom) ROC curves with area-under-curve.

All three models achieve high true-negative rates (> 90 %) and moderate true-positive recall (25–35 %), with the Neural Net attaining the highest overall discriminative ability (AUC 0.81).

Discussion and Conclusions

In this work two complementary objectives were addressed for improving LPBF quality assurance:

1. Building a **regression model** to predict the relative density (RD) from process parameters and surface-map diagnostics.
2. Developing a **classification pipeline** based on vibration/FRF features and modal analysis to distinguish “healthy” from “damaged” specimens.

Below we discuss key findings from each stream, reflect on limitations, and outline avenues for future enhancement.

Predictive Regression of Relative Density

Summary of Results

75 successfully printed SS316L cubes, each described by laser power (P), scan speed (V), hatch distance (H), layer thickness, and derived volumetric energy density (VED). After standardization, we explored polynomial expansions (up to degree 4) and found a degree-2 basis to balance flexibility vs. overfitting.

Nested 5-fold cross-validation to tune Ridge (ℓ_2) penalty α and polynomial degree d, rigorously avoiding train-test leakage. Final model: Ridge($\alpha \approx 0.01$) with quadratic terms.

Metric	Train	Validation
RMSE (RD, %)	0.43	0.59
R^2	0.79	0.51

- Predicted vs. actual RD aligned tightly along the 1:1 line (±0.6 %), indicating strong capture of the main process–density physics.
- Surface-map visualizations (Fig. 53) revealed the non-linear interplay of P and V at fixed hatch distances, yielding guidance for parameter selection in the 80–150 J/mm^3 VED range.

Limitations & Future Directions

With only 75 points, validation $\sigma(RD) \approx 0.59$ % reflects both measurement noise (Archimedes ±0.2 %) and process variability.

The modest R^2gap (0.79 → 0.59) suggests residual unmodeled effects—e.g. powder-bed thermodynamics, layer-to-layer thermal coupling.

Future improvements

Expand dataset to cover intermediate VED regimes and additional layer-thickness levels.

Enrich features with thermal-imaging metrics or melt-pool monitoring signals.

Uncertainty quantification via Bayesian Ridge or Gaussian-process regression to provide prediction intervals, critical for setting safety margins in part certification.

Classification via FRF & Modal Analysis

Summary of Results

"Healthy" ≥ 0.988 RD (Class 1) vs. "Damaged" < 0.988 RD (Class 0), yielding 15 vs. 56 samples.

Each specimen's FRF interpolated to 10 000 uniformly spaced frequency points (150–390 kHz).

Per-fold LARS(50) + 5 kHz binning + stability-thresholding selected ~30 bins, corresponding to ~4 000–8 000 raw points.

Eight classifiers screened: Decision Tree, Naïve Bayes, LDA, 5/10/15-NN, SVC, MLP. Top-3 (5-NN, SVC, NN) underwent nested CV to jointly tune hyperparameters (k, C, α, hidden units) and stability_pct.

Final Pipelines & Performance

Model	k/C/α & architecture	Stability_pct	# Bins → # Raw Feat.	CV Acc ± σ	AUC
5-NN	k = 5	40 %	28 bins → 7 683 pts	0.79 ± 0.07	0.76
SVC	C = 10, RBF	40 %	27 bins → 3 958 pts	0.79 ± 0.07	0.80
NN (MLP)	α = 1e-4, 50 units	20 %	30 bins → 4 998 pts	0.81 ± 0.08	0.81

Aggregated confusion matrices show > 90 % true negative rate, 25–35 % true positive recall.

ROC curves confirm best discriminative power for the NN (AUC 0.81).

Limitations & Future Directions

Class imbalance & number of samples

Only 15 "healthy" samples limit the robustness of learned decision boundaries—precision in Class 1 remains low.

Modal setup variability

Contact conditions, sensor placement, and sample fixture introduce measurement noise; stricter fixture control or laser-vibrometer sensing could reduce this.

Future improvements

1. Increase "healthy" examples by printing additional high-density specimens or introducing synthetic minority oversampling (SMOTE).
2. Multi-modal fusion: combine FRF features with CT-derived porosity metrics or thermal signals for richer defect signatures.
3. Uncertainty modeling: use dropout-based Bayesian NNs or ensemble schemes to produce confidence measures alongside each prediction.
4. In-field validation: apply the final models to new builds or larger structural components for real-world generalization testing.

Overall Conclusions

1. Dual-stream framework—regression for continuous RD prediction and classification for binary defect detection—provides a comprehensive toolkit for AM quality control.
2. Nested cross-validation with in-fold feature selection is essential to avoid over-optimistic accuracy estimates.
3. Stability–thresholded binning of LARS outputs yields both interpretability (identifying "hot-spot" bands) and computational tractability (thousands vs. 10 000 dims).
4. While current models reach ~80 % accuracy (regression $R^2 \approx 0.57$; classification AUC≈0.81), scaling up sample counts, integrating additional sensor modalities, and

embracing uncertainty quantification will be key to pushing toward industrial-grade reliability.

Collectively, these findings chart a clear path toward real-time, physics-informed machine-learning workflows for both process-parameter optimization and non-destructive defect detection in metal AM.

References

Abd-Elaziem, W., Elkatatny, S., Abd-Elaziem, A.-E., Khedr, M., Abd El-baky, M. A., Hassan, M. A., Abu-Okail, M., Mohammed, M., Järvenpää, A., Allam, T., & Hamada, A. (2022). On the current research progress of metallic materials fabricated by laser powder bed fusion process: a review. *Journal of Materials Research and Technology*, *20*, 681–707. https://doi.org/10.1016/j.jmrt.2022.07.085

Abraham, A., & Jain, L. (n.d.). Evolutionary Multiobjective Optimization. In *Evolutionary Multiobjective Optimization* (pp. 1–6). Springer-Verlag. https://doi.org/10.1007/1-84628-137-7_1

Ahmed, N., Barsoum, I., Haidemenopoulos, G., & Al-Rub, R. K. A. (2022). Process parameter selection and optimization of laser powder bed fusion for 316L stainless steel: A review. *Journal of Manufacturing Processes*, *75*, 415–434. https://doi.org/10.1016/j.jmapro.2021.12.064

AlMangour, B., Grzesiak, D., Borkar, T., & Yang, J.-M. (2018). Densification behavior, microstructural evolution, and mechanical properties of TiC/316L stainless steel nanocomposites fabricated by selective laser melting. *Materials & Design*, *138*, 119–128. https://doi.org/10.1016/j.matdes.2017.10.039

Armstrong, M., Mehrabi, H., & Naveed, N. (2022). An overview of modern metal additive manufacturing technology. In *Journal of Manufacturing Processes* (Vol. 84, pp. 1001–1029). Elsevier Ltd. https://doi.org/10.1016/j.jmapro.2022.10.060

Atapour, M., Wang, X., Persson, M., Odnevall Wallinder, I., & Hedberg, Y. S. (2020). Corrosion of Binder Jetting Additively Manufactured 316L Stainless Steel of Different Surface Finish. *Journal of The Electrochemical Society*, *167*(13), 131503. https://doi.org/10.1149/1945-7111/abb6cd

Baturynska, I., Semeniuta, O., & Wang, K. (2019). *Application of Machine Learning Methods to Improve Dimensional Accuracy in Additive Manufacturing* (pp. 245–252). https://doi.org/10.1007/978-981-13-2375-1_31

Bond, L. J. (2014). *Through the looking glass: The future for NDE?* 21–35. https://doi.org/10.1063/1.4864798

Bose, S., Ke, D., Sahasrabudhe, H., & Bandyopadhyay, A. (2018). Additive manufacturing of biomaterials. *Progress in Materials Science*, *93*, 45–111. https://doi.org/10.1016/j.pmatsci.2017.08.003

Carroll, B. E., Palmer, T. A., & Beese, A. M. (2015). Anisotropic tensile behavior of Ti–6Al–4V components fabricated with directed energy deposition additive manufacturing. *Acta Materialia*, *87*, 309–320. https://doi.org/10.1016/j.actamat.2014.12.054

Cherry, J. A., Davies, H. M., Mehmood, S., Lavery, N. P., Brown, S. G. R., & Sienz, J. (2015). Investigation into the effect of process parameters on microstructural and physical properties of 316L stainless steel parts by selective laser melting. *The International Journal of Advanced Manufacturing Technology*, *76*(5–8), 869–879. https://doi.org/10.1007/s00170-014-6297-2

Chia, H. Y., Wu, J., Wang, X., & Yan, W. (2022). Process parameter optimization of metal additive manufacturing: a review and outlook. *Journal of Materials Informatics*, *2*(3), 16. https://doi.org/10.20517/jmi.2022.18

Choze, S. B., Santos, R. R., & Gomes, G. F. (2022). Overview of Traditional and Recent Heuristic Optimization Methods. In *Model-based and Signal-Based Inverse Methods* (pp. 107–142). Biblioteca Central da Universidade de Brasilia. https://doi.org/10.4322/978-65-86503-71-5.c04

Dass, A., & Moridi, A. (2019). State of the Art in Directed Energy Deposition: From Additive Manufacturing to Materials Design. *Coatings*, *9*(7), 418. https://doi.org/10.3390/coatings9070418

DebRoy, T., Mukherjee, T., Milewski, J. O., Elmer, J. W., Ribic, B., Blecher, J. J., & Zhang, W. (2019). Scientific, technological and economic issues in metal printing and their solutions. *Nature Materials*, *18*(10), 1026–1032. https://doi.org/10.1038/s41563-019-0408-2

DebRoy, T., Wei, H. L., Zuback, J. S., Mukherjee, T., Elmer, J. W., Milewski, J. O., Beese, A. M., Wilson-Heid, A., De, A., & Zhang, W. (2018). Additive manufacturing of metallic components – Process, structure and properties. *Progress in Materials Science*, *92*, 112–224. https://doi.org/10.1016/j.pmatsci.2017.10.001

Di, W., Yongqiang, Y., Xubin, S., & Yonghua, C. (2012). Study on energy input and its influences on single-track,multi-track, and multi-layer in SLM. *The International Journal* *of Advanced Manufacturing Technology*, *58*(9–12), 1189–1199. https://doi.org/10.1007/s00170-011-3443-y

Ehlers, H., Pelkner, M., & Thewes, R. (2022). Online Process Monitoring for Additive Manufacturing Using Eddy Current Testing With Magnetoresistive Sensor Arrays. *IEEE Sensors Journal*, *22*(20), 19293–19300. https://doi.org/10.1109/JSEN.2022.3205177

Elmer, J. W., Vaja, J., Carpenter, J. S., Coughlin, D. R., Dvornak, M. J., Hochanadel, P., Gurung, P., Johnson, A., & Gibbs, G. (2019). *Wire-based Additive Manufacturing of Stainless Steel Components The Welding Journal*.

Era, I. Z., Farahani, M. A., Wuest, T., & Liu, Z. (2023). Machine learning in Directed Energy Deposition (DED) additive manufacturing: A state-of-the-art review. *Manufacturing Letters*, *35*, 689–700. https://doi.org/10.1016/j.mfglet.2023.08.079

Farrell, S. P., & Deering, J. (2018). Analysis of Seeded Defects in Laser Additive Manufactured 300M Steel. *Materials Performance and Characterization*, *7*(1), 300–315. https://doi.org/10.1520/MPC20170162

García Márquez, F. P., & Peinado Gonzalo, A. (2022). A Comprehensive Review of Artificial Intelligence and Wind Energy. *Archives of Computational Methods in Engineering*, *29*(5), 2935–2958. https://doi.org/10.1007/s11831-021-09678-4

Gebhardt, A., & Hötter, J.-S. (2016). *Additive Manufacturing*. Carl Hanser Verlag GmbH & Co. KG. https://doi.org/10.1007/978-1-56990-583-8

Gobert, C., Reutzel, E. W., Petrich, J., Nassar, A. R., & Phoha, S. (2018). Application of supervised machine learning for defect detection during metallic powder bed fusion additive manufacturing using high resolution imaging. *Additive Manufacturing*, *21*, 517–528. https://doi.org/10.1016/j.addma.2018.04.005

Gonzalez-Gutierrez, J., Cano, S., Schuschnigg, S., Kukla, C., Sapkota, J., & Holzer, C. (2018). Additive Manufacturing of Metallic and Ceramic Components by the Material Extrusion of Highly-Filled Polymers: A Review and Future Perspectives. *Materials*, *11*(5), 840. https://doi.org/10.3390/ma11050840

Grasso, M., Laguzza, V., Semeraro, Q., & Colosimo, B. M. (2017). In-Process Monitoring of Selective Laser Melting: Spatial Detection of Defects Via Image Data Analysis. *Journal of Manufacturing Science and Engineering*, *139*(5). https://doi.org/10.1115/1.4034715

Gu, D., & Shen, Y. (2009). Balling phenomena in direct laser sintering of stainless steel powder: Metallurgical mechanisms and control methods. *Materials & Design*, *30*(8), 2903–2910. https://doi.org/10.1016/j.matdes.2009.01.013

Gupta, P., Krishna, C., Rajesh, R., Ananthakrishnan, A., Vishnuvardhan, A., Patel, S. S., Kapruan, C., Brahmbhatt, S., Kataray, T., Narayanan, D., Chadha, U., Alam, A., Selvaraj, S. K., Karthikeyan, B., Nagalakshmi, R., & Chandramohan, V. (2022). Industrial internet of things in intelligent manufacturing: a review, approaches, opportunities, open challenges, and future directions. *International Journal on Interactive Design and Manufacturing (IJIDeM)*. https://doi.org/10.1007/s12008-022-01075-w

Hossain, M. S., & Taheri, H. (2021). In-situ process monitoring for metal additive manufacturing through acoustic techniques using wavelet and convolutional neural network (CNN). *The International Journal of Advanced Manufacturing Technology*, *116*(11–12), 3473–3488. https://doi.org/10.1007/s00170-021-07721-z

ISO/TC 261, & ASTM- Komitee F42. (2021). ISO/ASTM 52900:2021. In *Additive manufacturing — General principles — Fundamentals and vocabulary* (Vol. 2).

Ituarte, I. F., Nilsén, F., Nadimpalli, V. K., Salmi, M., Lehtonen, J., & Hannula, S.-P. (2022). Towards the additive manufacturing of Ni-Mn-Ga complex devices with magnetic field induced strain. *Additive Manufacturing*, *49*, 102485. https://doi.org/10.1016/j.addma.2021.102485

Jiang, Y., Wang, H., Chen, S., Zhang, Q., Hu, P., Li, X., Zheng, K., & Wang, H. (2020). Quantitative Imaging Detection of Additive Manufactured Parts Using Laser Ultrasonic Testing. *IEEE Access*, *8*, 186071–186079. https://doi.org/10.1109/ACCESS.2020.3030307

Johnson, N. S., Vulimiri, P. S., To, A. C., Zhang, X., Brice, C. A., Kappes, B. B., & Stebner, A. P. (2020). Invited review: Machine learning for materials developments in metals additive manufacturing. *Additive Manufacturing*, *36*, 101641. https://doi.org/10.1016/j.addma.2020.101641

Kamath, C., El-dasher, B., Gallegos, G. F., King, W. E., & Sisto, A. (2014). Density of additively-manufactured, 316L SS parts using laser powder-bed fusion at powers up to 400 W. *The International Journal of Advanced Manufacturing Technology*, *74*(1–4), 65–78. https://doi.org/10.1007/s00170-014-5954-9

Khanzadeh, M., Chowdhury, S., Tschopp, M. A., Doude, H. R., Marufuzzaman, M., & Bian, L. (2019). *In-situ* monitoring of melt pool images for porosity prediction in directed energy deposition processes. *IISE Transactions*, *51*(5), 437–455. https://doi.org/10.1080/24725854.2017.1417656

Kim, F. H., Moylan, S. P., Garboczi, E. J., & Slotwinski, J. A. (2017). Investigation of pore structure in cobalt chrome additively manufactured parts using X-ray computed tomography and three-dimensional image analysis. *Additive Manufacturing*, *17*, 23–38. https://doi.org/10.1016/j.addma.2017.06.011

Kok, Y., Tan, X. P., Wang, P., Nai, M. L. S., Loh, N. H., Liu, E., & Tor, S. B. (2018). Anisotropy and heterogeneity of microstructure and mechanical properties in metal additive manufacturing: A critical review. *Materials & Design*, *139*, 565–586. https://doi.org/10.1016/j.matdes.2017.11.021

Kruth, J.-P., Badrossamay, M., Yasa, E., Deckers, J., Thijs, L., & Van Humbeeck, J. (2010a). Part and material properties in selective laser melting of metals. *16th International Symposium on Electromachining, ISEM 2010*, 3–14.

Kruth, J.-P., Badrossamay, M., Yasa, E., Deckers, J., Thijs, L., & Van Humbeeck, J. (2010b). Part and material properties in selective laser melting of metals. *16th International Symposium on Electromachining, ISEM 2010*, 3–14.

Larimian, T., Kannan, M., Grzesiak, D., AlMangour, B., & Borkar, T. (2020). Effect of energy density and scanning strategy on densification, microstructure and mechanical properties of 316L stainless steel processed via selective laser melting. *Materials Science and Engineering: A*, *770*, 138455. https://doi.org/10.1016/j.msea.2019.138455

Leuders, S., Thöne, M., Riemer, A., Niendorf, T., Tröster, T., Richard, H. A., & Maier, H. J. (2013). On the mechanical behaviour of titanium alloy TiAl6V4 manufactured by selective laser melting: Fatigue resistance and crack growth performance. *International Journal of Fatigue*, *48*, 300–307. https://doi.org/10.1016/j.ijfatigue.2012.11.011

Li, R., Shi, Y., Liu, J., Yao, H., & Zhang, W. (2009). Effects of processing parameters on the temperature field of selective laser melting metal powder. *Powder Metallurgy and Metal Ceramics*, *48*(3–4), 186–195. https://doi.org/10.1007/s11106-009-9113-z

Liu, J., Ye, J., Silva Izquierdo, D., Vinel, A., Shamsaei, N., & Shao, S. (2023). A review of machine learning techniques for process and performance optimization in laser beam powder bed fusion additive manufacturing. *Journal of Intelligent Manufacturing*, *34*(8), 3249–3275. https://doi.org/10.1007/s10845-022-02012-0

Liu, Y., Zhang, M., Shi, W., Ma, Y., & Yang, J. (2021). Study on performance optimization of 316L stainless steel parts by High-Efficiency Selective Laser Melting. *Optics & Laser Technology*, *138*, 106872. https://doi.org/10.1016/j.optlastec.2020.106872

Liu, Z., Jiang, Q., Li, T., Dong, S., Yan, S., Zhang, H., & Xu, B. (2016). Environmental benefits of remanufacturing: A case study of cylinder heads remanufactured through laser cladding. *Journal of Cleaner Production*, *133*, 1027–1033. https://doi.org/10.1016/j.jclepro.2016.06.049

Liverani, E., Toschi, S., Ceschini, L., & Fortunato, A. (2017). Effect of selective laser melting (SLM) process parameters on microstructure and mechanical properties of 316L austenitic stainless steel. *Journal of Materials Processing Technology*, *249*, 255–263. https://doi.org/10.1016/j.jmatprotec.2017.05.042

Lores, A., Azurmendi, N., Agote, I., & Zuza, E. (2019). A review on recent developments in binder jetting metal additive manufacturing: materials and process characteristics. *Powder Metallurgy*, *62*(5), 267–296. https://doi.org/10.1080/00325899.2019.1669299

Meng, L., McWilliams, B., Jarosinski, W., Park, H.-Y., Jung, Y.-G., Lee, J., & Zhang, J. (2020). Machine Learning in Additive Manufacturing: A Review. *JOM*, *72*(6), 2363–2377. https://doi.org/10.1007/s11837-020-04155-y

Milewski, J. O. (n.d.). *Springer Series in Materials Science 258 Additive Manufacturing of Metals From Fundamental Technology to Rocket Nozzles, Medical Implants, and Custom Jewelry*. http://www.springer.com/series/856

Miranda, G., Faria, S., Bartolomeu, F., Pinto, E., Madeira, S., Mateus, A., Carreira, P., Alves, N., Silva, F. S., & Carvalho, O. (2016). Predictive models for physical and mechanical properties of 316L stainless steel produced by selective laser melting. *Materials Science and Engineering: A*, *657*, 43–56. https://doi.org/10.1016/j.msea.2016.01.028

Mireles, J., Ridwan, S., Morton, P. A., Hinojos, A., & Wicker, R. B. (2015). Analysis and correction of defects within parts fabricated using powder bed fusion technology. *Surface Topography: Metrology and Properties*, *3*(3), 034002. https://doi.org/10.1088/2051-672X/3/3/034002

Mirzababaei, S., & Pasebani, S. (2019). A review on binder jet additive manufacturing of 316L stainless steel. In *Journal of Manufacturing and Materials Processing* (Vol. 3, Issue 3). MDPI Multidisciplinary Digital Publishing Institute. https://doi.org/10.3390/jmmp3030082

Miyanaji, H., Zhang, S., & Yang, L. (2017). *A new physics-based model for equilibrium saturation determination in binder jetting additive manufacturing process*. https://doi.org/10.1016/j.ijmachtools.2017.09.001

Mohr, G., Altenburg, S. J., Ulbricht, A., Heinrich, P., Baum, D., Maierhofer, C., & Hilgenberg, K. (2020). In-Situ Defect Detection in Laser Powder Bed Fusion by Using Thermography and Optical Tomography—Comparison to Computed Tomography. *Metals*, *10*(1), 103. https://doi.org/10.3390/met10010103

Obaton, A.-F., Butsch, B., McDonough, S., Carcreff, E., Laroche, N., Gaillard, Y., Tarr, J. B., Bouvet, P., Cruz, R., & Donmez, A. (2020). Evaluation of Nondestructive Volumetric Testing Methods for Additively Manufactured Parts. In *Structural Integrity of Additive Manufactured Parts* (pp. 51–91). ASTM International100 Barr Harbor Drive, PO Box C700, West Conshohocken, PA 19428-2959. https://doi.org/10.1520/STP162020180099

Pandiyan, V., Drissi-Daoudi, R., Shevchik, S., Masinelli, G., Le-Quang, T., Logé, R., & Wasmer, K. (2021). Semi-supervised Monitoring of Laser powder bed fusion process based on acoustic emissions. *Virtual and Physical Prototyping*, *16*(4), 481–497. https://doi.org/10.1080/17452759.2021.1966166

Pereira, R. J. R., de Almeida, F. A., & Gomes, G. F. (2023). A multiobjective optimization parameters applied to additive manufacturing: DOE-based approach to 3D printing. *Structures*, *55*, 1710–1731. https://doi.org/10.1016/j.istruc.2023.06.136

Qi, X., Chen, G., Li, Y., Cheng, X., & Li, C. (2019). Applying Neural-Network-Based Machine Learning to Additive Manufacturing: Current Applications, Challenges, and Future Perspectives. *Engineering*, *5*(4), 721–729. https://doi.org/10.1016/j.eng.2019.04.012

Qiu, C., Panwisawas, C., Ward, M., Basoalto, H. C., Brooks, J. W., & Attallah, M. M. (2015). On the role of melt flow into the surface structure and porosity development during selective laser melting. *Acta Materialia*, *96*, 72–79. https://doi.org/10.1016/j.actamat.2015.06.004

Rahmati, S. (2014). Direct Rapid Tooling. In *Comprehensive Materials Processing* (pp. 303–344). Elsevier. https://doi.org/10.1016/B978-0-08-096532-1.01013-X

Salman, O. O., Brenne, F., Niendorf, T., Eckert, J., Prashanth, K. G., He, T., & Scudino, S. (2019). Impact of the scanning strategy on the mechanical behavior of 316L steel synthesized by selective laser melting. *Journal of Manufacturing Processes*, *45*, 255–261. https://doi.org/10.1016/j.jmapro.2019.07.010

Sarker, I. H. (2022). AI-Based Modeling: Techniques, Applications and Research Issues Towards Automation, Intelligent and Smart Systems. *SN Computer Science*, *3*(2), 158. https://doi.org/10.1007/s42979-022-01043-x

Segovia Ramírez, I., García Márquez, F. P., & Papaelias, M. (2023a). Review on additive manufacturing and non-destructive testing. *Journal of Manufacturing Systems*, *66*, 260–286. https://doi.org/10.1016/j.jmsy.2022.12.005

Segovia Ramírez, I., García Márquez, F. P., & Papaelias, M. (2023b). Review on additive manufacturing and non-destructive testing. *Journal of Manufacturing Systems*, *66*, 260–286. https://doi.org/10.1016/j.jmsy.2022.12.005

Shevchik, S. A., Kenel, C., Leinenbach, C., & Wasmer, K. (2018). Acoustic emission for in situ quality monitoring in additive manufacturing using spectral convolutional neural networks. *Additive Manufacturing*, *21*, 598–604. https://doi.org/10.1016/j.addma.2017.11.012

Shi, W., Ren, Z., He, W., Hou, J., Xie, H., & Liu, S. (2021). A technique combining laser spot thermography and neural network for surface crack detection in laser engineered net shaping. *Optics and Lasers in Engineering*, *138*, 106431. https://doi.org/10.1016/j.optlaseng.2020.106431

Shi, W., Wang, P., Liu, Y., Hou, Y., & Han, G. (2020). Properties of 316L formed by a 400 W power laser Selective Laser Melting with 250 μm layer thickness. *Powder Technology*, *360*, 151–164. https://doi.org/10.1016/j.powtec.2019.09.059

Shinde, M. S., & Ashtankar, K. M. (2017). Additive manufacturing–assisted conformal cooling channels in mold manufacturing processes. *Advances in Mechanical Engineering*, *9*(5), 168781401769976. https://doi.org/10.1177/1687814017699764

Song, Y.-U., Song, B. U., Jung, M.-K., Lee, C., Choi, J. P., & Lee, I. (2024). Multi-fidelity Gaussian process modeling of a thin-walled structure for laser powder bed fusion (LPBF) process window. *Journal of Manufacturing Processes*, *127*, 107–114. https://doi.org/10.1016/j.jmapro.2024.07.085

Sun, Z., Tan, X., Tor, S. B., & Yeong, W. Y. (2016). Selective laser melting of stainless steel 316L with low porosity and high build rates. *Materials & Design*, *104*, 197–204. https://doi.org/10.1016/j.matdes.2016.05.035

Sutton, R. S., & Barto, A. G. (n.d.). *Reinforcement Learning: An Introduction Second edition, in progress*.

Tapia, G., & Elwany, A. (2014). A Review on Process Monitoring and Control in Metal-Based Additive Manufacturing. *Journal of Manufacturing Science and Engineering*, *136*(6). https://doi.org/10.1115/1.4028540

Thompson, S. M., Bian, L., Shamsaei, N., & Yadollahi, A. (2015). An overview of Direct Laser Deposition for additive manufacturing; Part I: Transport phenomena, modeling and diagnostics. *Additive Manufacturing*, *8*, 36–62. https://doi.org/10.1016/j.addma.2015.07.001

Tucho, W. M., Lysne, V. H., Austbø, H., Sjolyst-Kverneland, A., & Hansen, V. (2018). Investigation of effects of process parameters on microstructure and hardness of SLM manufactured SS316L. *Journal of Alloys and Compounds*, *740*, 910–925. https://doi.org/10.1016/j.jallcom.2018.01.098

Unger, L., Scheideler, M., Meyer, P., Harland, J., Gorzen, A., Wortmann, M., Dreyer, A., & Ehrmann, A. (2018). Increasing adhesion of 3D printing on textile fabrics by polymer coating. *TEKSTILEC*, *61*(4), 265–271. https://doi.org/10.14502/Tekstilec2018.61.265-271

Wang, C., Tan, X. P., Tor, S. B., & Lim, C. S. (2020). Machine learning in additive manufacturing: State-of-the-art and perspectives. *Additive Manufacturing*, *36*, 101538. https://doi.org/10.1016/j.addma.2020.101538

Wang, Q., Zhang, S., Zhang, C., Wu, C., Wang, J., Chen, J., & Sun, Z. (2017). Microstructure evolution and EBSD analysis of a graded steel fabricated by laser additive manufacturing. *Vacuum*, *141*, 68–81. https://doi.org/10.1016/j.vacuum.2017.03.021

Wei, Q. S., Zhao, X., Wang, L., Li, R. Di, Liu, J., & Shi, Y. S. (2011). Effects of the Processing Parameters on the Forming Quality of Stainless Steel Parts by Selective Laser Melting.

Advanced Materials Research, *189–193*, 3668–3671. https://doi.org/10.4028/www.scientific.net/AMR.189-193.3668

West, B. M., Capps, N. E., Urban, J. S., Pribe, J. D., Hartwig, T. J., Lunn, T. D., Brown, B., Bristow, D. A., Landers, R. G., & Kinzel, E. C. (2017). Modal analysis of metal additive manufactured parts. *Manufacturing Letters*, *13*, 30–33. https://doi.org/10.1016/j.mfglet.2017.06.001

Wu, H., Yu, Z., & Wang, Y. (2016, June 27). A New Approach for Online Monitoring of Additive Manufacturing Based on Acoustic Emission. *Volume 3: Joint MSEC-NAMRC Symposia*. https://doi.org/10.1115/MSEC2016-8551

Xue, R., Cui, X., Zhang, P., Liu, K., Li, Y., Wu, W., & Liao, H. (2020). Mechanical design and energy absorption performances of novel dual scale hybrid plate-lattice mechanical metamaterials. *Extreme Mechanics Letters*, *40*, 100918. https://doi.org/10.1016/j.eml.2020.100918

Yakout, M., Elbestawi, M. A., & Veldhuis, S. C. (2019). Density and mechanical properties in selective laser melting of Invar 36 and stainless steel 316L. *Journal of Materials Processing Technology*, *266*, 397–420. https://doi.org/10.1016/j.jmatprotec.2018.11.006

Ye, D., Hsi Fuh, J. Y., Zhang, Y., Hong, G. S., & Zhu, K. (2018). In situ monitoring of selective laser melting using plume and spatter signatures by deep belief networks. *ISA Transactions*, *81*, 96–104. https://doi.org/10.1016/j.isatra.2018.07.021

Yu, J., Zhang, D., Li, H., Song, C., Zhou, X., Shen, S., Zhang, G., Yang, Y., & Wang, H. (2020). Detection of Internal Holes in Additive Manufactured Ti-6Al-4V Part Using Laser Ultrasonic Testing. *Applied Sciences*, *10*(1), 365. https://doi.org/10.3390/app10010365

Yuan, B., Guss, G. M., Wilson, A. C., Hau-Riege, S. P., DePond, P. J., McMains, S., Matthews, M. J., & Giera, B. (2018). Machine-Learning-Based Monitoring of Laser Powder Bed Fusion. *Advanced Materials Technologies*, *3*(12). https://doi.org/10.1002/admt.201800136

Yusuf, S., Chen, Y., Boardman, R., Yang, S., & Gao, N. (2017). Investigation on Porosity and Microhardness of 316L Stainless Steel Fabricated by Selective Laser Melting. *Metals*, *7*(2), 64. https://doi.org/10.3390/met7020064

Zhang, Y., Hong, G. S., Ye, D., Zhu, K., & Fuh, J. Y. H. (2018). Extraction and evaluation of melt pool, plume and spatter information for powder-bed fusion AM process monitoring. *Materials & Design*, *156*, 458–469. https://doi.org/10.1016/j.matdes.2018.07.002

Zhong, T., He, K., Li, H., & Yang, L. (2019). Mechanical properties of lightweight 316L stainless steel lattice structures fabricated by selective laser melting. *Materials & Design*, *181*, 108076. https://doi.org/10.1016/j.matdes.2019.108076

Ziaee, M., & Crane, N. B. (2019). *Binder jetting: A review of process, materials, and methods*. https://doi.org/10.1016/j.addma.2019.05.031